AN IN VITRO 3D PLATFORM FOR IDENTIFYING FACTORS REGULATING DPSC POLARIZATION AND DIFFERENTIATION

A Dissertation

by

BEI CHANG

Submitted to the Office of Graduate and Professional Studies of
Texas A&M University
in partial fulfillment of the requirements for the degree of

DOCTOR OF PHILOSOPHY

Chair of Committee,	Xiaohua Liu
Committee Members,	Kathy Svoboda
	Jian Q. Feng
	Yongbo Lu
	Hu Zhao
Head of Department,	Larry Bellinger

August 2020

Major Subject: Oral Biology

ABSTRACT

Regeneration of functional dentin remains challenging in regenerative dentistry since it requires a precise control of odontoblast polarization and differentiation. Both biophysical and biochemical factors have been proposed to play critical roles in regulating odontoblast behaviors, while currently there is no feasible platform to examine their effects. Therefore, an *in vitro* platform which enables the isolation of single biophysical/biochemical factor seems necessary. A gelatin-derived nanofibrous matrix-based micropattern system was developed by combining electrospinning, photolithography and laser ablation techniques. This system provides a clean and biomimetic background that allows for single odontoblast entrapment and observation.

Micropatterns with various biophysical properties were fabricated to examine their influence on isolated human dental pulp stem cells (hDPSCs). Nanofibrous topography promoted a more *in vivo*-like cell morphology and stronger odontogenic differentiation of single hDPSCs when compared to a smooth topography. A large micropattern size also increased hDPSC differentiation. However, hDPSC polarization wasn't observed on any of these 2D micropatterns. Therefore, a 3D tubular architecture was generated and hDPSCs were successfully induced to polarize *in vitro* with a odontoblast-like cell morphology and increased differentiation ability. Afterwards, rotated microenvironments were created and it's found that gravity was a contributory factor in inducing hDPSC polarization.

In addition, influences of various biochemical factors were explored on the novel platform. Results showed intercellular communication efficiently promoted hDPSC differentiation but failed to enhance hDPSC polarization. Eight types of growth factors, including TGF-β, BMP-2, BMP-4, EGF, HGF, FGF2, Wnt5a and Shh, promoted hDPSC polarization within appropriate concentration ranges, while higher concentrations damaged the cell limitation effect of micropatterns. Besides, rat BMSCs seeded to the NF-MT scaffolds displayed similar polarization behaviors but distinct differentiation capacity with hDPSCs. Moreover, the addition of several inhibitors confirmed that the cytoskeletal integrity and integrin-mediated cell adhesion were prerequisites for hDPSC polarization and differentiation.

In summary, we generated an novel platform for single hDPSC study and successfully induced hDPSC polarization *in vitro*. This platform allowed us to explore the effects of various biophysical and biochemical factors on hDPSC polarization and differentiation, which may benefit the development of next-generation dentin regenerative strategies.

ACKNOWLEDGEMENTS

Successful completion of the research that comprises this dissertation is not a singular effort but involves the dedicated support of many individuals. For this reason, I wish to acknowledge my dissertation advisor, Dr. Xiaohua Liu, for his continual, patient mentoring. He provided such a friendly and exciting research environment filled with possibilities, which allowed me to work comfortably. He discussed with me frequently, encourages me to think independently and creatively but never pushes me to do anything. He is always supportive that he never criticized my work and instead, he tried all his best to help me and gave me a lot of encouragement when I was frustrated by my research work. His caring and kind personal character comforted me greatly and supported me to overcome many difficulties. He is the best mentor I've known and I can never say enough thank you to him.

I am also indebted to the considerable help and expertise of Dr. Kathy Svoboda, who supervised my progress and ensured that everything was on time. Dr. Svoboda helped me a lot in analyzing my data during the committee meetings. She paid attention to small details and came up with very helpful suggestions. She also helped a lot in reviewing my cognate review paper. She read the manuscript carefully and offered many inspiring and detailed suggestions every time I gave her the updated version, which greatly promoted the publication of the review paper. Also, she offered tremendous help and support to me when I was trying hard in figuring my future career. She was

insightful and always selflessly helpful to all the students, and I wish I could live like her in my future career.

Dr. Jerry Feng has always been a great committee advisor, who not only generously offered me convenience in using the equipment and facilities in his lab, but also offered me a lot of creative ideas and thoughts to review my research and my data. Also, it's always nice to talk to and learn from Dr. Feng during lunchtime since he is always so humorous and perceptive. I received so much help from him and I really appreciate his generous help.

I am lucky to have Dr. Yongbo Lu in my committee. He gave me a lot of insightful ideas about the construction of my research project and that provided me a lot of thoughts. He also assisted me greatly in finishing my cognate work and raised very perspectives questions. He was very careful in proposing a project and interpreting the data, which taught me a lot. Apart from that, he is such a nice person that I would always like to talk to him and discuss my concerns.

I also appreciate Dr. Zhao Hu for his insightful views of my research work and his support. It's always inspiring to see him working enthusiastically in lab and that encouraged me a lot. I deeply admire his creative thoughts and endless enthusiasm in research work.

I also need to express my gratitude to all the members in our department. Dr. Opperman, our department head, is taking good care of all the graduate students, including me. I also learn a lot from her during the Colloquium, like how she discovers a question and interprets the data. Dr. Bellinger, the professor monitoring research in the

whole college, provides me many opportunities to talk about my research in the school. The department is a very lovely place to stay, which is made possible by Kim, Marge, Nancy, Meghan, Sophie, Richard, Jeanne and Darla. Their kindness and help make my life much easier than I thought it would be. For sure, I would not forget the help from members of our lab. Dr. Chi Ma played an indispensable role in developing the scaffold and offered numerous great advice on my research which has contributed to the big progress we made toward the final conclusions. I sincerely believe he is a nature researcher and I've learnt a lot from him. Dr. Xiangwei Li and Dr. Xiaogang Cheng helped me a lot in adapting to the environment when I first arrived here. Dr. Zhiai Hu and Dr. Rurxin Wu offered me a lot of helpful advice in some technical problems. Yongxi Liang and Qian Li are both very nice person, they have great personalities and inspired me a lot when I was upset. I want to give special thanks to Dr. Ke Wang and Dr. Wenjing Luo. We became best friends since we met 5 years ago. During these years, they laughed with me, cried with me and taught me to hug both good and bad from life. Even after they left Dallas, they continued to care about me and provided enormous courage and happiness to me. It's my greatest honor to have such friends in a foreign country. Also, I would like to thank all the people I've sought for help during the five years, Yan Jing, Mary, Priscilla, Gerald and all the graduate students. They made my life much colorful and easier and I am really lucky to have such a group of people in my life.

CONTRIBUTORS AND FUNDING SOURCES

Contributors

This work was supervised by a thesis (or) dissertation committee consisting of Professor Dr. Xiaohua Liu, Dr. Kathy Svoboda, Dr. Jerry Feng, and Dr. Yongbo Lu of the Department of Biomedical Sciences and Professor Dr. Hu Zhao of the Department of Restorative Sciences.

The measurement of BMP-2 staining intensity and the mechanical properties of the scaffolds in Chapter 2 was performed by Professor Dr. Chi Ma of the Department of Biomedical Sciences. All other work conducted for the dissertation was completed by the student independently.

Funding Sources

Graduate study was supported by the department of Biomedical Sciences and Grants DE 024979 from the National Institutes of Dental and Craniofacial Research and a scholarship from China Scholarship Council (201506170032).

NOMENCLATURE

HDPSC	Human dental pulp stem cell
2D	Two-dimensional
3D	Three-dimensional
TGF-β	Transforming growth factor beta
BMP	Bone morphogenetic protein
EGF	Epidermal growth factor
HGF	Hepatocyte growth factor
FGF2	Fibroblast growth factor 2
Wnt5a	Wingless-related integration site-5a
Shh	Sonic Hedgehog
BMSC	Bone marrow stem cell
MTA	Mineral trioxide aggregate
BSP	Bone sialoprotein
DSP	Dentin sialoprotein
Gla	Gamma-carboxyglutamic
ER	Endoplasmic reticulum
ECM	Extracellular matrix
MTOC	Microtubule organizing center
AJ	Adherens junction
PAR	Protease-activated receptor

G-actin	Globular actin
F-actin	Filamentous actin
Arp2/3	Actin-related protein2/3
ADF	Actin depolymerization factor
CPNE7	Copine 7
MAP	Microtubule-associated protein
+TIPS	Microtubule plus-end tracking proteins
ACF7	Actin cross-linking factor 7
EB1	MAPRE1, Microtubule-associated protein RP/EB family member
Tea	Tip elongation aberrant protein
RhoA	Ras homolog gene family, member A
GEF	Guanine nucleotide exchange factor
CLASP	Cytoplasmic linker associated protein
IQGAP1	IQ motif containing GTPase activating protein 1
APC	Adenomatous polyposis coli
LINC	Linker of nucleoskeleton and cytoskeleton
SUN	Sad1p, UNC-84
TBCCD1	TBCC domain-containing protein 1
AKAP	A kinase (PRKA) anchor protein
TJ	Tight junctions
MARVELD	MARVEL domain containing-protein
ZO	Zonula occludens

JACOP	Junction-associated-coiled-coil protein
ROCK	Rho-associated, coiled-coil containing protein kinase 1
ZONAB	Zonula occludens 1-associated nucleic acid binding protein
E-cadherin	Epithelial cadherins
N-cadherin	Neural cadherin
Nfic	Nuclear factor 1 C-type
AJ	Adherens junctions
ZO	Zonula occludens
JACOP	Junction-associated-coiled-coil protein
aPKC	Atypical protein kinase C
CRB	Crumbs homolog
PALS1	Protein associated with Lin seven 1
PATJ	PALS1-associated tight junction protein
SCRIB	Scribble
LGL	Lethal giant larvae
DLG	Discs large
JAM-1	Junctional adhesion molecule 1
JAMA	Junctional adhesion molecule A
Rac1	Ras-related C3 botulinum toxin substrate 1
Cdc42	Cell division control protein 42 homolog
LIMK	LIM domain kinase
WASP	Wiskott–Aldrich syndrome protein

WAVE	Wasp-family verprolin-homologous protein
mDia1	Diaphanous homolog 1
FAK	Focal adhesion kinase
GEF-H1	Guanine nucleotide exchange factor H1
GAP	GTPase-activating proteins
DLC3	Deleted in liver cancer 3
Tiam1	T-cell lymphoma invasion and metastasis-inducing protein 1
Tuba	DNMBP, dynamin binding protein
NWASP	Neural Wiskott-Aldrich syndrome protein
ARHGEF11	Rho guanine nucleotide exchange factor 11
LKB1	Liver kinase B1
NGF	Nerve growth factor
IGF	Insulin-like growth factor
Runx2	Runt-related transcription factor 2
TWIST1	Twist Family BHLH Transcription Factor 1
DSPP	Dentin sialophosphoprotein
DMP1	Dentin matrix acidic phosphoprotein 1
SMAD4	Mothers against decapentaplegic homolog 4
Dlx3	Distal-less homeobox 3
PDMS	Polydimethylsiloxane
GelMA	Methacrylamide-functionalized gelatin
PBS	Phosphate-buffered saline

FITC	Fluorescein isothiocyanate
MES	4-Morpholinoethanesulfonic acid
EDC	N-(3-Dimethylaminopropyl)-N′-ethylcarbodiimide hydrochloride
NHS	N-hydroxysuccinimide
PEGDA	Polyethylene (glycol) diacrylate
UV	Ultraviolet
NF-MP	Nanofibrous micropattern
PEN	Polyethylene naphthalate
NF-MT	Nanofibrous micropattern with tubules
FBS	Fetal bovine serum
DIC	Differential interference contrast
PFA	Paraformaldehyde
DAPI	4′,6-diamidino-2-phenylindole
ALP	Alkaline phosphatase
SEM	Scanning electron microscopy
SD	Standard deviation
ANOVA	Analysis of variance
MTT	3-(4,5-Dimethylthiazol-2-yl)-2,5-diphenyltetrazolium bromide
EDS	Energy dispersive X-ray spectroscopy
RGD	Arginine-glycine-aspartic acid
MMP	Matrix metalloproteinase
MSC	Mesenchymal stem cells

CNS	Central nervous system
PLGA	Poly(lactic-co-glycolic acid)
YAP1	Yes-associated protein 1
GRASP65	Golgi reassembly-stacking protein of 65 kDa
AR	Aspect ratio
CI	Circularity index
MAPK	Mitogen-activated protein kinase
CTGF	Connective tissue growth factor
DNA	Deoxyribonucleic acid
Myod1	Myogenic differentiation 1
RT-PCR	Real-time polymerase chain reaction
AGA	18α-Glycyrrhetinic acid
NF-M2T	Nanofibrous micropatterns with 2 tubules
ERK	Extracellular signal-regulated kinases
mRNA	Messenger ribonucleic acid
SHED	Stem cells from human exfoliated deciduous teeth
SCAP	Stem cells of apical papilla
Gli1	GLI family zinc finger 1
Ptch1	Protein patched homolog 1
Smo	Smoothened

TABLE OF CONTENTS

Page

LIST OF FIGURES

Page

LIST OF TABLES

Page

1. INTRODUCTION

Dentin is formed by odontoblasts. Normal dentin possesses a tubular structure with odontoblast processes, neural fibers and dentinal fluid within the dentin tubules. This tubular structure, together with its contents is necessary for normal dentin functions. Dentin loss caused by caries or traumas can't be self-repaired and requires a clinical restoration process. When dental pulp remain active, bioactive reagents like calcium hydroxide or MTA are commonly used on accidently exposed pulp or for apical angioplasty to promote the differentiation of pulpal stem cells into odontoblasts to produce dentin and repair the defect. However, even though these reagents have been widely used in clinic with satisfying clinical outcome, detailed observations have found that functional dentin could hardly be regenerated. Unlike the tubular structure of nature dentin, the neo-regenerated mineralized tissues using above-mentioned reagents are usually more similar to bone morphologically as it typically exhibits a disorganized, non-tubular structure with the matrix-secreting cells embedded within the tissues, while the characteristic polarized odontoblasts or odontoblast processes can hardly be found. As a result, the normal functions of dentin including neural transduction and sensation to exterior stimuli are missing, and moreover, the mechanical strength of the neo-regenerated tissue is not matched to the surrounding nature dentin, which may result in secondary caries or dentin fracture.

The formation of tubular dentin depends on the precise control of odontoblast polarization and differentiation. Therefore, in order to achieve functional tubular dentin

regeneration, a comprehensive understanding of the odontoblast polarization and differentiation processes seems essential. However, currently there is only very limited knowledge about odontoblast polarization and differentiation in primary odontogenesis, and moreover, critical factors that regulate these processes haven't been identified. This knowledge gap greatly impedes the development of functional dentin regeneration strategies, thus, it's important to address this knowledge gap in odontoblast study and identify possible regulating factors for odontoblast polarization and differentiation, which may provide clues for future odontoblast or dentin regenerative studies.

In this dissertation, four parts will be included. First, the known knowledge and possible molecular mechanisms related to odontoblast polarization will be reviewed. Second, a biomimetic scaffold will be established to enable single hDPSC entrapment and observation *in vitro*. Third, biophysical factors that regulate hDPSC polarization and differentiation behaviors will be identified. Fourth, biochemical factors that regulate hDPSC polarization and differentiation behaviors will be identified.

1.1. Odontoblast morphological change

Odontoblasts are a layer of dentin-forming cells at the periphery of dental pulp. In the early stage of primary dentinogenesis, the outermost layer of dental mesenchymal cells in dental papilla receive signals from adjacent differentiating pre-ameloblasts and start their differentiation into odontoblasts. During this transition process, both the morphological change (odontoblast polarization) and function maturation (odontoblast differentiation) are evident. Morphologically, the relatively isotropic mesenchymal cells transform into a layer of highly organized columnar odontoblasts with evident cell

polarity. Maturation in cellular function accompanies the morphological transformation that mature odontoblasts secret predentin components including collagen type I, type I trimer, types V, together with proteoglycans like decorin, bi-glycan, non-collagenous proteins like bone sialoprotein (BSP), dentin sialoprotein (DSP), and Gla proteins like osteocalcin [1]. These matrix components deposit around the odontoblast process and start mineralization with the addition of calcium ions and phosphate reagents, thus tubular dentin forms. The polarized morphology and the characteristic cytosol distribution pattern of odontoblasts play determinative roles in the direction of cell secretion and subsequently the formation of tubular dentin. Therefore, to overcome the challenge in regenerating tubular dentin, an extensive exploration of odontoblast polarization seems foremost important.

In contrary to the relatively isotropic dental mesenchymal cells, the asymmetric morphology of odontoblasts evidently announce that they are a group of polarized cells. Their morphological features mainly include the unidirectional formation of odontoblast process and characteristic distribution patterns of organelles and cytoskeleton elements.

Odontoblasts are highly columnar cells that align tightly in a layer. Within each odontoblast, a long cytoplasmic process extends from the cell body and stretches towards to the dentin-enamel junction, while on the another side which faces the dental pulp, no such process is formed. As the odontoblast process moves towards the eccentric dentin, multiple mini-branches extend from the odontoblast process trunk [2] and those mini-branches interlace between neighboring odontoblast processes to provide a means for intercellular communication.

The positions of organelles change with the maturation of odontoblasts [1]. During the transition from mesenchymal cells to odontoblasts, cell nucleus moves towards the pulp side, the Golgi apparatus moves to the supranuclear region, and the centrosome locates between the nucleus and the Golgi apparatus [102]. Endoplasmic reticulum (ER) is distributed at two regions within the cytosol. A well-developed and flattened ER is found laterally and parallel to the long axis of the cell, and a secretory vesicle-rich RER-filled area where the RER is abruptly interrupted is simultaneously found proximal to the odontoblast process [1]. Vesicles related to exocytosis and endocytosis [3] and organelles have also been found in odontoblast processes. Fragments of isolated ER and ribosome-like granules are found in the process in predentin but are seldomly seen in eccentric dentin, while mitochondria have been observed throughout the process even near the dentin-enamel junction [4]. This distribution pattern of organelles within odontoblast process supports the deposition of matrix along the entire process and the formation of many individual mineral collars [2].

The cytoskeletal system within an odontoblast includes 3 components, microfilaments (actin filaments), microtubules and intermediate filaments. The organization of these cytoskeleton components forms the unique morphology of odontoblasts and supports various cytological activities. All three components have been observed both in the cell body and in the odontoblast process. With the onset of odontoblast differentiation, microfilaments and microtubules concentrate at the apical pole of odontoblasts [4] and grow accompanying the formation and extension of an odontoblast process. In a mature odontoblast, a large amount of actin filaments form a

terminal web close to the site where the process originates from the cell body, and in the meanwhile, actin filaments stretch into the odontoblast process and the mini-branches [5]. Microtubules align parallel with the long axis of the odontoblast in the cell body and also form the odontoblast process in the core. Vimentin, a type III intermediate filament protein, exhibits a distribution change during odontoblast polarization that it was uniformly localized within the cytoplasm of pre-odontoblasts while accumulated at the apical pole of polarized odontoblasts [6]. In the meantime, intermediate filaments also align parallel along the axis of the cell body and form the odontoblast process in the core [5] with a similar pattern to microtubules.

However, apart from the aforementioned descriptions in odontoblast morphological change, only a few studies have been reported focusing on the odontoblast polarization process. Although some previous studies have proved that bioactive factors like the basement membrane, various growth factors and signaling transcriptional factors were indispensable for tubular dentin formation, their exact roles in regulating odontoblast behaviors remain unknown. Moreover, studies exploring possible signaling molecules participating in this process and induction signals that could promote this process are even less. Therefore, questions like how pre-odontoblasts initiate the polarization/differentiation process in response to signals and what types of signals are actually promoting this process are waiting to be answered.

1.2. Possible signaling factors related to odontoblast polarization*

As to the first question, there aren't enough publication to give us a clue. However, for other types of cells that also go through polarization process, like epithelial cells, neurons or migrating fibroblasts, their dynamic transition have been extensively studied and the underlying molecular mechanisms have been described as well. When we compare between epithelial cells and odontoblasts, multiple similarities can be found, including their features in cell morphology, development, function, and composition [7], thus it's reasonable to learn from the epithelial cells to explore the unknown facts of odontoblast polarity.

Epithelial cells can be divided into squamous, cuboidal and columnar epithelial cells based on cell morphology. The columnar epithelial cells exhibit a morphology similar to odontoblasts with a well-demonstrated apicobasal polarity, which is defined by 3 plasma membrane domains: apical, lateral and basal domains. The apical domains have the cellular processes and face the lumen or the outer environment to achieve material exchange. The lateral domains connect adjacent cells via specialized intercellular junctional structures. The basal domains adhere to the underlying basement membrane or extracellular matrix (ECM). The basal and lateral domains have similar components and are thereby named as basolateral domains [8].

---

* Modified with permission from "Cell polarization: From epithelial cells to odontoblasts" by Bei Chang, Kathy K.H. Svoboda, Xiaohua Liu, 2019. European Journal of Cell Biology, 98, 1-11, Copyright 2019 by Urban & Fischer.

While for odontoblasts, a apical-basolateral polarity has not be clearly defined or widely accepted. Some researchers used “apical pole” to describe the pole of odontoblast process which faces the pre-dentin/dentin, and “basal pole” to describe the pole that faces the dental pulp [1] in a similar way to the apical-basolateral polarity of epithelial cells. However, one group of researchers proposed that the polarity of odontoblasts was inverted to that of epithelial cells since they found both the transfection sites of influenza virus and vesicular stomatitis virus were opposite to those on the epithelial cell surface. Moreover, the distribution patterns of aquaporin 4 and aquaporin 5, a pair of epithelial polarity proteins, were also inverted on odontoblasts [9].

The formation of apicobasal polarity in epithelial cells is determined by an intricate signaling network, which includes the cytoskeleton, organelles, intercellular junctions, membrane lipids and the regulatory molecules. This signaling network has been extensively explored in previous studies, therefore, by learning how this network determines epithelial cell polarity, it’s possible for us to pick up some critical factors that may also participate in the odontoblast polarization process.

1.2.1. Cytoskeleton distribution

The distribution patterns of cytoskeleton elements in polarized epithelial cells are similar to those in odontoblasts. Actin filaments form the cortical belt (terminal web) encircling the most apical end of the lateral membrane domain and support apical junctions, in the meantime, they also form stress fibers and support focal contacts at the basal ends of the cells [10]. Microtubules undergo a dramatic rearrangement from a radial centrosomal array to a highly asymmetric distribution with distinct orientations

during the polarization of epithelial cells. The majority of microtubules are non-centrosomal and polarized with their plus ends stabilized at the basal cell cortex and minus ends anchored to cell-cell junctions (mainly AJs and desmosomes) or at the apical pole. The release of non-centrosomal microtubules and reassignment of microtubule organizing centers (MTOCs) from the centrosome to the apical membrane had been proposed to be related to γ-tubulin ring complexes [11, 12], or the formation of E-cadherin mediated AJs [13] or a PAR3-regulated physical hand-off of microtubule nucleators [14]. Another two minor microtubule populations include microtubules orientated apically from the centrosome positioned at the apical side of the nucleus, which might be required for apical protein trafficking, and microtubules forming the primary cilium where microtubules originate from the centrosome toward the tip of the cilium [15]. In polarized epithelial cells, a thick layer of intermediate filaments lies immediately below and within the terminal web, at the rootlets of the microvilli [16]. Besides, a few thin, isolated bundles of intermediate filaments extend along the apical half of the lateral domain, where they connect with desmosomes. A faint but distinct intermediate filament network has also been observed at the basal pole [17] where it might be anchored to hemidesmosomes [18] or focal adhesions [19].

Actin filaments and microtubules are both dynamic polymers that undergo rapid polymerization and depolymerization within the cytosol. Actin filaments are composed of G-actin subunits that orientated in the same direction, which results in a polarized surface lattice and two structurally distinct ends (barbed end and pointed end). The dynamic polymerization and depolymerization typically occur at the barbed end.

Polymerization of F-actin includes a nucleation process via formins and a branching process via Arp2/3, and the depolymerization process relies on ADF/cofilin. Myosins are the motor proteins on actin filaments, and most members of the myosin superfamily (except myosin-VI) move towards actin barbed ends. Microtubules have fast-growing plus ends and slow-growing minus ends. The minus ends usually bind to centrosome or other MTOCs, and their plus ends stretch to the plasma membrane and dominate the "dynamic instability". Dynein and kinesin are microtubule motors that move towards the minus ends and the plus ends, respectively, and they are somehow interdependent for their activities [20]. Cortical signals usually regulate microtubule activity via a group of proteins named microtubule-associated proteins (MAPs), among which +TIPS are the most critical ones. +TIPS are regulatory proteins that bind to microtubules at plus ends and own functions like regulating the stability of microtubules and/or generating pulling forces on microtubules. In contrast to actin and microtubules, intermediate filaments are formed by nonpolar structural units and display a much more stabilized status.

All three cytoskeletons contribute to epithelial cell polarity, while the function of actin and microtubules are much better known than intermediate filaments. Actin filaments and microtubules coordinate in establishing and maintaining cell polarity [13] and it seems actin filaments are critical in the initial symmetry-breaking process while microtubules build on and stabilize the asymmetry subsequently. From the initial cell-cell contact to the subsequent polarized cellular morphology establishment, actin filaments play manifold roles. For instance, actin filaments establish and sustain a polarized cell morphology via its dynamic polymerization and depolymerization at

specific sites, maintain the structures of cell-cell and cell-matrix adhesions by binding to various adaptor proteins, transport polarized molecules via its motors, reorientate and relocate organelles. Microtubules also contribute to epithelial cell polarity via multiple ways, mainly through the targeted transportation of polarized molecules to specific locations [21] and the generation of pulling forces for organelle positioning. Profound evidence had verified microtubule-based vesicular transport to the cell surface [22], and post-Golgi exocytic vesicles have been shown to associate with microtubules and their motor complexes. Moreover, microtubules might directly contribute to protein sorting and modulate the composition of transport carriers in forming distinct membrane domains [21]. Intermediate filaments were initially believed non-functional in epithelial cell polarization owing to their non-polar subunits, while recent studies found that septin family, the basic structural unit resembling intermediate filaments, is important for cell polarity in a number of cell types [23]. Moreover, intermediate filaments have been shown to participate in epithelial polarization via colocalizing with centrosome, mediating in non-centrosomal microtubules organization, directly binding to membrane proteins, participating in membrane trafficking [23], and acting as scaffolds for the interaction between extrinsic proteins and membrane proteins [16].

All three cytoskeletons function interdependently in various ways. Firstly, centrosome reorientation during cell polarization requires the cooperation of both microtubule-dependent centrosome centering and actin-dependent nucleus movement [13]. Then, ACF7, a cytoskeletal crosslinking protein that interacts with both actin and microtubules, mediates in guiding the parallel growth of microtubules along with actin

filaments and the targeted tether of microtubules to actin-rich cortical sites [24]. A actin motor protein, Myosin Va guides microtubules targeting to focal adhesion via interacting with EB1, a microtubule-associated protein [25]. In turn, microtubules regulate actin filaments via delivering Tea1/Tea4 to recruit formin (a actin polymerization protein) to promote actin polymerization [26], delivering dynamin to focal adhesion and promoting the disassembly of focal adhesion and the depolymerization of actin filaments [27], and regulating RhoA activity via RhoGEF11 to control the activities of both front and rear actin [28]. Meanwhile, intermediate filaments are also related with actin filaments and microtubules. The apical distribution of intermediate filaments was found to precede the polarization of actin filaments or microtubules, indicating a precursor signal inducing actin/microtubule polarization [16]. Also, intermediate filaments organization and movement require the assistance from actin and microtubule network and their motors, and in turn, intermediate filaments mediate the stress fiber formation and microtubule reassembly [29].

In odontoblasts, there was no such extensive studies that observed the cytoskeletal dynamics during the polarization process. Even though the disassembly and reassembly processes of the cytoskeletal elements and their inducing proteins could possibly be the same among various cell types, further studies are still needed to confirm their roles in odontoblasts.

1.2.2. Organelles translocation

The translocation of organelles during epithelial cell polarization is also similar to that in odontoblasts, which include nucleus, centrosomes, and Golgi apparatus. In

non-polarized cells, the centrosomes reside in the central area close to the nucleus, and the Golgi apparatus is usually adjacent to the centrosome. In a polarized epithelial cell, the nucleus resides at the basal half of the cell body, the centrosome at the apical surface above the nucleus [14], and the Golgi apparatus accompanies the movement of centrosome and remains adjacent to the centrosome. The relative centrosome-to-nucleus localization corresponds to the main polarization axis [30], and the relative Golgi-to-nucleus defines an axis of secretion relevant to the proper orientation of membrane trafficking [31].

Organelle translocation within the cytosol is directly achieved by cytoskeleton elements under the direction of regulatory factors, and all three cytoskeleton components participate in this process. Microtubules are critical forces in regulating nuclear position, especially the centrosomal microtubules. Their plus ends are anchored to cortical proteins via +TIPS including dynein, dynactin, CLASPs, IQGAP1 and APC, while their minus ends are directly linked to the nuclear envelope via liners of nucleoskeleton and cytoskeleton (LINC) to apply forces to modulate nuclear positioning [32]. Actin cytoskeleton contributes to nuclear positioning via increasing microfilament stability, regulating actomyosin contraction and self-reorganizing at specific sites to restrain nucleus movement [33, 34]. Besides, actin filaments can be directly linked to nucleus by SUN2 to position the nucleus, and myosin II-mediated actomyosin contraction may power and accelerate this process [35]. Intermediate filaments also participate in and exhibit a critical role in this actin-dominated nucleus movement [36, 37].

The centrosome movement precedes and might initiate nuclear translocation [38]. The location of the centrosome is regulated by PAR proteins and it contributes to epithelial polarity mainly by regulating the apical accumulation of microtubule nucleators and the formation of an apicobasal microtubule network [14]. Centrosome positioning requires an active force generated by both microtubule and actin [39]. Proteins mediating cytoskeleton-centriole include actin, dynein and TBCCD1, a centrosome-associated protein [40] and ninein, a microtubule-anchoring protein [41].

The reassembly, location and trans-Golgi transport of Golgi requires both microtubule and actin cytoskeleton [42]. For instance, Microtubules, together with its associated proteins, determine the location and organization of the Golgi ribbon around the centrosome during Golgi remodeling and allow a directed transportation to specific membrane domains. Apart from centrosomal microtubules, a subset of microtubules can be nucleated at the Golgi independent of the centrosome and their functions include assisting post-mitotic assembly of Golgi complex, post-Golgi trafficking and establishing cell architecture [43, 44]. Although the exact mechanism remains unclear, the formation of Golgi-derived microtubules was found associated with γ-tubulin [45, 46], microtubule-stabilizing protein CLASPs [45], AKAP proteins, and microtubule motor complex dynein/dynactin [47]. The actin cytoskeletons have multiple effect on Golgi. They facilitate post-Golgi transport by providing actin-based motors [48], prevent Golgi spontaneous swelling by providing mechanical stability, maintain the position of the Golgi by providing structural support through the dynamic instability of actin filaments by Arp2/3 and cofilin and assist in Golgi reconstruction [49].

The translocation of Golgi apparatus and the nucleus have been well documented during odontoblast polarization process, and their dependence on the cytoskeletal integrity has also been reported. However, underlying molecules that link the cytoskeleton elements to the organelles remain unclear, therefore, it's necessary for further studies to examine role of the aforementioned proteins in odontoblast polarization process.

1.2.3. Intercellular junctions

Intercellular junction is a characteristic of a polarized epithelial cell. There are several types of intercellular and cell-matrix junctions. Tight junctions (TJs), adherens junctions (AJs), desmosomes, and gap junctions are located at the intercellular space from apical to basal regions sequentially, while hemidesmosomes and focal adhesions are located between basal cell domains and underlying ECM. Despite the strict structural demarcation among the junctions, they are closely related during junction formation and epithelial polarity development [50].

Among those junction complexes, AJs mediate cell-cell adhesion and enable dissociated cells to selectively assort and reassemble to form organized tissues. Desmosomes are similar to AJs morphologically, and the differences lie in the location of the two junctions and the type of cytoskeleton they anchor, together with the relevant anchoring proteins. AJs link to actin filament via cadherin and catenin, while desmosomes link to intermediate filaments via plakophilin, plakoglobin, and desmoplakin. Hemidesmosomes also anchor to intermediate filaments. Connecting to desmosomes and hemidesmosomes, a network of intermediate filaments is formed

within the cytosol and it offers the cell with great tensile strength. Gap junctions bridge gaps between adjacent cells to create direct intercellular passageways and allow the direct communication of various molecules, ions, and electrical impulses.

TJs not only function as a “gate” to occlude intercellular gap for selective paracellular permeability but also as a “fence” to mechanically segregate diffusion of proteins and lipids within the lipid bilayer proteins and thereby define the boundary between apical domains and basolateral domains [51]. TJs are composed of transmembrane structural proteins that constitute the diffusion barriers, and cytosolic adaptor proteins that link the junctional membrane with the cytoskeleton proteins. Among the structural proteins are tetraspan proteins of the claudin family and three junctional MARVEL domain proteins: occludin, MARVELD2, and MARVELD3. Cytosolic adaptor plaque is a protein network that contains multiple protein-protein interaction motifs and interacts with cytoskeletons including actin filaments and microtubules. Zonula occludens 1 (ZO1), ZO2, ZO3, cingulin, and JACOP are among the adaptor protein group. Both structural proteins and adaptor plaque are indispensable to TJ formation. Briefly, occludins mainly function in maintaining the stability and barrier function of a TJ, claudins mainly regulate the permeability [52], and ZOs mainly function in TJ assembly. ZO-1 regulates TJ formation in various ways, including assembling occludin and claudin as scaffolding proteins, binding to and regulating components of the cortical actin cytoskeleton and promoting cadherin-mediated cell-cell adhesion via regulating the spatial organization of tension acting on sites of adhesion in a RhoA/ROCK-dependent way [53]. Moreover, ZOs can also be imported into the

nucleus and regulate the expression of genes relevant to epithelial growth and differentiation by modulating the activities of transcription factors [54]. Some other TJ-related proteins, like ZONAB, Rab13, and cingulin, can also control cell proliferation by participating directly in signaling cascades or regulating gene expression in the nucleus [55]. It's noteworthy that ZO proteins are not exclusively localized to TJs, they are also components of AJs in non-epithelial cells like fibroblasts or cardiomyocytes, and it is prevalently believed that ZO proteins directly interact with AJ proteins during AJ assembly and subsequently recruit TJ-related proteins to form tight junctions [56]. ZO-1 has also been proposed as a gap junction partner that acts as a scaffold to recruit signaling proteins or mediate in regulating the size of a gap junction.

All four intercellular junctions including AJs [57], TJs, gap junctions [58, 59], and desmosomes [60, 61] have been observed between adjacent odontoblasts, however their formation and function in odontoblasts remain unclear. For example, the structure of TJs (macular or continuous) in odontoblasts remains controversial since different morphologies have been reported from different studies, and their function (barrier only or also a inducer for odontoblast polarization) is unknown [62-66]. Another example lies in the expression of cadherins, a key factor of AJs [67]. One study reported that E-cadherin expression was absent in differentiating odontoblasts and weak in mature odontoblasts, while N-cadherin can be found in differentiated odontoblasts and sub-odontoblastic Hohl's cells, besides, both proteins are down-regulated in adult teeth, but N-cadherin can be re-expressed in the pulp of carious or injured teeth [57]. However, contradictory results were also reported from *in vitro* studies that E-cadherin was up-

regulated by Nfic with the differentiation of odontoblast, wheras N-cadherin was down-regulated in the meantime [68].

1.2.4. Polarity complexes

There are three groups of protein complexes involved in epithelial polarity, including PAR6/PAR3/aPKC complex, CRB/PALS1/PATJ complex, and SCRIB/LGL/DLG complex [69-71]. The CRB and PAR complexes determine the apical domain of epithelial cells and exclude the SCRIB complex from the apical domain, while the SCRIB complex expels CRB and PAR complexes at the basolateral domains. This mutual exclusion between the polarity complexes results in the establishment and maintenance of apicobasal polarity [70].

In polarized epithelia, the PAR and CRB complexes locate primarily close to the TJs [71]. The PAR complex is the major protein complex that dominates the polarization process [70, 72]. PAR3 is recruited to the initial sites of cell-cell contact, and serves as a scaffold protein to recruit follow-up proteins to form apical junctions, including PAR6-aPKC. PAR6 functions as a conjugator that brings TJ-related proteins together [72]. aPKC plays a crucial role in the establishment of cell polarity in various biological contexts. In mammalian cells, aPKC is recruited to the initial spot-like AJs via a direct interaction with PAR-3, JAM-1, and nectin-1/3 upon cell-cell contact [73], assists in promoting the transition of primordial spot-like AJs into continuous belt-like AJs via myosin II modulation [74], and finally accumulates in TJs as polarization progresses. Apart from its role in junctional development, aPKC is fundamental in regulating cell

polarity owing to its kinase role in phosphorylating various proteins. A detailed discussion of aPKC targets has been summarized recently [75].

The CRB complex associates with TJs through the interactions of PATJ with ZO-3, claudin1, and JAMA [76], and contributes to the apical junction stabilization, apical membrane differentiation, and cilium formation in epithelial cells [77]. Over-expression of CRB3 induces TJ formation in non-polarized epithelial cells [78]. PALS1 acts as a linker of CRB3 and PATJ [69].

The SCRIB complex locates at the basolateral pole of a polarized epithelial cell. Suppression of SCRIB [79] or DLG [80] expression causes a delay in TJ assembly. After the detachment from the PAR6/aPKC dimer, LGL moves towards the basolateral domain where DLG and SCRIB localize, therefore creating a direct connection between the apical PAR complex and the basolateral SCRIB complex. SCRIB, LGL, and DLG are localized in the basolateral domain of epithelial cells. Although the exact physical interactions remain unclear [69], it has already been found that SCRIB associates physically with DLG via a protein termed GUK Holder, and physical interactions between SCRIB and LGL2 can also occur in polarized epithelial cells. Suppression of SCRIB [79] or DLG [80] expression in epithelial cells causes a delay in tight junction assembly and affects the mesenchymal-to-epithelial transformation. After LGL dissociates from the PAR6/aPKC dimer, it translocates to the lateral membrane, where it interacts with DLG and SCRIB, and therefore creates a direct connection between the basolateral SCRIB/LGL/DLG complex and the apical PAR complex.

In odontoblasts, however, relevant studies are scarce. Up to now, none of the PAR complexes have been confirmed in odontoblasts, although PAR3 has been detected at the proximal TJs in ameloblasts and was proposed to mediate in the formation and maintenance of the proximal TJs [81]. Similarly, no reports discussing the expression of CRB/PALS1/PATJ and SCRIB/LGL/DLG complexes in odontoblasts have been found. Therefore, whether such polarity complexes exist in odontoblasts and participate their polarization process remain unknown.

1.2.5. Regulatory factors

The most extensively characterized Rho GTPases related to epithelial polarity include RhoA, Rac1, and Cdc42. As small GTPases, the active or inactive status of Rho proteins is regulated by various types of GTPase-binding proteins, while they also modulate each other's activity via their complex crosstalk [82, 83]. As the major regulatory molecules in epithelial polarization, Rho GTPases regulate cytoskeleton dynamics, modulate organelle translocation via direct and indirect ways, interact directly with junction proteins and polarity complexes [84, 85] to establish epithelial polarity.

The downstream molecules of Rho GTPases mainly target actin and microtubules. Their effect on actin activities have been extensively described [86-88]. One RhoA effector ROCK directly phosphorylates actin regulators such as myosin phosphatase and LIM domain kinase (LIMK), which regulate actin contractility and depolymerization, respectively. Another RhoA effector are the formins that regulate unbranched actin filaments nucleation and assembly. WASP and WAVE are effectors of Cdc42 and Rac1, respectively, and they promote actin branching to augment the amount

of free barbed ends to accelerate actin polymerization [86]. Actin dynamics also regulate Rho GTPase activity and this feedback loop ensures a precise regulation of actin [13]. Meanwhile, Rho GTPases also regulate microtubule dynamics [21, 89, 90]. RhoA regulates microtubule stability through mDia-APC-EB1 pathway [91], and integrin-FAK mediated cell adhesion facilitates this process [46]. Moreover, ROCK phosphorylates MAP-2 and Tau, two microtubule-associated proteins critical in microtubule dynamics [89]. Rac1 and Cdc42 regulate microtubule polarization via stabilizing microtubules, providing the docking sites for microtubule plus ends and regulating the location of CLASPs. Microtubules also regulate Rho GTPase. Microtubule outgrowth activates Rac1. Microtubule depolymerization activates RhoA at focal adhesions and promotes the formation of contractile actin bundles via GEF-H1 [92, 93].

Rho GTPases regulate organelle translocation mainly through their modulating roles in cytoskeleton dynamics, apart from that, Rho GTPases also have direct roles on organelles [94, 95]. Both Cdc42 and RhoA are localized at the Golgi apparatus. Cdc42 localizes at the Golgi apparatus and ER, and regulates cell polarity by controlling the secretory and endocytic transport [94]. Apart from accumulating Cdc42 as a reservoir to supplement the membranous Cdc42, Golgi-located Cdc42 also promotes the polarized transportation via regulating cargo sorting and carrier formation within the Golgi cisternae [95]. Moreover. RhoA also influences the morphology and function of Golgi [95]. Constitutive overexpression of RhoA disrupted Golgi ribbon integrity and increased Rab6-positive carriers issued from the Golgi [96] , which may associate with a RhoA GAP, DLC3 [97].

Rho GTPases interact directly with polarity complexes [84, 85]. Rac1 activity is higher at AJs and lower at TJs, which is probably owing to the PAR3-mediated inhibition of Tiam1-Rac1activity, a process required for tight junction biogenesis [85, 98]. Also, Rac1 is lower in apical membranes compared to lateral membranes, because Rac1 GAP chimaerin reduces Rac1 activity apically [99]. RhoA activity at apical membranes is also limited that it is inactivated by Rac1 via recruiting p190RhoGAP to cell-junctions to help define the apical domains [84]. Also, PAR6 targets RhoA degradation at tight junctions, which limits the local RhoA activity. Cdc42 is vital in the apical localization of PAR complex and the establishment of epithelial polarity. An earlier theory proposed that Cdc42 promoted apical differentiation through binding to PAR6 and caused its conformational change, which enhanced its affinity for aPKC substrates. Cdc42 also increased the phosphorylation activity of aPKC and subsequent PAR3 activation, resulting in the correct positioning of the apical-basolateral border. However, later studies showed the interruption of Cdc42-PAR6 interaction did not impair aPKC activity. Therefore, the function of Cdc42-PAR6 in aPKC stimulation remains unclear. Moreover, a network that involves Cdc42, Tuba, annexin2 and PAR complex guides Cdc42-dependent exocytosis and targeted apical transportation [100], resulting in apical localization of CRB and exclusion of apical PAR3 to define the apicobasal border [101].

Direct interaction between Rho GTPases and junction adaptor proteins have also been reported, which assist in transferring junction signals to the cell interior [102]. Rac1 is recruited and activated by nascent cell-cell contacts, and it stimulates lamellipodia

formations which initiates AJ formation. As AJs mature, the intercellular accumulation of E-cadherin widely diminishes Rac1 activity [102]. Rac1 moving in the lamellipodia promotes Arp2/3-mediated actin polymerization, and drives the expansion of cell-cell adhesion [103], together with the concurrent activation of RhoA/ROCK/myosin pathway [104]. RhoA promotes both the organization and the maintenance of tight junctions [51, 105]. First, E-cadherin-based puncta clustering is the initiator of apical junction formation and it's dependent on RhoA/mDia-dependent actin polymerization, as well as Rac1-WAVE-Arp2/3-dependent and Cdc42-NWASP-Arp2/3-dependent pathways. Second, the direct interactions between actomyosin and TJ plaque proteins stabilize the junctions and provide the force against the disruption of intercellular junctions. Third, Rho GEFs p114RhoGEF [106] and ARHGEF11 [107] are recruited by adaptor proteins JACOP or ZO-1 to mediate the formation of junctions. Last, RhoA regulates contractile activity via associating with ROCK/cingulin/myosin complex or ATJ/Lulu2 complex, which causes the expansion and linearization of initial AJ-like junctions. The formation of the circumferential actomyosin belt and the specialized morphology of a polarized epithelial cell are also regulated by RhoA [106, 108]. However, there is also evidence suggesting that RhoA negatively regulates TJ activity. GEF-H1, the microtubule-related RhoA GEF, was inhibited by association with cingulin, and can promote TJ disassembly [109, 110]. Cdc42 is also a critical factor in tight junction assembly. The activated Cdc42 binds to PAR6 and the Cdc42-PAR6 complex activates aPKC, which results in PAR3 phosphorylation and PAR3-PAR6-aPKC complex dissociation. PAR3 remains at the tight junction area while the PAR6-aPKC complex migrates to the apical membrane.

This process drives the accumulation of apical signaling proteins and the construction of TJs, during which a Cdc42 GEF, Dbl3 plays a critical role. Dbl3 is not indispensable in tight junction formation, it also activates the PAR3-PAR6-aPKC complex that promotes apical PAR3 expulsion and apical membrane differentiation, thereafter regulating the size of apical domains and the position of TJs. Dbl3 localizes along the apical membrane and is enriched apical to tight junctions similar to other apical proteins [111]. Other Cdc42 GEFs like Etc2 and Tuba are involved in apical polarization. Previously Etc2 was proposed to regulate Cdc42 activity and associate with the PAR3-PAR6-aPKC complex in the initial establishment of epithelial polarity [112], but a later study showed that it specifically regulated RhoA signaling at AJs [113]. Tuba is recruited to TJs by ZO-1 and tricellulin, and it modulates the apical actin network by binding to N-WASP [114]. Furthermore, a Rac1/Rich1 (a Cdc42 GAP) complex is also recruited to and associated with the CRB complex and PAR3 to sustain the stability of tight junction by precisely controlling the local Cdc42 activity [115].

Although small GTPases are a group of proteins that exist generally in various types of cells and participate in cytoskeleton regulation, their distribution and regulatory function in odontoblasts have seldomly been reported. Previous studies indicated that RhoA [66, 116] and Cdc 42 [116] uniformly distributed in odontoblasts before and during cytodifferentiation stages, and Rac1 was found to uniformly expressed in odontoblast at initiation stages but disappeared at cytodifferentiation stages [116]. However, the exact roles of these factors during the odontoblast polarization process remain unknown.

Under normal circumstances, the acquisition of the fully polarized state is initiated by the formation of cell-cell contacts between epithelial cells [69, 85, 105, 117-120], although contact-independent polarization signals can also come from LKB1-activated epithelial cells or integrin-mediated cell-matrix interactions. Take cell-cell contact for example, after this signal is perceived, adhesion proteins (like nectin and E-cadherin) and small GTPases (like Cdc42) are activated. Adhesion proteins recruit scaffolding proteins and polarity proteins to the site of initial tight junctions and establish the apical border. Small GTPases not only leads to sequential phosphorylation and movement of polarity complex components (like aPKC, LGL, PAR3), but also regulate cytoskeleton dynamics to assist in establishing the intercellular junctions and transporting polarity complexes towards destinated membrane domains to achieve apicobasal polarity. Moreover, orderly organized cytoskeleton elements form the polarized cell morphology and take responsibility in organelle translocation within the cytosol, leading to the unidirectional secretion pattern.

Therefore, it's demonstrated that epithelial cell polarization is realized by a complex signaling network that requires the cooperation among small GTPases, polarity complexes, cytoskeleton elements and organelles. Using this extensively explored network as a reference, we are able to underline the gap of knowledge in odontoblast polarization. It is found that despite there are some similarities in morphology between those two types of cells, many characteristics of epithelial polarity at the molecular level are missing or have not been found in odontoblasts, such as the function of intercellular junctions, the existence of polarity complexes and the regulatory role of small GTPases.

We hope this comparison may propose an orientation for future odontoblast studies, which will guide the development of new strategies in regenerative dentistry.

1.3. Signals that may induce odontoblast polarization

1.3.1. Biochemical factors

As to the second question what signals are responsible for inducing odontoblast polarization, early studies demonstrated that the interaction between dental mesenchyme and dental epithelium was undoubtedly one of them. It's proposed that 3 major components within the epithelio-mesenchymal interaction could determine the fates of dental mesenchymal cells, which include the inner dental epithelium, basement membrane and growth factors [1]. In the very beginning, dental epithelium was believed indispensable to initiate odontoblast polarization, however, later studies had found that non-dental epithelium also possessed such capabilities. When in contact with non-dental epithelium, the dental mesenchymal tissues would first promote the transformation of those non-dental epithelium into an inner dental epithelium, which in turn induced the dental mesenchyme to differentiate into odontoblasts.

The importance of the epithelio-mesenchymal basement membrane was recognized when it's found that removal of this basement membrane greatly impeded the dental mesenchyme differentiation process. When dental mesenchyme was co-cultured with dental epithelium directly *ex vivo* after removing the basement membrane, the removed basement membrane would be reconstructed before the initiation of dental mesenchyme differentiation [121]. Moreover, it's demonstrated that the epithelio-mesenchymal basement membrane was a dynamic structure that its components changed

accompanying the odontoblast polarization process, for example, the disappearance of collagen type III, the modification and turnover of glycosaminoglycans, and the restricted distribution of fibronectin at the apical pole of polarized odontoblasts which surrounded dividing pre-odontoblasts [6]. Besides, the basement membrane got gradually degraded with the onset of predentin mineralization [122].

Various growth factors from epithelium were also believed to play critical roles in odontoblast polarization, including the TGF-β superfamily [123], EGFs [124], NGFs [125], and IGFs [126]. It's worth noticing that although the participation of these epithelium-related growth factors had been confirmed in early studies with immunolocalization and/or in situ hybridization techniques, their exact functions in initiating odontoblast polarization remained unclear until more advanced techniques, especially the gene-modified animal models, were developed. Multiple transcriptional factors or effector proteins have been identified using this technique, including Runx2 [127, 128], TWIST1 [2, 129], DSPP [130], DMP1 [131, 132], BMP4 [133], SMAD4 [134], Wnt [135], Notum [136] and Dlx3 [137]. Expression of those factors are precisely and timely controlled in normal conditions, while artificial deletion or knock-down their expression can lead to disordered dentinogenesis. Common phenotypes include disorganized odontoblast alignment, impaired odontoblast polarity and decreased expression of dentin-specific proteins. Moreover, retarded dentin growth is often detected as well, shown as a thinner layer of dentin with disorganized dentinal tubules, and sometimes bone-like dentin mass forms in the pulp.

It should be noted that even though *in vivo* animal studies have potently proved the participation of various growth factors in odontoblast polarization, the underlying mechanisms that how they regulate the polarization process remain unclear owing to the complexity of *in vivo* environments. In the meantime, numerous *in vitro* studies have also been performed where various growth factors were confirmed favorable in promoting odontoblast differentiation, whereas, on the 2D culture substrate odontoblast polarization behaviors could hardly be recapitulated. Therefore, the role of those biochemical factors on odontoblast polarization remain largely unclarified at this moment.

1.3.2. Biophysical factors

In recent years, the advancement in bioengineering techniques have proved that biophysical factors may also participate in the regulation of odontoblast polarization and differentiation [138-140]. For example, researchers managed to mimic the natural "mesenchyme condensing" process by condensing embryonic mesenchymal cells mechanically [141] or compacting mouse bone marrow stromal cells within thermo-responsive compressive scaffolds [142]. Mechanically condensed or compacted cells expressed increased level of odontogenic markers and formed dentin-like tissues, indicating that spatial restriction of mesenchymal cells could promote their odontogenic-lineage differentiation abilities.

Moreover, the generation of 3D culture environments further confirmed the role of spatial factors in odontoblast polarization. Dental cells cultured on natural dentin slides where dentinal tubules were chemically or physically enlarged could display an

odontoblast-like cell morphology [143, 144]. In another study, pelleted dental pulp cells were cultured on Millipore filters and it turned out that the layer of cells adjacent to the filters also exhibited a odontoblast-like morphology with an elongated cell body and a cytoplasmic process extending into the pores of filter. Moreover, the nucleus/cytoplasm ratio of these cells was increased, and the nucleus located eccentrically apart from the filter, further implying a polarized cell morphology [138]. Another example worth mentioning is dental stem cells seeded on synthetic tubular scaffold managed to polarize like odontoblasts and extend cellular processes into the microchannels. Moreover, dental pulp tissues cultured on the same scaffolds were able to deposit collagen and form natural dentin-like mineralized tissue with organized tubular structure. On the contrary, dental tissues cultured on scaffolds without the tubular architecture only formed bone-like mineralized tissues and the dental cells were entrapped within the tissue, displaying a osteocyte-like morphological pattern [139]. All these *in vitro* studies have demonstrated that biophysical signals also possess the ability to induce odontoblast polarization, and moreover, those biophysical factors might be quite beneficial for tubular dentin regeneration work.

In summary, apart from the morphological change, the polarization process of odontoblasts remains largely ambiguous to date, especially the signaling molecules participating in this process and the induction signals that could promote this process. The molecular mechanism as to how the various cytological components within a odontoblast are organized to obtain the polarized morphology could be learnt from the extensively studied epithelial cells. The induction factors have been found to include

both biophysical and biochemical factors, but what specific factors are truly effective in inducing odontoblast polarization remain unclarified. Therefore, this research project is inspired. We aim to identify both biophysical and biochemical factors that possess the capability to promote odontoblast polarization and differentiation, which could benefit future tubular dentin regeneration studies.

2. ESTABLISHMENT OF A CLEAN AND BIO-MIMIC IN VITRO PLATFORM FOR SINGLE HDPSC OBSERVATIONS*

2.1. Introduction

Cells in the body reside in a distinct 3D microenvironment with a well-organized hierarchic architecture ranged from nano to macro scales. When cells are removed from the *in vivo* microenvironment and are cultured on an artificial matrix *in vitro*, the cells usually cannot retain their 3D physiological morphologies. Odontoblasts are a vivid example. Odontoblasts display a high columnar cell morphology with a evident cytoplasmic process *in vivo*, however, when they were extracted from a dental tissue and cultured on a 2D tissue culture flask, they rapidly lost their long processes and the characteristic columnar morphology [145, 146] and their function and gene expression were likely changed as well.

It's well known that cell morphology is one of the crucial factors that regulate many biological processes, including stem cell commitment and selective differentiation [147, 148]. Therefore, to explore how various biophysical or biochemical factors regulate odontoblast polarization and differentiation *in vitro*, a successful recapitulation of odontoblast morphology is undoubtedly a prerequisite. To achieve this goal, a bio-inspired 3D platform capable of precisely mimicking the microenvironment that

* Modified with permission from "Bio-Inspired Micropatterned Platforms Recapitulate 3D Physiological Morphologies of Bone and Dentinal Cells" by Chi Ma, Bei Chang, Yan Jing, Harry Kim, Xiaohua Liu, 2018. Advanced Science, 5, 1801037, Copyright 2018 by WILEY-VCH Verlag GmbH & Co. KGaA, Weinheim.

accommodate odontoblasts seemed necessary, and both the hierarchic architecture and composition of the ECM needed to be included.

Dentin forms a unique microenvironment for odontoblasts. It's a mineralized tissue and the ECM has a hierarchic structure in which the well-defined tubules, which have a diameter of 3-5 micrometers, were embedded in a highly interconnected nanofibrous network [149, 150]. Reconstructing such a hierarchic architecture using biodegradable materials and integrating it into a biomimetic 3D platform was a considerable challenge. Conventional approaches using synthetic hydrogels and collagen-based matrix could form 3D fibrous network [151-153], however; those scaffolding materials were not capable of mimicking the tubular microstructures of the dentin ECM. Consequently, to date, there is no suitable platform that can recapitulate the morphologies of odontoblasts *in vitro*.

Moreover, to focus on the influence of each regulatory factor on odontoblasts, it's important to construct a platform that is capable to shield signal interference from other factors. Traditional *in vitro* culture methods could not get rid of cell-cell contact, which plays critical roles in various cytological activities, therefore, the effects presented to public were actually the synthetic effect of multiple factors within the microenvironment. Micropatterning technique, which allows the isolation and accommodation of individual single cells, offers an alternative way for *in vitro* cell studies. This technique has been widely used to control cell-material interactions within a micro-domain [154-158], thus it could be a potential tool to fabricate a clean platform for our *in vitro* studies. Currently, most of the micropatterning methods are limited to

fabricate 2D substrates using non-biodegradable materials, such as polydimethylsiloxane (PDMS), polyacrylamide, and polystyrene, while micropatterns constructed on a nanofibrous substrate mimicking the hierarchic architecture of dentin ECM have not be achieved [159-161].

Herein, we designed and developed a unique approach to develop a 3D ECM-like micropatterned matrix as a physiologically relevant 3D platform to recapitulate the dentin structure and induced odontoblast cell morphology *in vitro*. The bio-inspired micropatterned matrix precisely mimiced the hierarchic 3D tubular architecture as well as the compositions of the dentin ECM. In addition, the synthetic micropatterned matrix was capable of precisely controlling one single cell within a microisland, providing an excellent platform for our next-step odontoblast studies. Using this bio-inspired 3D platform, we were able to explore the behaviors of a single hDPSC in a *in vivo*-like microenvironment.

2.2. Materials and Methods

2.2.1. Micropattern fabrication

GelMA was synthesized by dripping 10 ml of methacrylic anhydride (Sigma, 276685) to 100ml 10% gelatin (sigma, G9382) -PBS solution at 40 °C. After 3 hours' stirring, the solution was diluted to 2% with PBS and dialyzed against distilled water using 12-14 kDa cutoff dialysis tubing at 40 °C for 1 week. The dialyzing water was changed every 12 hours. The GelMA was lyophilized and stored at -20 °C.

To synthesize FITC-conjugated GelMA, 0.5 g GelMA and 10 mg fluorescein isothiocyanate (FITC) (F7250, Sigma) were dissolved in 10ml borate buffer (pH=9.5) at

37°C, respectively. The FITC solution was then added into the GelMA solution slowly with constant stirring. The mixed solution was allowed to react for 12 hours at 37°C and dialyzed against distilled water using 12-14 kDa cutoff dialysis tubing for 4 days. The dialyzing water was changed every 12 hours. The FITC- GelMA was lyophilized and stored dry at -20 °C.

Then the GelMA was used to fabricate a nanofibrous matrix using the electrospinning technique. The FITC-labeled GelMA and non-FITC-labeled GelMA (1/9) were dissolved in the mixed solvent of hexafluoroisopropanol / acetic acid / ethyl acetate / water (volume ratio = 5/2.5/1.5/1) with a concentration of 20 % w/v. The solution was centrifuged at 15000 rpm for 3 minutes and the clear supernatant was used for following electrospinning process. The electrospinning process was carried out with the electrospinning system (SPRAYBASE® PLATFORM, Ireland) at room temperature through a metallic spray tip (22G); the voltage of 12 kV was insured by a power supply (Gamma High Voltage, USA); the feed rate was constant at 0.5 ml/h by a digital controlled infusion pump (Cole Plamer Inc, USA); and the electrospun nanofibers were collected onto a drum (30 cm in diameter) covered with aluminum foil while the drum was rotating at a speed of 80 rpm. The distance between the drum collector and the spray tip was 10 cm. After 6 hours, an electrospinning matrix of certain thickness was obtained.

Afterwards, a chemical crosslinking step was carried out immediately. The electrospinning matrix of FITC-GelMA with the foil attached was incubated into the precooled crosslinking medium of acetone/water (95/5) with 2.5 mM 4-

morpholinoethanesulfonic acid (MES), 3 mM N-(3-Dimethylaminopropyl)-N′-ethylcarbodiimide hydrochloride (EDC) and 0.5 mM N-hydroxysuccinimide (NHS) for 24 hours in 4°C. After that, the crosslinked electrospinning matrix was incubated in 50mM glycine aqueous solution for 1 hour at room temperature to neutralize the unreacted EDC. Subsequently the crosslinked matrix was washed 3 times by distilled water (15 minutes each) and dehydrated in absolute ethanol. The dehydrated samples were dried into the vacuum oven at 37°C for 30 minutes and stored in -20 °C.

To fabricate the micropatterns, a UV-initiated photolithography technique was employed. The crosslinked FITC-GelMA electrospinning matrix was cut into 1 × 1cm pieces. After the foil was carefully removed, the matrix was smoothed out on a glass slide. Then 10 μl of polyethylene (glycol) diacrylate (PEGDA) aqueous solution (20%) containing 1% 2-hydroxy-4’-(2-hydroxyethoxy)-2-methylpropiophenone) (Sigma, 410896) was added to the gelatin matrix. Next, a photomask (Digidat, Inc. CA. USA) was covered on the FITC-GelMA electrospinning matrix, and the photomask-gelatin matrix-slide complex was exposed to a UV light (CS2010, Thorlabs. Inc.) with a power of 40 mW/cm^2 for 60s. Afterwards, the micropatterned matrix was immersed in distilled water for 1 hour to wash off the unreacted PEGDA, and soaked into 75% alcohol for 30 minutes for sterilization, which were then ready to use in cell seeding.

In order to generate microchannels on the micropatterned scaffolds, NF-MP scaffolds were immersed into absolute ethanol for 30 minutes for complete dehydration and then placed on a polyethylene naphthalate (PEN) Frame Slide (Leica, 11600289) and dried in vacuum oven at 37°C for 15 minutes. The PEN Slide, which loosely

attached the NF-MPs, was placed under a Leica Laser Microdissection (LMD 7000) system and controlled with the software (Leica micro-dissection V7.5.1), from which the morphology of the NF-MPs could be observed. To generate dentinal tubule-like microchannels on the NF-MPs, the Laser Screw mode was selected, and a 5 μm^2 circle was drawn in the center of a micropattern on the software screen to mark where the laser targeted and drilled. At least 800 microchannels were drilled on each micropatterned scaffold. After the laser-drilling process, the NF-MT scaffolds were carefully removed from the PEN Frame Slide and soaked into 75% alcohol for future use.

To conjugate BMP-2 proteins to the GelMA nanofibers, 4-(N-Maleimidomethyl) cyclohexane-1-carboxylic acid 3-sulfo-N-hydroxysuccinimide ester sodium salt (Suflo-SMCC) was used as the crosslinker. After 4 mg Suflo-SMCC was dissolved in 1 ml PBS, the gelatin matrix was immersed with the Suflo-SMCC solution for 1 hour at room temperature for activation. Then the gelatin matrix was washed with PBS for 3 times and incubated in 100 ml BMP-2 solution (50 μg/ml) at 4°C for 1 hour. The resultant nanofibrous matrix was washed with sterile PBS and air-dried in the cell culture cabinet. Afterwards, the UV-initiated photolithography was performed on BMP-2-conjugated gelatin nanofibers.

2.2.2. Cell culture and cell seeding

Human dental pulp stem cells (hDPSCs) were a gift from Dr. Songtao Shi, The University of Pennsylvania School of Dentistry. The cells were isolated from surgical waste (extracted human wisdom teeth) that was approved by IRB (Protocol# USC IRB #HS-07-00701). HDPSCs were cultured in an ascorbic acid-free α-modified essential

medium (a-MEM) (GIBCO, Invitrogen, Carlsbad, CA, A1049001) supplemented with 10% (v/v) FBS (Gibco, #26140079) and 1% penicillin/streptomycin (Sigma, #P333) and maintained in a humidified incubator with 5% CO2 at 37 °C. The culture medium was changed every 2 days, and hDPSCs of passage 3-5 were used for following experiments.

Slides loaded with nanofibrous micropatterns (NF-MPs) were cut to a size that fits into a 6-well plate and an ImmEdge™ hydrophobic barrier pen was used to draw a square frame around the NF-MPs to prevent liquid flow during cell seeding. Immediately afterwards, those slide fragments were immersed in 70% alcohol for 30 minutes for sterilization and then washed with sterile PBS for 3 times. After trypsin digestion and resuspension, 100 μl cell suspension that contained 2×104 hDPSCs was evenly dripped within the square frame on the slide. The 6-well plate was incubated at 37°C for 60 minutes and then the slides in the plate were gently washed with culture medium for several times until no cells were detected outside the micropatterns under an inverted differential interference contrast (DIC) microscopy. Each well of the plate was pipetted with 3 ml culture medium and returned to the incubator. A secondary seeding process was performed 2 hours after the first seeding when necessary. To prevent cell proliferation on micropatterns, aphidicolin (0.5 mg/ml, Sigma, #A0781) was added to the culture medium 6 hours after cell seeding, and the medium was changed every 3 days. For hDPSCs differentiation assay, 1 mM dexamethasone, 50 mM ascorbic acid-2-phosphate, and 10 mM β-glycerophosphate were added to the medium and changed every 3 days [162].

2.2.3. Immunofluorescence staining and ALP staining

For actin staining, NF-MPs were fixed with 4% PFA and permeated with 0.3% Triton X-100. Afterwards, samples were blocked with 5% goat serum for 30 minutes at room temperature and then without washing, incubated with 10 U/ml CF633 phalloidin (Biotium, 00046) for 1 hour at 37 °C. PBS wash was then repeated for 3 times (5 minutes each) to remove residual phalloidin. For nuclear staining, samples were immersed into 1 μg/ml Hoechst 33342 (Thermo Scientific, 62249) for 10 minutes at room temperature and washed with PBS for 3 times (5 minutes each). For immunofluorescence staining, fixed NF-MPs were permeated with Triton X-100 and then blocked with 5% goat serum for at least 4 hours at room temperature to prevent non-specific staining. Afterwards, samples were incubated with primary antibodies with 2% goat serum at 4°C for overnight. Primary antibodies include anti-Integrin beta 1 antibody (1:1000, Abcam 179471), anti-vinculin antibody (1:150, Abcam 129002) and anti-BMP-2 antibody (1:100, Abcam 14933). Then samples were washed with PBS and immersed into Alexa Fluor Plus 555 secondary antibodies (1:200, Invitrogen, A32732) with 1% goat serum (1:200, Invitrogen, A32732) for 2 hours at room temperature. Then samples were smoothed out on a glass slide, immersed with ProLong™ Gold Antifade Mountant with DAPI (Invitrogen™ P36930) and mounted with coverslip (CoverWell™ Imaging Chamber Gasket) for confocal observations.

ALP staining was operated following manufacturer's guidance (Sigma, #85L2). Briefly, NF-MPs were washed with PBS and fixed with citrate buffered acetone (60% v/v) for 5 minutes, followed by PBS wash for 3 times (5 minutes each). Next, the NF-

MPs were immersed in the ALP staining solution for 30 minutes at room temperature. The nuclei were stained with 1 μg/ml Hoechst 33342 (Thermo Scientific, #62249) for 20 minutes. ALP-positive single cell ratio was calculated by dividing the number of ALP-positive single cells to the number of total single cells. To examine relative ALP intensity, each NF-MP sample was scanned under both bright field channel and fluorescence channel. By referring to both bright field and fluorescent images, ALP-positive microislands occupied by single cells were captured and exported to ImageJ software for quantitative analysis following a previous protocol [159, 163]. Briefly, all the bright field ALP images were converted to 8-bite images and the gray values of the pixels within the cell outline were regarded as the transmission intensity (I), while the control (I0) was determined from the corresponding nanofibrous background. The relative ALP activity of a cell was calculated by A=Scell lg (I0/I), where Scell is from the number of pixels covering the spreading area of the corresponding cell, which was also generated by ImageJ software. At least 30 ALP-positive cells on each sample were collected and measured.

2.2.4. Confocal observation and SEM observation

For Confocal observations, directly mounted samples were used for recording the top-view images with a high-resolution confocal microscopy (TCS SP5, Leica, Buffalo, USA). Three samples included at least 300 microislands were collected to measure the cell occupation ratio which was calculated as the percentage number of microislands that accommodated cells. A similar number of microislands were used when examining cell spreading area within each microisland that accommodated single cells. To obtain the

high-quality lateral view images of cells on microislands, the stained NF-MP samples were dehydrated in 30% sucrose aqueous solution, embedded, and processed using frozen microtome sections. Sections with a thickness of 30 μm were collected and immediately immersed with ProLong™ Gold Antifade Mountant and mounted for confocal observations. At least 90 lateral images from 3 samples were collected and measured for the lengths and diameters (the diameter at the half length) of the cellular processes. For cellular process analysis, we considered a cytoplasmic extension as a cellular process when the distance between its distal end and the cell body was more than 5 μm. High-resolution images were recorded in the stack mode with a step size of 0.4 μm. The image files were exported and used for 3D reconstruction with Imaris 9.0 software.

For scanning electron microscopy (SEM) observation, each sample was dehydrated with a graded ethanol solutions (50% alcohol for 10 minutes, 70% alcohol for 10 minutes, 95% alcohol for 30 minutes, and 100% alcohol for 30 minutes) and dried in a vacuum oven. The dried samples were coated with gold nanoparticles using a sputter coater (SPI-module Sputter Coater Unit, SPI Supplies/Structure Probe, Inc.) and observed using a SEM instrument (JSM6010, JEOL). The SEI mode was selected and all images were taken under a voltage of 15kV.

For the mechanical test of the micropatterned matrix, the micropatterned matrices (n=5) with a strip shape of 1 × 4 cm were used to test the Young's modules and elongation at break point using Instron with 1k newton sensor (Instron calibration Laboratory).

2.2.5. Statistical Analysis

Quantitative results were presented as mean ± standard deviation (SD). The unpaired Student's t-test was used to examine the significance between two groups, and the analysis of variance (ANOVA) test was applied for multiple group comparisons. A value of $P < 0.05$ was considered statistically significant.

2.3. Results

Steps in preparing the bio-inspired 3D platform were illustrated (Fig. 1). It started from the synthesis of GelMA by chemically crosslinking gelatin with methacrylate to obtain the methacryloyl groups, the reactive group that could be conjugated to PEGDA (Fig. 1A). Afterwards, GelMA was used as the raw material in an electrospinning process to generate randomly aligned nanofibers (Fig. 1B). After the electrospinning process, the membrane-like GelMA matrix was crosslinked with carbodiimide in a solvent mixture (acetone/water = 95/05 v/v) to preserve the nanofibrous structure (Fig. 1C). In the next step, PEGDA was cast onto the surface of the crosslinked GelMA matrix (Fig. 1D), followed by a UV-induced photolithography process to create a micropatterned scaffold (Fig. 1E). The alkene groups on the PEGDA and GelMA were initiated and crosslinked together to stabilize the micropattern. Finally, a computer-aided laser ablation technology was carried out using a Leica LMD 7000 system (Fig. 1F) to create a 3D nanofibrous micropatterned tubular matrix (Fig. 1G).

The final product was a membrane-like scaffold (Fig.2A&B). According to the design of the photomask, the surface area of each scaffold was 1x1 cm^2, and the thickness varied with the crosslinking time. When the electrospun matrix was

crosslinked for 24 hours, its final thickness was about 50 μm. Moreover, crosslinking time also influenced the mechanical properties of the scaffold that with the increase in crosslinking time, the elastic modulus (Fig. 2G) and the elongation (Fig. 2H) to break-point were both significantly improved. SEM images showed the morphology of the nanofibrous micropatterns (NF-MPs) within a scaffold (Fig. 2C&D). Two distinct surface topographies were exhibited. Within the microislands, the gelatin nanofibers were clearly exposed, and the average diameter of the fibers was approximately 200-500 nm (Fig. 2E), which was the same range of collagen fibers in natural dentin ECM. While surrounding the microislands, PEGDA hydrogel penetrated and covered the interweaving GelMA nanofibers, forming a smooth and non-adherant surface.

Unlike the GelMA matrix which was extremely soft and difficult to be smoothed out even with a superfine tweezer, the NF-MP scaffold containing both GelMA and PEGDA exhibited a much stronger mechanical strength, which significantly facilitated operation. We found that the incorporation of PEGDA with the gelatin matrix greatly increased the mechanical strength from 88 ± 5 MPa to 184 ± 27 MPa (Fig. 2G), while decreased the elasticity of the electrospun matrix (Fig. 2H). The elongation at break-point of the NF-MP was more than 21%, indicating it was appropriate to be used as a cell culture substrate.

Human DPSCs were trypsinized into single cells and seeded on NF-MPs and their interactions with the nanofibrous micropatterned matrix were examined. Phalloidin-633 was used to stain the filamentous actin to show the cell morphology on the bio-inspired microislands. As shown by the time-lapse tracing of single hDPSCs on

their microislands (Fig. 3A), the cells quickly attached to the microislands after they were seeded onto the micropatterned matrix and started to spread within 2 hours (Fig. 3A). The cell area increased with culture time, and reached a plateau at 24 hours after seeding and longer culture times failed to further increase the cell spreading area (Fig. 3B).

Even though microislands could be clearly observed under a bright light microscope (Fig. 4), it was difficult to distinguish the number of cells that were accommodated within a microisland. Therefore, FITC-labelled GelMA was synthesized and mixed with regular GelMA in preparation of the electrospun matrix to make the nanofibers visible with fluorescent microscopy (Fig. 2G and Fig. 4). After the photolithography process, partial FITC molecules surrounding the microislands were quenched by the UV light and covered by PEGDA hydrogel, therefore, the nanofibers within the microislands displayed a much brighter color. High-resolution confocal images, as well as SEM images, showed that regardless of shapes of the microislands, which were precisely controlled by the design of the photomasks, hDPSCs were strictly confined by PEGDA within the microislands. Single hDPSCs spread on the nanofibers and perfectly recapitulated the morphology of their residing microislands when an appropriate spreading area was given (Figure 4), illustrating the ideal biocompatibility of underlying GelMA nanofibers and strong cell-repellent effect of surrounding PEGDA.

The stability of the NF-MPs for single cell study was examined by harvesting the scaffolds at 1, 4, 7, 14, 21 and 28 days after hDPSCs seeding, respectively. During the culture process, aphidicolin, a nuclear DNA replication inhibitor was added to the

culture medium to prevent cell proliferation. Both confocal and SEM images (Fig. 5A) showed that the boundary between GelMA nanofibers and surrounding PEGDA stayed intact and sharp at each timepoint, and cells were strictly confined within the microislands. Moreover, degradation of PEGDA surrounding the microislands was not detected and its limiting effect was well maintained. Meanwhile, hDPSCs remained alive within a microisland even 28 days after initial seeding, although the number of attached cells decreased over time as shown by the MTT result (Fig. 5B). Apart from that, a live-dead staining protocol was also used to examine the cell vitality on the NF-MPs (Fig. 5C). In this assay, the NF-MP scaffolds were roughly washed at 1 hour after initial cell seeding and there were a few cells staying on PEGDA. After 4 days, the live-dead staining result showed that cells accommodated within the microislands stayed alive while cells attached on the PEGDA surface were dead. Since the cell density became too low for the MTT assay after 7 days' culture, the biocompatibility of the microislands was reexamined by the cell occupation ratio (Fig. 5D). Calculated by N0/N1 (N0: number of microislands occupied by cells, N1: number of all microislands examined), the cell occupation ratio was high at each timepoint. One day after cell seeding, there was nearly 70% of the microislands occupied by cells. As time passed, the cell occupation ratio decreased, while there was still 36.8% of the microislands occupied by cells after 28 days. In the meantime, the single cell ratio was examined (Fig. 5E), which was calculated by N2/N0 (N0: number of microislands occupied by cells, N1: number of microislands occupied by only one cell), to satisfy our need for single cell observation. The single cell ratio was relatively low at the initial seeding (21.3%), while it increased

greatly to 46.7% after 2 weeks' culture. To be noted, the cell occupation ratio and the single cell ratio reported were calculated on circular microislands with a diameter of 40 μm, while they could be easily modulated when parameters such as the size, shape of the micropatterns or seeding times were changed.

ECM is a reservoir for various growth factors. Since GelMA preserves the functional free amino groups of collagens, it inherits the capability to be crosslinked with bioactive proteins or peptides and become functionalized. Bone morphogenetic protein 2 (BMP-2) was selected for experiments. BMP-2 proteins were grafted onto the GelMA nanofibers using a one-step process with a heterobifunctional crosslinker that contains both NHS ester and maleimide groups (Fig. 6A). To verify the successful conjugation of BMP-2 proteins on the microislands, an anti-BMP-2 antibody was used for immunofluorescent staining (IHC) (Fig. 6B). The BMP-2 molecules were strictly confined within the microislands that no BMP-2 IHC staining was observed on the surface of surrounding PEGDA (Fig. 6C). Moreover, the BMP-2 proteins were evenly distributed in the microislands and the density was about 80 ng/cm^2, which could be easily modulated by changing the reactant concentration during the crosslinking process. The cell adhesion ratios on the microislands were enhanced after the conjugation of BMP-2 onto gelatin nanofibers (Fig. 6D). To evaluate the bioactivity of the incorporated BMP-2 molecules, ALP staining assay was performed and both ALP-positive single cell ratio and relative ALP intensity were examined. Single hDPSCs cultured on the BMP-2 conjugated microislands exhibited a much higher ratio of ALP positive cells (Fig. 6E)

than the control group. Moreover, the relative ALP intensities were significantly higher than the non-conjugated group at all 3 timepoints (Fig. 6F).

Using the FITC-labelled gelatin nanofibers, the interaction between the nanofibers and hDPSCs at the molecular level could be observed directly. Vinculin, a key protein of focal adhesion complexes, was employed to evaluate the formation of focal adhesion of single hDPSCs on the GelMA nanofibers. The expression of vinculin was detected both at the edge and in the middle of the microislands (Fig. 7A), revealing a uniformly distributed interaction sites between the cell and the nanofibers. To examine whether integrin-mediated signaling pathway was involved in this interaction, anti-β1 integrin immunostaining was used to show scattered β1 integrin proteins were at the interface between the cell and the nanofibrous matrix (Fig. 7B).

Moreover, owing to their desirable mechanic strength, the micropatterned scaffolds were used for the combined cytological section technique and confocal imaging to obtain higher magnification and quality images of the cell matrix interface. The selectivity of the micropatterned scaffold was confirmed that all the cell bodies were limited within the microislands, while their intervals were occupied by PEGDA (Fig. 8 A-C). Moreover, high-resolution confocal images (Fig. 8 D-F) showed that multiple short pseudopodia extended from the cell body and inserted into the pores of the nanofibrous matrix, which was identical to the interaction between a cell and its surrounding ECM within the *in vivo* environment.

To mimic the tubular architecture of dentin ECM, a laser-drilling technique (Fig. 9A) was employed to generate a microchannel within each microisland (NF-MT) (Fig. 9

B). EDS analysis found that the surface chemistry within a microisland mostly remained unchanged after the laser-drilling process, as indicated by the element compositions of carbon, nitrogen, oxygen in the matrix (Fig. 9 C). The biocompatibility, shown as the cell occupation ratio, also confirmed this observation (Fig. 9D). The morphology of single hDPSCs changed dramatically when they were seeded on NF-MTs. Top view SEM images showed that single hDPSCs on NF-MTs exhibited a more stereoscopic sphere-like morphology (Fig. 9E) and reconstructed confocal Z-stacked images (Fig. 9F) further illustrated this morphological change. It's seen that the majority of cytosol including the nucleus remained above the microislands, displaying a hemispherical shape, meanwhile a long and thin cellular process was formed within the laser-drilled microchannels, displaying a polarized morphology identical to the *in vivo* odontoblasts (Fig. 9G). Moreover, the average diameter of the cellular processes of the single hDPSCs on NF-MTs were comparable to that of the *in vivo* odontoblasts (Fig. 9H).

2.4. Discussion

Traditional *in vitro* cell culture microenvironments were significantly different from the *in vivo* environment in many aspects, including the stiffness, surface topography, chemical components and other features. Thus the *in vivo* cellular behaviors that researchers were aiming to observe could not be convincingly recapitulated *in vitro*. Odontoblasts are a vivid example of the characteristic that they display distinct cell morphologies *in vivo* and *in vitro*, which impose a great challenge to understanding the odontoblast polarization process. Therefore, to identify the regulatory factors in this process, a biomimetic platform that enables the recapitulation of polarized odontoblast

morphology was a prerequisite. In this chapter, by combining electrospinning, chemical crosslinking, photolithography, and laser-drilling techniques, we successfully generated 3D scaffolds that managed to induce single hDPSCs to polarize into a odontoblast-like morphology.

In seeking the polarized morphology of an odontoblast *in vitro*, it's important to recapitulate the natural microenvironment. Since dentin ECM has a hierarchic structure ranging from nano to macro scales, the scaffold design needed to incorporate this into the design.

First, GelMA was selected as the raw material for the scaffold. Gelatin is denatured derivative of collagen, the main component of dentin ECM. Gelatin retained the bioactive sites including RGD and MMP-responsive sites of collagen, but eliminated the potential risk of pathogen transmission during the denaturing process, making it an ideal choice for the scaffold design [164, 165]. In addition, gelatin was transparent in aqueous solution and this property allowed monitoring cell behaviors with an optical microscope. Moreover, fluorescent dyes (FITC) could be conjugated to the gelatin nanofibers [166, 167], therefore, the fabricated micropatterns could be clearly distinguished from cells using fluorescent microscopy (Fig. 2F & Fig. 6). To use gelatin in photolithography, a further step was performed by crosslinking gelatin with methacrylic anhydride to generate GelMA. As a result, many amino groups were present on the side chains of gelatin that could be replaced by the methacryloyl groups from methacrylic anhydride, which made the material responsive in a photocrosslinking process. GelMA could self-crosslink or crosslink with other reagents with active double

bonds under UV light [168]. When the GelMA-based electrospun matrix was crosslinked with PEGDA, a stable a non-fouling background could be generated.

The large amount of free amino groups of GelMA allowed it to be readily conjugated with bioactive proteins or peptides and a Sulfo-SMCC-mediated crosslinking reaction, which enabled crosslinking in physiologic solutions [169] to achieve conjugation (Fig. 6A). BMP-2 proteins were used as an example. After electrospinning and chemical crosslinking procedures, the GelMA nanofibrous matrix was conjugated with BMP-2 proteins in a contamination-free cabinet before photolithography. This operation sequence was designed to protect BMP-2 proteins from bacterial contamination and degradation. Immunochemical staining with anti-BMP-2 antibody demonstrated that BMP-2 molecules were successfully conjugated to the nanofibers and the growth factors were evenly dispersed within the microislands (Fig. 6 B&C). The bioactivity of BMP-2 molecules was well-maintained after the photolithography process shown by elevated cell occupation ratios (Fig. 6 D) and ALP expression (Fig. 6 E&F). Moreover, compared to 2-D traditional cell culture methods, significantly less BMP-2 proteins (80ng/ cm^2) were used in microislands (Fig. 6C), and a similar effect was exhibited in promoting odonto-lineage differentiation (Fig. 6 E&F) [170, 171]. Moreover, the gelatin-based NF-MP could be conjugated with other types of bioactive factors to fulfill the needs of specific studies.

Second, the electrospinning technique was adopted to generate a 3D nanofibrous matrix, which mimicked the nanofibrous microstructure of dentin ECM (Fig. 2 D&E). Diameters of electrospun nanofibers range from less than 100nm to several micrometers

based on the selection of raw material and parameters of the electrospinning process. Compared to other approaches in fabricating nanofibrous scaffolds such as phase separation, meltblowing, self-assembly or template synthesis, electrospinning was the most mature and commonly used approach [172]. More importantly, the electrospinning technique facilitated the production of a membrane-like scaffold with controllable thickness, which enabled and greatly favored the following photolithography and laser-drilling procedures. As we have reviewed in the Introduction Chapter, although the micropatterning technique was frequently used in biomedical studies, a micropattern constructed on a nanofibrous substrate for single cell entrapment has not be achieved. In this work, a *in vivo* like platform was successfully generated, as indicated by the formation of multiple filopodia within the porous space of the matrix. In addition, the uniformly distributed vinculin (Fig. 7A) and integrin β-1 proteins (Fig. 7B) within the cytosol was proof that the cells were making active contact with the scaffold. Previous studies confirmed the formation of focal adhesions, which was linear vinculin patches at the tips of actin stress fibers at the lamellipodia margins, was easily observed on a traditional 2D culture substrate. However, cells cultured within a 3D context, the adhesion related proteins were usually absent at the cell-matrix interface, instead, they were randomly distributed within the cytosol [173]. Therefore, our combination of electrospinning and photolithography technique could enable the observation of single cell behaviors in a more *in vivo*-like microenvironment.

Third, an innovative laser-guided ablation approach was used to introduce the 3D tubular structure to the nanofibrous micropatterns (Fig. 9 A&B) and *in vitro* hDPSC

polarization was successfully achieved (Fig. 9 E-H). Compared to the traditional cutting approaches, laser beam cutting has multiple outstanding merits. This approach was computer programming-aided and contact-independent, thus it ensured that the nanofibers surrounding the microchannels and the delicate boundary between PEGDA and the nanofibrous matrix were not impaired, which were confirmed by both the EDS analysis (Fig. 9C) and the confocal imaging (Fig. 9D). More importantly, it had excellent precision and efficiency, so the ablation and penetration into the nanofibrous matrix was easily achieved and channels with micrometer sizes were successfully generated. In our preliminary studies, we found that the diameter and distribution density of the artificial microchannels could be precisely controlled by modulating the laser power, laser writing speed and pulse frequency. Specifically, the laser power was used to control the size and the depth of the tubular pores, and the laser writing speed and laser pulse frequency were used to adjust the distance between the microchannels. Small microchannels (<10 μm) were generated with lower laser power, and narrow spaces between the microchannels were obtained from high pulse frequencies and low writing speed. Using a high laser frequency or a low writing speed led to the microchannels were interconnected and formed micro-grooves. Because the laser ablation approach was precisely modulated by a computer program, the depth of the microchannels could be readily controlled by the repetition of the laser ablation process. In addition, the orientation of the microchannels to the matrix could also be conveniently adjusted via changing the angle between the laser plane and the matrix plane (data not shown).

This scaffold design not only simulated natural dentin but also displayed several other advantages that would benefit our odontoblast studies.

One of the most characteristic features of our scaffold was the micropatterning design. The design allowed the observation of single cell behaviors in response to a stimulus without interference from intercellular communications. Another advantage of the design was that cells usually don't polarize spontaneously on a tubular surface. We found that a very small ratio of dental cells could project cytoplasmic process into the microchannels and form a polarized morphology when cultured on a non-patterned scaffold even with a high seeding density (5×10^6/ml). This phenomenon was consistent with previous studies that used pulp tissue [174] or a cell pellet [138], odontoblast-like polarization was observed in a many cells on the tubular surface. Therefore, using a relatively small micropattern could further impose a physical compacting effect to the entrapped cell. We found that cells cultured on the non-tubular microisland displayed a hemispherical morphology (Fig. 8F), which was significantly different from cells cultured on a non-patterned nanofibrous surface.

Another advantage of this design was it possessed desirable mechanical strength (Fig. 2 G&H). Stiffer and stronger than the GelMA matrix, the micropatterned scaffolds greatly facilitated handling and operation. However, they were softer than glass or silicon, therefore, the laser-drilling process for microchannel generation and the scaffold sectioning for lateral observation (Fig. 8) became possible. This feature was indispensable for our following odontoblast polarization study since it enabled hDPSC

polarization and offered great convenience to observe the formation of cellular processes.

This NF-MP scaffold also exhibited great stability. Both confocal and SEM images confirmed the hDPSCs remained confined within the microislands even 4 weeks after seeding (Fig. 5). Moreover, the boundary between PEGDA and the nanofibrous matrix stayed intact and sharp, indicating that this platform could potently resist hydrolysis and enzymolysis. Therefore, this desirable stability enabled the study for long-term cell experiments, for example, cell differentiation studies, which were difficult for previous micropattern designed platforms because the non-fouling surface could not be maintained for more than 7 days [144].

In conclusion, by combining the electrospinning, chemical crosslinking, photolithography and laser ablation techniques, a 3D biomimetic micropatterning scaffold was generated, which successfully induced single hDPSCs to polarize *in vitro*. Moreover, as a platform for *in vitro* single cell observation, it could provide tremendously useful matrix for future odontoblast studies.

3. IDENTIFICATION OF BIOPHYSICAL FACTORS THAT REGULATE SINGLE HDPSC POLARIZATION AND DIFFERENTIATION

3.1. Introduction

It has been well documented that biophysical properties of a scaffold have profound effects on stem cell fates. The surface topography [175-177], stiffness [178, 179], porosity [180], and many other physical features [181] of a scaffold can regulate cell behaviors in various ways. In chapter 2, we described the development and characterization of the nanofibrous matrix-based micropatterning technique for single-cell observation *in vitro* and identified the advantages over traditional 2D cell culture approaches. Moreover, this micropatterning design possessed ideal feasibility that many parameters of the scaffold could be modulated during the fabrication process. In this chapter, we aimed to test the hypothesis that changing several biophysical factors in the micropatterning design could influence polarization and differentiation behaviors of single hDPSCs.

3.1.1. Micropattern morphology

Numerous *in vitro* studies have demonstrated that the cell morphology was closely related to cell differentiation behaviors. Researchers have managed to modulate cell differentiation orientations by directly manipulating cell morphologies with various bioengineering approaches. For example, cells cultured on a nanofibrous scaffold were forced to display an osteocyte-like morphology with dendrites formed within the micropores of the scaffold, which led to an increased osteogenesis [182]. The

development of the micropatterning technique has offered a more straightforward approach to control cell morphology and explore the relationships between cell morphology and differentiation. With this technique, it was demonstrated that MSCs could switch between osteogenic and adipogenic differentiation depending on the micropatterns [147, 183, 184]. Moreover, various parameters of the micropattern morphology were proved to participate in the modulation effect, including the adhesion area [185], shape [147, 183], aspect ratio [163], subcellular curvature [184] and depth [186]. However, similar studies relevant to dental cells had not been reported, thus how micropattern morphology influenced odontogenic differentiation and polarization remained unclarified. Since we had developed a biomimetic micropatterned scaffold, it's important to examine whether the differentiation and polarization behaviors of single hDPSCs would be influenced when they were cultured on an ECM-like substrate and limited within a predefined morphology.

3.1.2. Surface topography

Nanofibrous architecture of natural ECM has been accepted to have regulatory roles in a variety of cellular behaviors [164, 187-189]. By mimicking this natural nanofibrous structure, researchers have been attempting to recapitulate the physiological morphology and behaviors of *in vivo* cells [164, 190, 191]. For example, bone marrow stromal cells (BMSCs) have been the subject of multiple studies that proved the nanofibrous architecture promoted an *in vivo*-like cell morphology and enhanced BMSC adhesion [192], motility [164], proliferation [175], osteogenic and chondrogenic differentiation [191, 193]. However, although they were designed to focus on cell-matrix

interaction, none of the studies could exclude cell-cell interactions, which contribute to almost all cytological behaviors. Consequently, the outcomes presented to researchers were the combined effects of cell- nanofiber interactions and cell-cell interactions. To date, how a single stem cell interacts with nanofibers and its underlying mechanism remained largely ambiguous. Therefore, our micropatterned scaffold could be applied as a powerful tool to observe how a single cell interacts with the nanofibrous topography at sub-cellular scales with the deprivation of intercellular communications.

3.1.3. Three-dimensional tubular architecture

Apart from 2D physical parameters, 3D spatial architecture was also critical within the microenvironment of a cell. Nature dentin possesses a unique tubular architecture that coordinates with the morphology of odontoblasts. In primary dentin formation, the polarization and retreat of odontoblasts were the main factors that ensured the formation of tubular dentin. However, in dentin reparation or regeneration work, the neo-formed dentin often exhibited bone-like features with the matrix-secreting cells embedded inside. To date, only under specific circumstances could researchers observe tubular dentin formation [194]. For example, researchers that seeded DPSCs on the surface of natural tubular dentin observed cell polarization behaviors. These cells extended cytoplasmic processes into the existing dentinal tubules and moreover, deposited matrix and formed new tubular dentin continuous with the existing dentin [140, 143]. In addition, dental cells cultured on a Millipore filters displayed a similar polarized morphology with cytoplasmic processes extending into the filter space and formed tubular dentin-like mineralized tissues [138]. An artificial scaffold designed with

dentinal tubule-mimicking microchannels also promoted the layer of dental cells adjacent the microchannels to form cellular processes within the microchannels and deposit matrix around the processes. When this scaffold was implanted *in vivo*, tubular dentin-like mineralized tissues could be formed at the microchannel area and the newly formed dentinal tubules were continuous with the microchannels. However, on a non-tubular scaffold, neither odontoblast polarization nor tubular dentin formation was achieved [174]. These previous studies had powerfully indicated that the tubular structure was a vital factor to initiate dental cell polarization *in vitro* and promote tubular dentin formation, even though the underlying mechanism remained unclear. With our versatile nanofibrous micropatterning technique, it was possible to figure out how this 3D spatial architecture regulated odontoblast polarization and differentiation at the single cell level.

3.1.4. Gravity

Gravitational force is a biophysical factor that exist continuously during development. Cells cultured on a gravity-modified microenvironments displayed altered cell behaviors in many aspects [195], including stem cell proliferation and differentiation. For example, microgravity cultures were proposed for in cell-based therapies for CNS diseases to enhance the therapeutic effect of stem cell transplantation [196, 197] for inducing MSC neural-lineage differentiation [198]. As to odonto/osteo-lineage differentiation, microgravity was reported to suppress the osteogenic differentiation of human osteoblasts [199], human MSCs [200], and mouse embryonic stem cells [201], while hypergravity induced rat MSCs to differentiate into force-

sensitive osteoblasts [202]. In 2 additional studies, hDPSCs were cultured on a 3D PLGA scaffold and exposed to a rotatory vessel to create a microgravity microenvironment. Increased cell proliferation and cell adhesion were observed [203] and moreover, when the cell-scaffold complex was implanted *in vivo*, the cells exhibited obviously accelerated odontogenic differentiation behaviors by increased expression of odontogenic related markers [204]. However, to date, there have not been studies focused on the effect of gravity on odontoblast polarization.

Therefore, in this chapter we aimed to generate 1) NF-MPs of various sizes and shapes to demonstrate the influence of micropattern morphology; 2) nanofibrous gelatin micropatterns (NF-MPs) and flat film gelatin micropatterns (FF-MPs) to explore the influence of surface topography; 3) 3D tubular micropatterns (NF-MTs) to examine the influence of the spatial architecture, and 4) spatially rotated microenvironment to check the influence of gravity. HDPSC polarization would be examined by observing the formation of cell process and the location of Golgi, while hDPSC differentiation would be examined with ALP staining.

3.2. Materials and Methods

3.2.1. Micropattern fabrication

To generate flat film micropatterns, GelMA aqueous solution (0.2% wt/v) was prepared by dissolving 1.0 mg of GelMA in 50 ml of deionized water at 40°C. An ImmEdge™ Hydrophobic Barrier Pen (Vector Laboratories, H-4000) was used to define a 1.5 cm × 1.5 cm square frame on glass slides. Twenty microliters of the GelMA solution was uniformly dripped into the pre-defined area and allowed to dry at room

temperature for 4 hours. The slides were then incubated at 4°C for 30 minutes to ensure GelMA gelation. Next, 150 µl of crosslinking aqueous solution containing 2.5 mM MES, 3 mM EDC, and 0.5 mM NHS was dripped onto the GelMA gel to crosslink the GelMA at 4°C for 12 hours. The GelMA slides were then immersed in 50 mM glycine aqueous solution for 1 hour at room temperature to neutralize the unreacted EDC and washed with deionized water for 3 times (15 minutes each). Air-dried samples were then ready for photolithography, which followed the same procedure as the nanofibrous micropatterns.

To generate 3D tubular micropatterns, the parameters of the laser beam was set following the description on the NF-MPs. A Leica Microdissection machine (LMD 6000) was used. The Laser Screw mode was selected, and a 5 μm^2 circle was drawn within each micropattern on the software screen to mark where the laser would target and drill. The power of the laser beam was set as 20, aperture as 16, speed as 15, specimen balance as 15, pulse frequency as 228, offset as 101, step size as 2 and repeats as 10.

3.2.2. Cell culture

HDPSCs seeding on NF-MPs and FF-MPs were performed as described in chapter 2.2.2. HDPSCs were cultured in an ascorbic acid-free α-modified essential medium (a-MEM) (GIBCO, Invitrogen, Carlsbad, CA, A1049001) supplemented with 10% (v/v) FBS (Gibco, #26140079) and 1% penicillin/streptomycin (Sigma, #P333) and maintained in a humidified incubator with 5% CO_2 at 37 °C. NF-MTs were sterilized with 75% alcohol for 30 minutes and then washed with PBS 3 times (5 minutes each).

HDPSCs of passage 3-8 were trypsinized and isolated into single cells with a density of 5×10^5/ml. Then 200μl cell suspension was dripped onto each NF-MT. NF-MTs were returned to incubator to allow cell attachment for 50 minutes before they were gently washed with cell culture medium to remove the unattached cells. For the ROCK inhibition assay, 2 μM Y-27632 (Calbiochem, #688000) was added to the culture medium 4 hours after cell seeding. For hDPSC differentiation, 1 mM dexamethasone, 50 mM ascorbic acid-2-phosphate, and 10 mM β-glycerophosphate were added to the medium 24 hours after cell seeding. Cell culture medium was changed every 3 days.

To examine the effect of gravity on hDPSC polarization and differentiation behaviors, NF-MT samples were seeded with hDPSCs (5×10^5/ml). After washed with fresh medium to remove unattached cells, NF-MT samples were rotated either 90^o or 180^o vertically in 48-well plates to create a decreased gravity microenvironment. The maintenance of the vertical rotation of NF-MT samples was provided by a 3D-printed highly-porous ring made from hydroxyapatite and polycaprolactone. After cells were cultured for 72 hours, 90^o or 180^o rotated NF-MT samples were harvested and fixed with 4% PFA.

To trace the formation of cellular processes within the NF-MTs, 5 timepoints were selected (12, 24, 48, 72 and 96 hours) scaffolds were harvested and fixed with 4% PFA for staining with CF633 phalloidin and Hoechst 33342. Some specimens were processed for cryosections to obtain lateral images. Lateral images from single hDPSCs were acquired and analyzed with Image ProPlus 7 to measure the ratio of hDPSC with process (the percentage number of single hDPSCs that displayed a cellular process

within the laser-drilled microchannels), together with the lengths and diameters (the diameters at the half lengths) of the processes.

3.2.3. Immunofluorescence Staining

Samples were fixed, permeated, blocked, and stained following the same procedures as described in chapter 2.2.3. Primary antibodies used in these experiments included anti-YAP1 antibody (1:500, Abcam, ab39361), anti-Runx2 antibody (1:150, Abcam, ab23981), anti-β tubulin antibody (1:400 Abcam ab52901), anti-vimentin antibody (1:400, Abcam, ab92547), anti-GRASP65 antibody (1:200, Invitrogen PA3-910), and anti-Collagen I antibody (1:50, Abcam, ab216892). Second antibodies were Alexa Fluor Plus 555 secondary antibodies (1:200, Invitrogen, A32732) supplemented with 1% goat serum (1:200, Invitrogen, A32732).

For mitochondria adenovirus transfection, Ad-Mito-DsRed (SignaGen Laboratories #SL100744) was a kind gift from Dr. Jerry Feng, Texas A&M University, College of Dentistry. After hDPSCs were seeded and stablished on NF-MTs, culture medium containing 5×10^5 PFU/ml Ad-Mito-DsRed were added to replace the normal medium 12 hours before NF-MT samples were harvested.

3.2.4. Statistical analysis

Apart from cell attachment ratio and single cell ratio analysis, only micropatterns occupied with one single cell were selected and analyzed in all experiments in these experiments. Semi-quantitative data from all images were analyzed with the ImageJ software, including cell area, circularity index, aspect ratio and ALP density. For quantitative analysis, six regions of interest and at least 30 cells were selected for each

group. All experiments were repeated twice. Data were analyzed with t-test, and statistical significance was set at $p < 0.05$.

3.3. Results

3.3.1. Micropattern morphology

Micropatterns of various sizes and shapes were fabricated by using photomasks with different morphological designs (Fig. 10). As shown by the SEM images, each NF-MP microisland perfectly recapitulated the morphology of the photomask applied to it and the nanofibrous GelMA nanofibers were separated from the smooth PEGDA surface regardless of size or shape. HDPSC attachment and cell morphologies were examined on various micropatterns, respectively. By staining patterns and calculating the cell occupation ratios, high cell occupation ratios were obtained on each NF-MP scaffold (Fig. 11A). Moreover, single hDPSCs fully occupied the microisland regardless of the size and shape of the microisland (Fig.11B).

To explore the influence of surface area to single hDPSC behaviors, quadrate micropatterns of different surface areas (625, 1600 and 3600 μm^2) were generated and seeded with cells and the cell occupation ratio and single cell ratio on each NF-MP scaffold were examined. A relatively low seeding density (1×10^5 /ml) was used to show the difference among groups. There was a positive correlation between the cell occupation ratio and the micropattern size as 29.1% of the 625 μm^2 microislands, 35.1% of the 1600 μm^2 microislands and 68.6% of the 3600 μm^2 microislands were occupied by the hDPSCs, respectively and significant differences were found among groups (Fig. 12A). A negative correlation between the single cell ratio and the size of the microisland

was found since the single cell ratios on the 625 μm^2, 1600 μm^2 and 3600 μm^2 microislands were 26.8%, 54.2% and 75.9%, respectively, with significant differences among groups (Fig. 12B). The effect of microisland shape on hDPSC attachment was explored by fabricating microislands of same surface area (1600 μm^2) but different shapes (quadrate, hexagonal, circular and triangular). There was no significant difference in cell occupation ratio (Fig. 12C) or single cell ratio (Fig. 12D) among the 4 groups.

Single hDPSC morphology was examined on various microislands via both SEM and confocal z-stacking laser scanning microscopes. SEM images of the apical views of single hDPSC morphologies on circular microislands of different surface areas (625, 1600 and 3600 μm^2) (Fig. 13A) while the 3D images from the confocal z-stack demonstrated the cross sectional profile (Fig. 13B). Single hDPSCs were less spread and displayed a hemispherical morphology with a higher cell height when the microisland was 900 μm^2. On the contrary, a hDPSC on large microislands were much flatter and the height was significantly shorter.

The effect of microisland shape and size on single hDPSC differentiation were examined via ALP staining assay. Circular microislands of different surface areas (900 μm^2, 1800 μm^2 and 3600 μm^2) were generated and seeded with hDPSCs for 3 days (Fig. 14A). There was 9.1% single hDPSCs on the 900 μm^2 NF-MPs, 12.9% single cells on the 1800 μm^2 NF-MPs and 19.2% single cells on the 3600 μm^2 NF-MPs positive for ALP staining (Fig. 14B). Moreover, the relative ALP intensity on the 3600 μm^2 NF-MPs was significantly higher than the 900 μm^2 group and the 1800 μm^2 group (Fig. 14C). Microislands of the same surface area (900 μm^2) but different shapes (quadrate,

hexagonal, circular and triangular) were generated and single hDPSC differentiation on them were examined (Fig. 14D). ALP positive cell ratios were similarly high on the hexagonal (12.4%) and cubic (11.2%) NF-MPs, slightly lower on the circular (9.7%) NF-MPs and lowest on the triangular NF-MPs (5.3%), which was significantly different from the other shapes (Fig. 14E). The relative ALP staining intensity confirmed the result that the ALP intensities were significantly lower on the triangular group while the other 3 groups were similar (Fig. 14F).

To examine the polarization behaviors of single hDPSCs on microislands, apart from the previously mentioned isotropic micropattern designs, rectangular microislands with different aspect ratios (2:1, 4:1 and 8:1) were also introduced to eliminate the surface isotropy. Cellular process formation was examined on NF-MP scaffolds with various sizes and shapes. We found that cells seeded on microislands of small surface areas (900 and 1800 μm^2) appeared to occupy the whole microisland without distinguishable cellular processes. However when microislands with a large surface area (3600 μm^2) were utilized, some cells did occupy part of the micropatterned surface and some had dendrite-like processes. However, a specific pattern was not found in the analysis of the processes orientation. Another approach employed to examine hDPSC polarization was labeling and locating the Golgi apparatus. In most cells, the Golgi apparatus was randomly distributed (Fig. 14E). To determine the distribution pattern of the Golgi apparatus, a simple coordinate system was established to quantify the position of Golgi apparatus. The center of the nucleus was artificially defined as the “origin” and the line passing the longitudinal axis of the micropattern was defined as the “X axis” and

the line perpendicular to it was defined as the "Y axis". The center of each Golgi apparatus was located by its ordered pair in the Coordinate. As the scatter plot demonstrated (Fig. 14H), no pattern in Golgi locations was detected.

3.3.2. Surface topography*

To explore the influence of surface topography on hDPSC polarization and differentiation, GelMA-based microislands with a flat surface was fabricated using a gelatin coating technique. Briefly, GelMA aqueous solution was dripped on a glass side, which allowed the solution to freely spread and form a flat film. After chemical crosslinking, the flat film could be employed as a substrate for photolithography. Micropatterns were successfully generated on these 2 distinct substrate surfaces that were referred to as nanofibrous micropatterns (NF-MPs) and flat film micropatterns (FF-MPs) (Fig. 15A-C and Fig. 15 F-H). After hDPSCs were seeded onto the two micropatterned matrices, cell adhesion behaviors were examined. Both SEM images (Fig. 15 D&I) and confocal images (Fig. 15 E&J) confirmed the cell confining effects of both types of micropatterns. In preliminary studies, we had found that the average spreading area of a hDPSC on a petri dish after 24 hours' culture was 2398 ± 765 μm^2. To exclude the cell size effect, a micropatterning design with a surface area of 3600 μm^2 was selected for this part of the experiments. Under this condition, the cell occupation ratios were 75.1% on a NF-MP scaffold and 81% on a FF-MP scaffold (Fig. 15K), and

* Modified with permission from "Nanofibers Regulate Single Bone Marrow Stem Cell Osteogenesis via FAK/RhoA/YAP1 Pathway" by Bei Chang, Chi Ma, Xiaohua Liu, 2018. ACS applied materials & interfaces, 10, 33022-33031, Copyright 2018 by American Chemical Society.

the single ratios on those scaffolds were 45.4% and 37.9% (Fig. 15L), respectively, with no differences found between the two groups. Again, only micropatterns occupied by single cells were used in this study.

It was evident that the morphologies of single hDPSCs on NF-MPs and FF-MPs were different. On the NF-MPs, hDPSCs exhibited a narrow, irregular shape with multiple cellular processes extending towards the margin of the micropattern (Fig. 15 D&E). In contrast, cells on FF-MPs had a flattened, spread shape without any obvious cellular processes formed (Fig. 15 I&J). Moreover, the spread area of single hDPSCs on the NF-MPs was significantly smaller than that on the FF-MPs (Fig. 15M). Twenty-four hours after cell seeding, the hDPSCs on the NF-MPs had a stable adhesion area of 1709 μm^2, while the adhesion area on FF-MPs was 2296 μm^2. To quantify the different cell morphology on NF-MPs and FF-MPs, two descriptive indexes were used. The circularity index ($CI = 4\pi A/L2$) represents the circularity of a cell, where A is the area of the cell, and L is the perimeter of the cell, with CI=1 representing a perfect circle. The aspect ratio (AR) is calculated as a ratio of the major cell axis length to the minor cell axis length, which represents the symmetry of a cell, with AR=1 indicating an absolute symmetry. Results showed that single hDPSCs on the NF-MPs had a smaller CI value (0.3 vs 0.65) (Fig. 15N) and a larger AR value (1.84 vs 1.13) (Fig. 15O) compared to those on the FF-MPs.

The confocal images of actin microfilaments were also quite different on the NF-MPs and FF-MPs (Fig. 15 E&J). Most of the actin microfilaments within a cell on the FF-MPs formed well-organized stress fibers, and the actin cortex under plasma

membrane was not obvious (Fig. 15J). In contrast, the stress fibers within a cell on the NF-MPs were scarce, and most actin filaments formed actin cortex underlying the plasma membrane (Fig. 15E). Quantitative analysis further demonstrated that single hDPSCs on the NF-MPs had fewer organized stress fibers compared to cells on the FF-MPs that the average stress fiber intensity within a single hDPSC on the FF-MPs (765.7) was eight times higher than that on the NF-MPs (94.1) (Fig. 15P).

The formation and maturation of focal adhesions on the NF-MP and FF-MP were also distinct. Vinculin IHC staining was used to show the distribution of focal adhesions (Fig. 16A). Typical focal adhesions on the FF-MP matrix, indicated by linear vinculin patches, were at the tips of stress fibers in lamellipodia. However, similar linear vinculin patches were rarely seen on the NF-MP matrix, and the most of the vinculin accumulated into clusters at attachment sites and with the cortical actin. Semi-quantitative analyses showed that the focal adhesion number (Fig. 16B) and focal adhesion area (Fig. 16C) on the NF-MPs were less than 1/11, and 1/14 to those on the FF-MPs, respectively.

To determine if the substrate influence differentiation into the osteoblast lineage, ALP was assessed. After cells were cultured in differentiation medium for 3 and 7 days, a stronger ALP staining of single hDPSCs was detected on the NF-MPs than on the FF-MPs (Fig. 17A). At three days, 19.8% of the single cells on the NF-MPs were positive for the ALP staining, while that number was 15.9% on the FF-MPs (Fig. 17B). Moreover, the relative ALP activity of the hDPSCs on the NF-MPs was significantly higher than that on the FF-MPs (Fig. 17C). After culturing cells for 7 days, the ALP

positive ratio and relative activity on the NF-MPs were still significantly higher than those on the FF-MPs (Fig. 17 B&C).

To determine if the RhoGTP pathway was involved in actin reorganization an inhibitor of ROCK, Y-27632 was added to the culture medium. The Rho-ROCK pathway modulated the organization and distribution of actin reorganization including stress fibers. The size of cells cultured in the presence of Y-27632 decreased significantly on the NF-MPs and FF-MPs (Fig. 18B). In contrast to the cell area, the morphology, attachment ratio, and single cell ratio remained unchanged on both substrates in the presence of Y-27632. However, the inhibition of the RhoA/ROCK signal pathway significantly impaired the odonto-lineage differentiation of single hDPSCs (Fig. 18 C&D). The ALP-positive ratio decreased from 19.1% to 12.8% in cells cultured on the NF-MPs and from 15.8% to 13.2% on the FF-MPs (Fig. 18C). In addition, the relative ALP activity in cells on the NF-MPs and FF-MPs were reduced from 75.9 to 56.7, and from 53.6 to 21.0, respectively (Fig. 18D).

To explore the possible mechanism that lead to the distinct cellular behaviors on NF-MPs and FF-MPs, we examined the expression pattern of another protein, YAP1 (Fig. 19A). YAP1 was expressed in the cytoplasm and nucleus and the distribution pattern disclosed cellular tension [205-207]. We examined the YAP1 distribution within single hDPSCs and found that nuclear YAP1 expression was 46% of the total YAP1 expression on the NF-MPs, but 62% of the total in cells on the FF-MPs (Fig. 19B). The addition of ROCK inhibitor Y-27632 decreased the nuclear YAP1 expression in both groups, especially in the FF-MP group, although the total cellular YAP1 content did not

change significantly (Fig. 19C). We also examined the expression of Runx2 in single hDPSCs (Fig. 20A) and found that Runx2 was expressed in the nucleus of single hDPSCs in both groups, but the expression level on the NF-MPs was higher than in cells cultured on the FF-MPs (Fig. 20B). When the ROCK activity was inhibited with Y-27632, Runx2 expression was decreased on both groups. Runx2 was nearly absent in cells cultured on the FF-MPs, but still observed in the nucleus and cytoplasm of cells cultured on the NF-MPs (Fig. 20B).

3.3.3. Three-dimensional tubular architecture

In chapter 2, a 3D tubular structure was introduced into the NF-MP microislands with a laser-guided ablation technique (see 2.2.1). We found that by modulating the laser power, laser writing speed, pulse frequency and repetition times, we were able to control the diameter and depth of the microchannels. Specifically, for odontoblast studies, microchannels with a diameter of 4.56 ± 0.79 μm were generated. Moreover, a photomask covering circular shades with a diameter of 25 μm was selected to generate micropatterns with small surface areas to ensure a relatively high single cell ratio and a more *in vivo*-like cell morphology. In this study, 1 microchannel was generated within each micropattern circle to allow the formation of 1 cellular process from each isolated cell.

To examine the effect of this tubular structure on cell morphology, hDPSCs were seeded on both NF-MPs and NF-MTs. The biocompatibility, shown as the cell occupation ratio (Fig. 21E), and the single cell ratio did not change significantly after the laser-drilling process (Fig. 21J). Apical SEM images of single hDPSCs on NF-MTs had

a more stereoscopic sphere-like morphology (Fig. 21G) compared to cells cultured on NF-MPs, which had a flatter and spread morphology (Fig. 21B). This difference in cell morphology was further illustrated by lateral view images (Fig. 21 C&H) and the confocal z-stack 3D images (Fig. 21 D&I). Single hDPSCs limited within a NF-MP exhibited a 2D morphology even though tiny filopodia were seen projecting from the cells and penetrating into the gelatin nanofiber network (Fig. 21D). On the contrary, single hDPSCs on the NF-MT had a single long cellular process in the laser-drilled microchannels, while the cell body with the nucleus remained apical to the microchannel with a hemispherical morphology. This morphology was similar to *in vivo* odontoblasts (Fig. 21 H&I).

To explore the adhesion behaviors of single hDPSC on this 3D tubular culture system, focal adhesion markers β_1 integrin (Fig. 22A) and vinculin (Fig. 22B) were used. High resolution confocal images in lateral views demonstrated that single hDPSCs had fairly weak expression of β_1 integrin and vinculin, especially at the interface of the cell membrane and nanofibers where immunofluorescent signals were difficult to detect. However, mini-branches were also seen extending from the process trunk and were attached (?) inside the porous space of the electrospinning matrix (Fig. 22A), similar to the natural odontoblast. Immunostainings targeting 3 cytoskeletal elements were performed to further check the components of the hDPSC processes within the microchannels. Tubulin staining microtubules (Fig. 22C) and intermediate filaments (Fig. 22D) were found lining the cell cortex throughout the entire extended cell process.

However, the mini-branches extending from the cell process were only positive for actin staining (ADD ARROWS), while β-tubulin and vimentin signals were not be detected.

To further explore the polarization process, multiple timepoints were selected and NF-MT samples seeded with hDPSCs were harvested and sectioned at each timepoint to observe the morphological change. Typical cellular morphology at 12, 24, 48, 72 and 96 hours after initial seeding were obtained (Fig. 23A). After 12 hours, the pseudopodia from a single hDPSC interacted with surrounding nanofibers started to extend into the laser-drilled microchannels. The cell process kept moving into the microchannel until it reached a plateau at 72 hours. The culture time was extended to 96 hours but the process did not increase in length. However, multiple mini-branches formed with the lengthening of the hDPSC processe, which were observed in the lateral views (Fig. 23A add arrows to the images). The stabilized status of a hDPSC on the NF-MTs successfully recapitulated the polarized morphology of an odontoblast *in vivo*. Moreover, the ratio of single hDPSCs with process (Fig. 23B) and the length of the processes within the microchannels (Fig. 23C) were analyzed at each timepoint, which were utilized to indicate the polarization status of cells cultured on the NF-MTs.

Another marker for polarization is the position of the Golgi apparatus. The relative location of the Golgi apparatus at different timepoints was recorded using immunofluorescence staining against the unique protein GRASP65 (Fig. 24A). Twelve hours after seeding the cells, when the cellular process was initiated, the Golgi apparatus was adjacent to the nucleus, indicating a non-polarized status. The Golgi apparatus gradually moved around the nucleus towards the base of the cellular process. By the 72

hour time point, the Golgi apparatus was between the nucleus and the cellular process, indicating the cells had obtained polarized status on the NF-MT. A simplified coordinate system was used to illustrate the movement of Golgi apparatus at selected timepoints (Fig. 24B). The center of the nucleus was defined as the "origin", the "Y axis" was defined to the line passing through both the "origin" and the cellular process tip. The direction towards the process tip was defined as positive. The relative location of each Golgi apparatus to the nucleus was reflected by the value on the "Y axis". We found that the Golgi was located at a slightly negative juxtanuclear region initially (-1.9 μm after 12 hours' culture), then moved towards the positive pole, bypassed the nucleus, and subsequently moved to a positive location between the nucleus and the cellular process (7.8 μm after 72 hours' culture) (Fig. 24C).

To examine the physiological function of the cellular process within single hDPSCs on NF-MT microislands, we used adenovirus transfection to locate the mitochondria at different timepoints (Fig. 25A). We found that at the beginning of hDPSC polarization, the mitochondria were mainly accumulated in the perinuclear region. As the process extended, some mitochondria migrated towards the process. After 24 hours, a few mitochondria were at the tip of the process, which predicated a higher metabolic activity in the cell process. The expression of type I collagen was also examined using immunofluorescent staining (Fig. 25B). Type I collagen was observed not only in the main cell body above the laser-drilled microchannels, but also within the gelatin nanofibers surrounding the hDPSC process. Moreover, ALP staining was again performed to examine the effect of this tubular architecture to single hDPSC

differentiation (Fig. 25C). After cultured in odontogenesis medium for 3 days, the ALP-positive single cell ratio on NF-MT (13.9%) was significantly higher than cells grown on NF-MP (9.6%).

3.3.4. Gravity

To explore the influence of gravity in inducing odontoblast polarization and differentiation on our novel 3D platform, we manually altered the microenvironment of the culture system. By vertically rotating the NF-MT samples for 90^{o} or 180 ^{o}, we exposed single hDPSCs to a microenvironment where the direction of cellular process growth was vertical or opposite to gravity (Fig. 26A). The ratio of single hDPSC with cellular process decreased significantly, but some single hDPSCs formed cellular processes inside the laser-drilled microchannels cultured at 90^{o} (79.1%) or 180^{o} (66.67%) rotated (Fig. 26B). The processes were shorter when rotated for 90^{o} (17.9 μm) or 180^{o} (14.6 μm) compared to the control culture microenvironment (25.6 μm) (Fig. 26C). We also examined the location of Golgi apparatus in the altered orientation and found that the translocation of Golgi was slower in the 2 rotated experimental groups and stopped at a less positive position (Fig. 26D).

The effect of gravity on hDPSC differentiation was examined with ALP staining. Fewer hDPSCs were positive for ALP staining in both rotated experimental groups. Compared to the control group with ALP-positive ratio of 14.8%, 90^{o} had12.1% and 180^{o} had 10.8% cells ALP-positive, but there were no significant differences among the 3 groups (Fig. 26E).

3.4. Discussion

3.4.1. Micropattern morphology

The fate of a stem cell is regulated by various cues within its microenvironment. Even though a nanofibers-based micropatterning technique wasn't available for single cell studies before, previous studies using micropatterns constructed on flat substrate had hinted us with some critical biophysical factors that regulated stem cell behaviors, and micropattern morphology was undoubtedly one of them.

In this chapter, we firstly examined the adhesion behaviors of single hDPSCs on NF-MPs of different shape and sizes. Results showed that the cell occupation and ratio and single cell ratio were directly related to the surface area of the micropatterns (Fig. 12 A&B), while the morphology of micropatterns was not a influencing factor (Fig. 12 C&D). Moreover, the surface area also determined the morphology of the accommodated cells (Fig. 13 A&B). When the surface area was relatively small, single hDPSCs attached above displayed a hemispherical morphology with a considerable cell height, while on a relatively large micropattern, single hDPSCs were more spreading and their height were lower (Fig. 13B). Moreover, even on a large micropattern which possessed a surface area (3600 μm^2) larger than the freely spreading area of a cell, an obvious cell height could still be observed and cellular extensions could be seen within the porous space of the nanofibrous substrate (Fig. 13B). Therefore, compared to the traditional 2D cell culture surface, this nanofibers-based micropattern could better recapitulate the *in vivo* cell morphology.

Next, we examined the differentiation of single hDPSCs on the NF-MPs with different shapes and sizes and a ALP staining technique was selected due to multiple reasons. First, it's a widely accepted method that enables the identification of differentiated osteo/odontogenic cells and it allows for both qualitative and quantitative analyses. Besides, this technique examines the differentiation behaviors at early timepoints. According to our preliminary data, a 3-day period was long enough to compare the difference among groups, which not only shortened the experimental period for each trial, but also prevented cell proliferation within one NF-MP microisland and ensured the limitation effect of the PEGDA boundaries during the culture period. Moreover, ALP staining is convenient, low-cost and less skill-sensitive than many other methods like the immunofluorescence staining, which allows repetitive trails in a systemic study. Our results indicated that a large surface area led to a higher number of ALP-positive single cells and higher ALP activities than a small surface area (Fig. 14 B&C). In the meantime, the ALP activities on NF-MPs of different shapes were also examined and results showed that no significant differences were found among the circular, quadrate and hexagonal groups while they were significantly higher than the triangular group (Fig. 14 E&F).

According to previous micropattern studies, cell tension was generally believed as the main factor that linked cell spreading area to cell differentiation behaviors. When a cell was cultured on a stiff surface or within a large spreading area, signals from the microenvironment would be sensed by cell membrane receptor integrins and transduced to and activated small GTPases, especially RhoA. RhoA is the main regulator of

cytoskeleton distribution and cell tension, and by interacting with its downstream ROCK, increased RhoA activity could enhance osteogenesis [184, 208]. Therefore, the formation of stress fibers within the cytosol, which was regulated by RhoA-ROCK-myosin pathway, could be visualized as an indicator of high cellular tension. Although in this part we didn't quantify the stress fiber content within each micropattern, it could be seen from the confocal images (Fig. 11B and Fig. 13B) that the actin distribution within the cytosol were different among groups. Take the circular shapes for example (Fig. 11B and Fig. 13B), when single hDPSCs were cultured on a small micropattern, the majority of actin signals were seen accumulating under the cell cortex, while few signals could be found in the center of a cell. On the contrary, when single hDPSCs were cultured on a large micropattern, a large part of actin signals could be clearly seen in the cell center and they even formed stress fibers within the cytosol. Therefore, this distinct actin distribution pattern might be the reason leading to the different differentiation behaviors when single hDPSCs were cultured on NF-MP of different morphologies.

As to the relationship between cell shape and cell differentiation, there was no conclusive reports up to now. When the differentiation behaviors of single cells with same spreading area but different shapes were compared, opposite results had been reported [163, 183], but it's generally believed that cellular tension was still the leading causative factor. In our work, only triangular micropatterns displayed a significantly lower ALP activity compared to other shapes. The underlying reason remained unclear, but we proposed that it might be related to our *in vivo*-like culture substrate and the relatively small spreading areas for single cells. One recent study had confirmed that

unlike within a 2D culture environment, cell morphology alone was not a decisive factor of cell differentiation commitments in a 3D context. Instead, many other cues of the 3D environment, including the rigidity, stress relaxation, viscoelastic properties of the scaffold, might play a major role [209]. This might explain the absence of significant difference among the circular, quadrate and hexagonal groups. In our work, single cells cultured on a nanofibrous micropattern already exhibited *in vivo*-like behaviors, like the intracellularly and randomly distributed focal adhesion proteins and the formation of filopodia within the matrix, as shown in previous chapter. Moreover, since the micropatterns used in this part were relatively small (900 μm^2), the cellular morphologies were even more similar to those *in vivo*. However, the reason why triangular shape induced a significantly lower ALP activity remained unclear, which required further exploration.

For the polarization study, as we had discussed previously, there was no systemic studies exploring odontoblast polarization behaviors, and no standards had been established to evaluate whether a cell was polarized or not, especially at the molecular level [1, 5, 130, 210]. The only widely accepted feature of an odontoblast is its characteristic polarized cell morphology. Therefore, in our experimental design, we mainly rely on the morphological features (the formation of cellular process and the location of Golgi apparatus) to determine the polarization status of single hDPSCs on a micropattern. Results showed that discernable cellular processes could hardly be observed on a small micropattern, while on a large micropattern, the orientation of the processes didn't show a particular pattern, even though rectangular microislands with

different aspect ratios had been introduced to eliminate the surface isotropy (data not shown).

Another feature of odontoblast polarization was the translocation of Golgi apparatus. Hereby, an anti-GRASP65 immunofluorescent staining was employed to examine the location of Golgi apparatus. GRASP65 is a peripheral membrane protein anchored to the lipid bilayer of Golgi apparatus and is a commonly used marker for Golgi apparatus in immunohistochemistry. As the workshop for protein packaging and secretion, Golgi apparatus located at the juxtanuclear region between the nucleus and the process in a polarized odontoblast, which was believed to facilitate its function in efficiently packaging and processing proteins for secretion both at the tip of the odontoblast processes and at the terminal web where the process originated from the cell body. This location of Golgi apparatus had been used as a marker to determine cell polarization in an *in vitro* study [211], even though the cell type examined in that work was 3T3 fibroblasts. In our study, we similarly employed the immunofluorescent method to examine the location of Golgi apparatus, but it turned out that Golgi apparatus randomly distributed on the 2D NF-MP surface and no specific distribution pattern could be found, regardless of shapes or sizes of the NF-MPs (Fig. 14 G&H). Taking the cellular process and Golgi apparatus location together, it could be concluded that single hDPSC polarization could not be achieved on a 2D NF-MP surface.

3.4.2. Surface topography

To explore the influence of surface topography on hDPSC polarization and differentiation, NF-MPs and FF-MPs were generated to compare single hDPSC

behaviors. Firstly, we confirmed the micropatterning technique was applicable to both nanofibrous substrate and flat film substrate since hDPSCs seeded on both micropatterns were limited within the designated areas (Fig. 15) and the biocompatibility of both matrices were not impaired (Fig. 15 K&L). Then we examined the cell morphology of single hDPSCs on both matrices and found that hDPSCs on a NF-MP exhibited a narrower and *in vivo*-like morphology (Fig. 15 D&E) while hDPSCs on a FF-MP had a flattened, spreading shape (Fig. 15 I&J), which was similar to the cell morphology cultured on a tissue culture plate. Moreover, both circularity index (Fig. 15N) and aspect ratio (Fig. 15O) suggested that the nanofibrous architecture modulated hDPSCs to form an *in vivo*-like morphology.

Cell attachment is a process that involves a cell continuously stretching out multiple filopodia or lamellipodia to explore the surrounding matrix. Once the filopodia or lamellipodia detect and anchor to stable anchoring sites, they rapidly recruit attachment-related molecules and form initial focal adhesions. Focal adhesions act as a link between actin fibers and integrins. The formation and maturation of focal adhesions rely on the feedback from both the actin cytoskeleton and integrin-based exterior signal transduction. Mature focal adhesions are linear vinculin patches associated with the termini of stress fibers localized at the cell periphery, which were seen on a FF-MP. On the contrary, no typical focal adhesion patches could be seen on the NF-MP matrix, and instead the majority of the vinculin molecules accumulated into clusters underlying plasma membrane and distributed within the cytosol (Fig. 16A). The significantly less

focal adhesion amount and area (Fig. 16 B&C) were consistent with previous studies that nano-topography impaired the formation and maturation of focal adhesions [212].

One recent study reported that focal adhesion proteins couldn't be found between osteocyte dendrites and surrounding bone matrices and the authors proposed mentioned that if the cytoplasmic space between cell membrane and the tightly packed cross-linked actin filament bundles within (<20 nm) is insufficient to accommodate the normal array of focal adhesion adaptor proteins, that which typically occupy >40 nm of cytoplasmic depth, the focal adhesion might not form [213]. Although it's not known whether the significantly lower expression of focal adhesion proteins on the NF-MPs was also caused by this reason or not, it could be clearly seen that the actin filaments concentrated closely underlying the cell membrane on the nanofibrous surface, while on the contrary, they were much more distributed within the cytosol on a flat surface. Moreover, some researchers believed that the typical linear morphology of focal adhesions was actually an artificial result when culturing cells on flat tissue culture plates *in vitro*, and no such morphology could be observed *in vivo* [214]. Instead, the focal adhesion related proteins were mainly distributed within the cytosol *in vivo*, but they still played regulatory roles in modulating various cell behaviors [173].

ALP staining was performed on single hDPSCs seeded on NF-MPs and FF-MPs (Fig. 17A) and results showed that a higher ratio of single hDPSCs was stained positive on the NF-MPs (Fig. 17B) and their relative ALP activity was higher than those on the FF-MPs (Fig. 17C), suggesting nanofibrous architecture promoted hDPSC odonto-lineage differentiation. To explore the mechanism of the enhanced odontogenic

differentiation on NF-MPs, we used a fluorescence dye phalloidin to trace the location of F-actin and the formation of stress fibers within single hDPSCs (Fig. 15 E&J) since multiple previous studies had proposed the association between stress fibers and osteogenesis [147]. It's found that single hDPSCs on the NF-MP surface possessed significantly less stress fibers than those on the FF-MP surface (Fig. 15P). RhoA, a member of small GTPase family, is a critical regulator of actin cytoskeleton. ROCK is the effector of RhoA which links to myosin II, the other major component of stress fiber besides F-actin to regulate actin contractility. When the inhibitor of ROCK (Y-27632) was added into the culture medium to interrupt the RhoA signaling pathway, the spreading areas of single hDPSCs decreased (Fig. 18B) and the odontogenic differentiation was also significantly impaired as indicated by the decreased ALP-positive ratio (Fig. 18C) and relative ALP activities (Fig. 18D). These results revealed a critical role of actomyosin cytoskeleton in hDPSC odontogenic differentiation on both the NF-MPs and the FF-MPs.

YAP1 is critical in cell-matrix adhesion-mediated signaling and mechano-transduction [205-207], and is expressed both in the cytoplasm and in the nucleus. The cytoplasmic YAP1 is functionally latent while the nuclear YAP1 functions as a transcriptional co-activator. The shuffling of YAP1 between the nucleus and cytosol makes it as an indicator of ECM mechanical property and cellular tension. When cells were cultured on a stiff surface or forced to spread over a large area, YAP1 could sense actin tensions and transfer its location to the nucleus. Our results found the nuclear YAP1 expression accounted for 46% of the total YAP1 expression on the NF-MPs,

while for 62% on the FF-MPs (Fig. 19B). Considering the relatively lower amount of stress fibers on the NF-MPs, this difference in YAP1 distribution was consistent with previous studies that YAP1 nuclear expression level is positively related to the cytoskeleton tension [206]. Moreover, Y-27632 decreased the nuclear YAP1 expression on both NF-MPs and FF-MPs, especially on the FF-MPs (Fig. 19C). Since YAP1 nuclear translocation depends on actin network [215], the decrease in nuclear YAP1 expression might be a result of an impaired actin polymerization by Y-27632.

In osteogenesis, YAP1 is expressed in immature osteoprogenitor cells and the osteogenesis is blocked by a high level of nuclear YAP1 [216]. It was documented that nuclear YAP1 suppressed the activity of Runx2 by forming the YAP1/Runx2 complex to restrict the effect of Runx2 that served as a key transcriptional factor at bone-specific osteocalcin promoter [217, 218]. In our study, we found that Runx2 was expressed in the nucleus of single hDPSCs both on the NF-MPs and FF-MPs, and the expression level on the NF-MPs was much stronger than that on the FF-MPs (Fig. 20B), which further confirmed the pro-odontogenesis effect of the nanofibrous architecture. Moreover, the higher Runx2 expression and the cytoplasmic location of YAP1 on the NF-MP also indicated the negative relationship between the nuclear YAP1 content and the Runx2 activity. When the ROCK activity was inhibited by adding Y-27632, Runx2 expression was decreased on both the NF-MPs and FF-MPs. The Runx2 signal was hardly found on the FF-MPs, while it was observed in both the nucleus and the cytoplasm on the NF-MPs (Fig. 20A). The decrease of Runx2 expression in nucleus further demonstrated that odontogenesis was dependent on the RhoA/ROCK signaling pathway.

Runx2 proteins are latent in the cytoplasm, and need to be transferred into the nucleus to play its role as the master transcriptional factor in odontogenesis [219]. The cytoplasmic Runx2 expression had been detected when microtubules were stabilized by taxol [220]. While in our study, the inhibition of RhoA/ROCK signaling pathway also induced a cytoplasmic Runx2 expression on the NF-MPs (Fig. 20B). Considering that ROCK can regulate microtubule acetylation [221], a post-translational modification that increased the stability of microtubules [222], it is likely that this cytoplasmic expression of Runx2 was also owing to the dysfunction of microtubules, which might be induced by Y-27632. Therefore, the inhibiting of RhoA/ROCK not only decreased the synthesis of Runx2, but also hampered its translocation from the cytoplasm to the nucleus.

It should be noted that RhoA/ROCK is a ubiquitous signaling pathway, and the addition of Y-27632, a strong inhibitor of RhoA/ROCK, not only influenced the YAP1 expression, but also affected many other downstream molecules related to osteo/odontogenesis. For example, MAPK pathway [223] and CTGF pathway [224] have also been demonstratred to mediate in RhoA/ROCK regulated osteogenesis. Therefore, it is possible to observe a decreased nuclear YAP1 expression and a decreased odontogenesis (e.g. lower ALP activity) at the same time, but how other mechanisms participated in this process required further studies.

Based on the aforementioned discussions, a possible molecular signaling pathway of how nanofibrous architecture interacted with hDPSCs was summarized. When a hDPSC initiated its contact with the nanofibers, the integrin receptors on the plasma membrane were activated, and subsequently fewer focal adhesions were formed

compared to the flat surface. The fewer focal adhesion leaded to a relatively low activity of RhoA. Since RhoA positively regulates the formation of stress fibers via its effector ROCK and its downstream myosin, fewer stress fibers were formed on the nanofibers. Meanwhile, RhoA/ROCK regulated actin polymerization, which was critical in the cytoplasm-to-nucleus translocation of YAP1, therefore less nuclear YAP1 expression was observed on nanofibers. As a result, the restrained effect of YAP1 on Runx2 was partially released and the amount of functional Runx2 was increased on the nanofibers. As the master transcription factor in osteo/odontogenesis, Runx2 initiated the differentiation of single hDPSCs on the nanofibers and promoted the synthesis of ALP molecules, leading to an enhanced hDPSC differentiation on the nanofibrous architecture.

3.4.3. Three-dimensional tubular architecture

Although systemic research studies focusing on how biophysical factors regulate odontoblast polarization and differentiation were lacking at this time, we were still able to find some clues from several previous literatures. One shared conclusion from these studies was that dental stem cells cultured on regular 2D substrate don't spontaneously polarize into an odontoblast-like morphology unless additional stimulus was applied. For example, some researchers believe that during primary dentin formation, the embryonic dental epithelium induces underlying mesenchyme to undergo odontogenesis by promoting a cell compaction process, so they artificially compacted embryonic mandible mesenchymal cells using mechanic approaches, which managed to induce odontoblast differentiation and initiate tooth differentiation [141]. Several other groups believed that

the tubular structure was an essential factor in dentiongenesis, so biomimetic scaffolds with tubular channels [138, 174] or natural dentin slides [143, 144] where dentinal tubules were chemically or physically enlarged were employed to induce odontoblast polarization and tubular dentin formation. Another group combined the application of mechanical force (compression force) and tubular structure and achieved successful odontoblastic differentiation from non-dental mesenchymal stem cells [225]. Consistent with previous reports, our results in this chapter that focused on single odontoblast polarization further illustrated that single hDPSCs failed to polarize on micropatterns constructed on the 2D nanofibrous substrate and a 3D tubular architecture was critical in inducing hDPSC polarization and differentiation.

In this chapter, we further modified the parameters of the laser-drilling technique to achieve dentinal tubule-like microchannels within the NF-MP microislands. After cells were seeded on the NF-MTs, the cell occupation ratio and the single cell ratio on the NF-MT scaffolds were similar to those on NF-MP scaffolds (Fig. 21 E&J). Together with the SEM-EDS analysis (Fig. 9C), these results indicated that the laser-drilling process didn't change the chemical composition of surrounding nanofibers or influence the cell-limiting function of PEGDA, which ensured the launch of following studies.

Cell morphologies observations showed that single hDPSCs on NF-MTs exhibited a polarized morphology identical to *in vivo* odontoblasts. Single hDPSCs formed a long process which extended into laser-drilled microchannels and even mini-branches were formed within the porous space of nanofibers. Moreover, the main cell body, which displayed a hemispherical morphology stayed outside the microchannels

and so did the nucleus (Fig. 21 H&I). In comparison, single hDPSCs on NF-MPs (Fig. 21 C&D) were more morphologically similar to those cultured on 2D surfaces. Besides, the immunofluorescence staining showed that all three cytoskeletal elements (Fig. 22 C&D) were found lining the cell cortex throughout the entire process trunk, while the mini-branches contained only microfilaments. Moreover, the expressions of microtubule and intermediate filament could be clearly found even when the hDPSC process formation was just initiated, and this was consistent with the description of *in vivo* odontoblasts [226], indicating a functional participation of all three cytoskeletal elements in the cytological activities of odontoblasts.

The expression intensities of cell adhesion markers integrin β-1 (Fig. 22A) and vinculin (Fig. 22B) were low, especially around the cellular process area, that hardly any integrin or vinculin signals could be detected. When compared to their expression on a 2D NF-MP surface , their intensities on the 3D NF-MT surface were even lower. Previous studies reported that integrin β-1 could be found in *in vivo* odontoblasts and even within their intradentinal dendrites, and its expression level was significantly increased with the maturation of odontoblasts [226]. However, when the integrin β-1 expression was conditionally knocked down in a transgenic mice, no obvious phenotypes were observed within odontoblasts or dentin [227].Therefore, the function of integrin β-1 in odontoblasts remained unclarified. It's noteworthy that low or even absent expression of focal adhesion markers between the cell-matrix interface was a common phenomenon within a 3D *in vitro* culture environment, but it's generally

believed that despite their absence in detection, those proteins still play regulatory roles in modulating cell behaviors like adhesion and motility [173].

The cell tracking study indicated that the ratio of cell with process and the length of processes were both positively associated with culture time (Fig. 23 B&C), and they could be utilized as a marker to trace the polarization status of cells cultured on NF-MTs. Apart from that, the translocation of Golgi apparatus is another unique feature of odontoblast polarization and this was also recapitulated within a hDPSC cultured on a 3D NF-MT scaffold. The relative locations of Golgi apparatus to the nucleus at different timepoints were traced similarly (Fig. 24A) and a coordinate system was established to quantify each position (Fig. 24B). Results showed Golgi apparatus initially located close to the nucleus in the main cell body, while with the formation of hDPSC process, it gradually moved to a position between the nucleus and the cellular process (Fig. 24C).

Another organelle worth mentioning is mitochondria, the supply of cellular energy. The presence of mitochondria in odontoblast process was confirmed even in mature dentin, suggesting a considerably metabolic activity in the process regardless its remote location from the nucleus [228]. Moreover, the autophagy of mitochondria, together with the decrease in mitochondria amount in odontoblasts indicates the aging of the cell and an eventual decline in cell functions [229, 230]. Adenovirus transfection was used to examine the mitochondria location within the cellular process of single hDPSCs at different timepoints (Fig. 25A). It’s found that the mitochondria mainly accumulated at the perinuclear region while a considerable amount of mitochondria could also be seen at the tip of the process within a polarized hDPSC (Fig. 25A). Both the movement of

Golgi apparatus and mitochondria implied that the cellular processes formed within the laser-drilled microchannels were highly active, and more importantly, they predicted a unidirectional secretion of the polarized hDPSCs on the NF-MT scaffold. The immunofluorescent staining of collagen I surrounding the cellular process further verified this point of view (Fig. 25B).

The ALP positive ratio of single hDPSCs cultured on a NF-MT was significantly higher than that on the NF-MP after 3 days' culture (Fig. 25C), implying that hDPSC differentiation was accelerated on the 3D tubular architecture during the formation of its cellular process. Moreover, the ALP-positive signals had been observed within the cellular process area in our preliminary studies, which further confirmed that the cellular process formed within the laser-drilled microchannels were functionally active. On the other hand, it's technically very difficult to section ALP-stained NF-MP or NF-MT scaffolds with good preservation of the ALP signals, therefore, using the relative ALP intensity as a quantitative criterion to evaluate single hDPSC differentiation ability was not appropriate on a NF-MT scaffold.

Therefore, the generation of 3D tubular architecture on the NF-MPs successfully recapitulated the polarization behavior of odontoblasts *in vitro*. Moreover, various cellular behaviors, including Golgi apparatus translocation, mitochondria movement, collagen I secretion and ALP activity, indicated that the cellular processes of polarized hDPSCs were physiological functional on the NF-MTs.

3.4.4. Gravity

Gravity, an indisputable biophysical factor, has been found to influence various types of biological activities [231] including stem cell differentiation and self-renew [232]. However, its role in *in vitro* odontoblast polarization remains unclear. Since we usually culture hDPSCs on our *in vitro* scaffold, it might be proposed that the formation of cellular process was resulted from the influence of gravity. Therefore, it's necessary to examine the effect of gravity on odontoblast polarization and differentiation. According to our data, when the hDPSC-scaffold complex was artificially rotated vertically (Fig. 26A), the polarization behaviors of single hDPSC were impacted. The ratio of polarized cells (Fig. 26B), the average length of cellular processes (Fig. 26C) and the moving rate of Golgi apparatus (Fig. 26D) were all decreased. Moreover, the larger degree the hDPSC-scaffold complex was rotated, the greater influence was imposed by the altered-gravity microenvironment, which implied that gravity was a regulatory factor in inducing hDPSC polarization *in vitro*. However, the influence of gravity was not imperative, since even within the 180-degree rotated microenvironment, there was still 2/3 single hDPSCs that successfully polarized on the 3D tubular scaffold (Fig. 26B), indicating that gravity was a contributing rather than essential factor in hDPSC polarization. Moreover, on the rotated NF-MT scaffolds, the ALP positive ratio of single hDPSC was decreased compared to the control group (Fig. 26E), implying that gravity also regulated hDPSC differentiation behaviors. The synchronous change in hDPSC polarization level and differentiation level further confirmed the close relationship between cell morphology and cell differentiation.

Previous studies have attempted to explore the molecular mechanisms as to how altered gravitational environment regulates stem cell behaviors, including cell proliferation [200], differentiation [231, 233], cytoskeleton distribution [234, 235], stemness [236] and stem cell marker expression [237], and so on. For example, one study [238] reported that osteoblasts exposed to microgravity displayed lower functional activities. Apart from that, impacted cellular architectures, including shorter and wavier microtubules, smaller and fewer focal adhesions, and thinner cortical actin and stress fibers, were observed within the cells and were believed to be the causal factor leading to the decreased function level. Another study found that gravity modulated mechanotransduction pathways with the tool of transcriptomic analysis and found that epigenetic behaviors, such as chromatin re-modeling and DNA methylation, contributed to the altered gene expression [239]. A later study found microgravity attenuated myogenesis by controlling DNA methylation status of Myod1, a critical gene related to myogenesis [240], further confirmed that epigenetic modulation might be a key factor as to the effect of microgravity on cell behaviors. However, our scaffold which was designed for single cell observation couldn't allow for a quick and efficient cell harvest technically, thus the commonly used molecular analysis like RT-PCR, Western Blot or the transcriptomic analysis could hardly be performed. Therefore, further mechanism underling how the tubular architecture promotes hDPSC polarization and differentiation, and how gravity partially influences this process remained unanswered, and more advanced techniques are required.

In summary, in this chapter the NF-MP design was used as a platform to examine how various biophysical factors influence single hDPSC differentiation and polarization *in vitro*. Parameters of the NF-MP scaffold including its micropattern morphology, surface topography and 3D spatial architecture were examined. Results showed that spreading area, shape and the nanofibrous surface topography all influenced hDPSC differentiation behaviors, while hDPSC polarization couldn't be achieved on any of these 2D platforms. The 3D tubular architecture also enhanced hDPSC differentiation and more importantly, it enabled single hDPSC to polarize *in vitro*. Furthermore, the effect of gravity in inducing hDPSC polarization and differentiation was examined on the NF-MT platform and it turned out gravity was a contributory but not essential factor for hDPSC polarization and differentiation.

4. IDENTIFICATION OF BIOCHEMICAL FACTORS THAT REGULATE SINGLE HDPSC POLARIZATION AND DIFFERENTIATION

4.1. Introduction

4.1.1. Intercellular communication

Intercellular communication play important roles in various types of biological activities. Odontoblasts are a dense layer of cells that reside closely to each other *in vivo*. Moreover, all 4 types of intercellular junctions including adherens junctions [57], tight junctions [62-66], gap junctions [58, 59], and desmosomes [60, 61] have been found between adjacent odontoblasts, indicating that intercellular signals can be transmitted via direct (intercellular junctions) ways. Among the 4 intercellular junctions, gap junction has been found to play a critical role in odontoblast maturation and function from both *in vitro* and *in vivo* studies [241]. For example, Connexin 43 is found critical to dentin mineralization [242], and the knockout of pannexin 3, another member of the gap junction protein family, in tooth germs also led to impaired odontoblast proliferation and differentiation [243]. Previous studies have attempted to explore the role of intercellular communication in rat BMSC differentiation using micropatterning technique and found that both osteogenic and adipogenic differentiation of rat BMSCs were significantly enhanced with the existence of direct cell-cell contact [159]. Now with the development of our 3D tubular micropatterning technique, the exploration of intercellular communication in odontoblast behaviors becomes possible.

4.1.2. Growth factors

Previous studies have attempted to explore biochemical signals that may play a role in odontoblast polarization. Ruth's group suggested multiple growth factors, including TGF-β superfamily [133], growth hormone receptor [244], IGF and receptors [126], EGFs [124], NGF and receptors [125], participated in that process using immunolocalization and/or in situ hybridizations approaches, while the exact functions of these proteins remained ambiguous. Recent years have witnessed the advancement of genetic engineering techniques, which have enabled the exploration of function of various biochemical factors in primary dentinogenesis at molecular level [245, 246]. Growth factors and transcriptional factors like BMP-2 [247], Wnt10a [248], Dlx-3 [137], DSPP [249], DMP-1 [131, 250], Runx2 [127] are found indispensable in inducing odontoblast polarization using gene-modified animal models. However, although this gene-modified animal model approach has contributed greatly in identifying the roles of multiple biochemical factors, the complicated *in vivo* environment makes it impossible to solely focusing on odontoblasts and the proposed regulatory factors without signal interference from various other interwinding factors.

In vitro studies have also been employed to explore the effects of those growth factors on hDPSCs and many achievements have been obtained from those studies, for example, EGF and FGF have started to be routinely used in DPSC differentiation medium in many experiments [251, 252]. However, it's noteworthy that even though their influence on hDPSC differentiation have been widely explored, their roles in regulating hDPSC polarization have seldomly be reported owing to the lack of an

appropriate study model. Moreover, as we discussed in previous chapter, *in vitro* studies also possess shortcomings like the difficulty in single cell isolation and the non-biomimetic culture conditions. Therefore, even though it's well accepted that growth factors play critical roles in odontoblast maturation and dentinogenesis, their exact roles in odontoblast polarization remain unclear. Our novel *in vitro* platform provides a biomimetic microenvironment for single hDPSC, thus it's possible to explore the role of those growth factors on odontoblast polarization behaviors.

4.1.3. Cell type

Dental pulp stem cells (DPSCs) and bone marrow stromal cells (BMSCs) share a similar immunophenotypes *in vitro* [253] and comparable potentials towards osteogenic [254], adipogenic, chondrogenic [253, 255], angiogenic [256], neurogenic [257] and even hepatogenic [258] differentiations. Plenty of *in vitro* studies have proved that DPSCs cultured in osteogenic medium exhibited a osteoblast-like phenotype, including their expression of typical osteoblast markers and production of mineralized matrix components. Moreover, when DPSCs were used in *in vivo* dentin regeneration studies, they were often embedded within the deposited matrix which were positive for osteogenic specific markers and displayed a osteocyte-like morphology. All these previous work indicate that DPSCs could behave like osteoblasts and be easily transdifferentiated into osteocytes, however, transition in the opposite direction that BMSCs express odontogenic markers and form tubular dentin has seldomly been reported. In a recent study, human BMSCs, as well as the C3H10T1/2 connective tissue cell lines, were reported to display a odontoblast-like morphology with odontoblastic

cellular processes with the induction of a preameloblast-derived protein CPNE7. Moreover, when those non-dental cells were seeded on the tubular dentin and implanted *in vivo*, dentin-like mineralized tissues were formed and the characteristic dentinal tubules were regenerated on the existing dentinal wall [259]. This work implied that the BMSC-to-odontoblast transition is not unfeasible, instead it could be achieved with the induction of specific biophysical and biochemical factors. It has been shown previously that our novel 3D tubular micropatterning scaffold is a potent inductor for DPSC-to-odontoblast polarization, therefore, we would like to examine whether BMSC-to-odontoblast transition could be similarly achieved on this 3D tubular scaffold.

4.1.4. Inhibitors

The cytoskeletal system is the backbone of a cell and is a complex and dynamic network of filament proteins in the cytosol. It contains 3 dynamic components, including microfilament, microtubule and intermediate filament. All three components coordinate with each other and all the organelles precisely to participate in all types of cellular activities. Cell polarization is no exception. Mediated by the dynamic disassembly and reassembly of cytoskeletons, cell polarization has been defined as the asymmetric distribution of cytoskeletons within a cell. In our previous chapter, it had been proved that all 3 cytoskeletal elements exist in the cellular process of single DPSC on a NF-MT, but their importance in the hDPSC polarization process needs further illustration.

Moreover, we had proved that the RhoA/ROCK signaling pathway played critical roles in modulating hDPSC intracellular tension and differentiation in previous chapter, but since hDPSC polarization couldn’t be achieved on the 2D substrate, the role

of RhoA/ROCK signaling pathway in hDPSC polarization hasn't been checked. Similarly, the involvement of integrin β-1 had been confirmed in the interaction between single hDPSC and the gelatin nanofibers, but as a critical regulator in cell adhesion and mechanotransduction, its role in hDPSC polarization remained unknown. Therefore, in this part, we aim to use several inhibitory drugs to examine the vital effects of cytoskeletal integrity and integrin-mediated adhesion on the hDSPC polarization behaviors.

4.2. Materials and Methods

4.2.1. Micropattern fabrication

The fabrication of NF-MT was performed as described previously. To satisfy the need for single hDPSC observation, a photomask containing 450-μm^2 circular shades was used in the photolithography process and 1 tubule with a diameter ranging from 4-6 μm was drilled by lasers within each microisland following the protocol described in previous chapters. When 2-cell microislands were needed, a photomask containing 900-μm^2 circular shades was applied and 2 tubules were drilled within each microisland.

4.2.2. Cell culture

Human DPSCs were cultured as previously described. Primary rat BMSCs were isolated from rat bone marrows following a standard protocol [260]. The animal surgical procedures were approved by the University Committee on the Use and Care of Animals (UCUCA) of the Texas A&M University College of Dentistry. Briefly, 5-week-old SD rats were sacrificed after anesthesia, and both femora and tibia were aseptically removed. Bone marrow was flushed down by a syringe filled with α-modified essential

medium (a-MEM) (Gibco, A1049001) supplemented with 10% (v/v) FBS (Gibco, 26140079) and 1% penicillin/streptomycin (Sigma, P333). The released cells were collected and cultured in a 75 cm^2 culture flasks and maintained in a 37°C incubator. Cells were allowed to attach for 72 hours, then non-adherent cells were removed and cells attached on the flasks were labeled as Passage 0 (P0). BMSCs of P3-P5 were used in this study. For differentiation assays, 1 mM dexamethasone, 50 mM ascorbic acid-2-phosphate, and 10 mM β-glycerophosphate were added to the medium 24 hours after cell seeding. Cell culture medium was changed every 3 days.

For ROCK inhibition assay, 2 μM Y-27632 (Calbiochem, 688000) was added to the culture medium 4 hours after cell seeding. To inhibit actin polymerization, 1μM cytochalasin D (Sigma, C8273) was added to the culture medium 2 hours after cell seeding. To inhibit microtubule polymerization, 1 μg/ml nocodazole (Sigma, M1404) was added to the culture medium 2 hours after cell seeding. To inhibit focal adhesion formation, anti-integrin β1 antibody (10μg/ml, Abcam 179471) was added to the culture medium 1 hour after cell seeding. To inhibit the formation of gap junction, 40 μM 18α-Glycyrrhetinic acid (AGA) (Sigma, G8503) was added into the medium 2 hours after cell seeding.

For the study of growth factors, as shown in Table 4.1, eight types of growth factors were purchased from vendor and diluted into desirable concentrations. For the exploration of these growth factors on odontoblast polarization, 4 concentrations in each type were added to the single-cell single-tubule system and cultured for 24 hours.

Afterwards, samples were harvested to measure their process length and the movement of Golgi apparatus.

Table 4.1 List of growth factors

	Label	Concentration
BMP-2	R&D 355-BM-010	50, 100, 200, 500ng/ml
HGF	R&D 294-HG-005	50, 100, 200, 500ng/ml
EGF	R&D 236-EG-200	50, 100, 200, 500ng/ml
FGF	R&D 233-FB-025	50, 100, 200, 500ng/ml
Wnt-5a	R&D 645-WN-010	50, 100, 200, 500ng/ml
Shh, N-Terminus	R&D 314-SH-025	50, 100, 200, 500ng/ml
TGF-beta 1	R&D 240-B-002	50, 100, 200, 500ng/ml
BMP-4	R&D 314-BP-010	50, 100, 200, 500ng/ml

4.2.3. ALP staining and immunofluorescence staining

The ALP staining procedures were performed following previous protocols and the stained scaffolds were loaded on a glass slide and scanned with a slide scanner. On the 450-μm^2 NF-MTs, the total number of single-cell microislands (A) was counted on a scaffold with the help of nucleus staining, and then among those microislands, the number of ALP-positive single hDPSCs were counted and recorded as B. Each ALP-positive cell on a 450-μm^2 NF-MT microisland was recorded as 1 cell, therefore the ALP-positive cell ratio was calculated as B/A×100%. On the 900-μm^2 NF-MTs, the total number of 2-cell microislands was counted (C) and then among them all microislands

where ALP-positive signal could be detected were screen captured. The number of NF-MTs was counted as D if both cells on a 2-cell NF-MT microisland were ALP-positive, while the number of NF-MTs was counted as E if only one cell on a 2-cell NF-MT microisland was ALP-positive. Then the ALP-positive cell ratio of the 2-cell NF-MT was calculated as (2D+E)/2C×100%.

Nucleus, actin and Golgi immunofluorescent staining were performed as previously described. Additional first antibodies used in this chapter include anti-ZO1 antibody (1:50, Invitrogen, #617300), anti-Connexin 43 antibody (1:200, Abcam, ab11370) and anti-DSP antibody (1:200, Abcam, ab216892)

4.3. Results

4.3.1. Intercellular communication

To explore the effect of cell-cell interaction on the polarization and differentiation behaviors of hDPSCs, firstly 2 types of micropatterns were generated and employed as platforms. For the control group where no intercellular communication existed, NF-MPs with a surface area of 450-μm^2 were fabricated and only 1 microchannel was drilled within each microisland. After cell seeding, only NF-MTs accommodating single cells (1-cell NF-MT) were selected for observation. For the experimental group with intercellular communication, NF-MPs with a surface area of 900-μm^2 were fabricated to eliminate the influence of cell spreading area and 2 microchannels were drilled within each NF-MP (Fig. 27 A&C), and after cell seeding, only NF-MTs accommodating 2 cells (2-cell NF-M2T) were selected for observation.

Both confocal stacking scan and the lateral section images showed that 2 cellular processes could be formed inside the laser-drilled microchannels of a 2-cell NF-M2T, but above the microchannels, the cytosol of the 2 cells tended to mingle with each other and it's difficult to distinguish the boundary between them (Fig. 27 B&D). Then the cellular process formation pattern on a NF-M2T scaffold was further examined after hDPSCs were seeded for 24 hours. Results showed that there were 75.8% NF-M2T microislands were occupied by cells, which was similar to that on a NF-MT scaffold (79%) (Fig. 27F). Among all those 2 cell-occupied NF-M2T microislands, the ratio of NF-M2Ts where no cellular process was 24.2%, the ratio of NF-M2Ts where 1 process was formed was 16.1% and the ratio of NF-M2Ts where 2 processes were formed was 59.7% (Fig. 27E). Moreover, lengths of the processes were measured to explore whether the hDPSC polarization behaviors were different on NF-M2T microislands where intercellular communication existed. Results showed that the average process length was 15.79 μm on 2-cell NF-M2T microislands, and when compared to the process length (15.32 μm) on 1-cell NF-MT microislands, no significant difference was found (Fig. 27G). To be noted, in this part, all 2-cell NF-M2T microislands were taken into measurement, including those with no cellular process formed and in this situation, the process length would be recorded as zero.

Afterwards, the hDSPC differentiation behaviors were examined on the NF-M2T microislands. ALP staining was used as the evaluation criterion again and all NF-M2T microislands where ALP positive signals were detected were recorded as positive, regardless of the number of cells which were stained as positive (Fig. 28A). Results

showed that the ALP positive ratio on the 2-cell NF-M2T microislands was 30%, which was significantly higher than that on the 1-cell NF-MT microislands (10.8%) (Fig. 28B). Moreover, anti-Collagen I immunofluorescence staining was performed on the 2 types of NF-MT scaffolds. It's observed that the staining intensity per cell was much stronger on the 2-cell NF-M2Ts when compared to the 1-cell NF-MTs (Fig. 28C). However, when AGA, a gap junction inhibitor, was added to the culture system, the ALP positive ratio on the NF-M2Ts decreased to 14.2% and the significant difference between the 1-cell NF-MTs and 2-cell NF-M2Ts disappeared (Fig. 28B).

4.3.2. Growth factors

In this part, we selected 8 types of growth factors which had previously been reported to play a role in primary odontoblast differentiation (Table 1) and explored their influence on single hDPSC polarization *in vitro*. Four gradual concentrations of each growth factor were designed and added to the culture system of single hDPSC on a NF-MT scaffold, respectively. According to the results, it's found that HGF (50, 100, 200 ng/ml), FGF (50, 100, 200 ng/ml), BMP-2 (100 ng/ml), BMP-4 (200 ng/ml), Shh (100, 200 ng/ml) and Wnt5a (100, 200, 500 ng/ml) exhibited significant promoting effects on hDPSC polarization. Other groups (except for the 200ng/ml TGF-β group) exhibited a slight but not significantly promoting effect and the 200ng/ml TGF-β group seemed to have a unfavorable effect on hDPSC cell process formation but this effect was not statistically significant.

Apart from those groups, it's interesting to find that even higher concentration of growth factors, including 500ng/ml EGF, 500ng/ml TGF-β, 500ng/ml FGF, 500ng/ml

HGF, 500ng/ml BMP2, 500ng/ml BMP4, 500ng/ml Shh, impaired the cell-limitation effect of PEGDA. After 24 hours' culture, single hDPSCs stained with phallodin-633 were found to stretch out cellular processes that broke down the boundaries of the microislands although their nuclei remained inside boundaries, and some cells even contacted with other cells from neighboring microislands (Fig. 30A). Therefore, data from those groups were excluded from our analysis. Following this phenomenon, we cultured hDPSCs in a very low concentration on the GelMA nanofibrous matrix without PEGDA or laser-drilled tubules and similarly added growth factors (Shh, for example) of different concentrations (0, 50, 100, 200, 500ng/ml) to see whether hDPSC polarization can be observed on a 2D substrate. HDPSCs were similarly culture for 24 hours before they were fixed and stained with Golgi, nucleus and actin filaments. An isolated hDPSC should fulfill 2 standards simultaneously to be recognized as a polarized cell that its aspect ratio should be no smaller than 2.0 and its Golgi apparatus should locate beside the nucleus in the long axis of the cell. We counted the number of polarized cells and divided it by the number of total attached cells to obtain the polarized cell ratio (Fig. 30C). However, when comparing the ratio of polarized cells among the 5 concentration groups, no significant difference was found (Fig. 30B).

4.3.3. Cell type

To explore whether osteogenic lineage cells could be induced into odontoblast-like cells, rat BMSCs were trypsinized into single cells and seeded on the NF-MT microislands in a way exactly same to that of hDPSC seeding. Results found that the biocompatibility, which was indicated by the cell occupation ratio and single cell ratio,

and selectivity of rBMSCs on NF-MT scaffolds were almost the same to those of hDPSCs. From the lateral view SEM images and confocal images, it was clearly seen that a single rBMSC formed a noticeable cellular process stretching into the laser-drilled microchannels with the nucleus residing outside the microchannels (Fig. 31 A&B), displaying a morphology identical to a polarized hDPSC (Fig. 31 E&F). Golgi apparatus within rBMSCs also translocated to a supranuclear area between the nucleus and the process tip, further confirming the polarized odontoblast-like status (Fig. 31G). To explore possible differences in the polarization behaviors more comprehensively, we selected 5 timepoints (12, 24, 36, 72 and 96 hours after seeding) to trace the dynamic cytologic change of single rBMSCs seeded on a NF-MT scaffold. In the meantime, the ratio of cell with process and the average process length were measured. Results showed that at any timepoint, the morphology of rBMSCs was similar to that of hDPSCs. Quantitative analysis showed no significant difference in either the ratio of cell with process (Fig. 31I) or the average process length (Fig. 31J) between the 2 cell types. Moreover, the Golgi apparatus translocating rate and final position within single rBMSCs were also similar to those within single hDPSCs (Fig. 31K).

As to the cellular function of polarized rBMSCs on the microislands, ALP staining and anti-DSP immunofluorescence staining were performed. The ALP positive ratio of single rBMSCs was 46.4% on a non-tubular NF-MP scaffold after cells were seeded for 3 days, while it increased to 61.6% on a NF-MT scaffold (Fig. 31L). Apart from that, the ALP positive ratios of rBMSCs were significantly higher than hDPSCs on both scaffolds, which was 9.6% on a NF-MP scaffold and 13.9% on a NF-MT scaffold,

respectively (Fig. 31L). Moreover, the anti-DSP staining of single rBMSCs on a NF-MT was also performed and it showed that BMSC could also express DSP protein, but the intensity was very low (Fig. 31H), not comparable to that of hDPSCs (Fig. 31D).

4.3.4. Inhibitors

To examine the role of microfilament in this process, a actin polymerization inhibitor cytochalasin D was added to the culture medium after cell seeding and the NF-MT samples were harvested after 24 hours. Cytochalasin D led to a cell attachment ratio of only 3.2%, exhibiting a tremendous reduction compared to that under normal culture conditions (70.23%) (Fig. 32A). Moreover, cellular processes could be hardly detected within the those attached (Fig. 32 B&C).

To investigate the effect of microtubule in inducing single DPSC polarization, a microtubule polymerization inhibitor nocodazole was similarly added into the culture system. Results showed it also greatly reduced the cell attachment ratio (43.25%) (Fig. 32A) and hDPSC cellular process formation, since the ratio of cell with process was only 5.98% (Fig. 32B) and the average length of the processes was only 0.59 μm (Fig. 32C) while in normal culture conditions it's 73% and 15.8 μm after 24 hours' culture, respectively. Moreover, the unidirectional translocation of Golgi within single hDSPCs could not be detected, instead, Golgi signals could be observed randomly around the nucleus (Fig. 32 D).

Afterwards, the effect of inhibiting RhoA/ROCK signaling pathway on hDPSC polarization was explored by adding Y-27632 into the culture medium. Results showed that its cell attachment ratio (67.67%) (Fig. 32A) was comparable to that in normal

culture conditions, while the cellular process formation was significantly impacted that the ratio of cell with process decreased to 48.1% (Fig. 32B) and the process length was decreased to 9.56 μm (Fig. 32C). The movement of Golgi apparatus could be detected after the inhibition of ROCK, but it stopped at a juxtanuclear position in the main cell body or at the initiating area of the cellular process (Fig. 32E).

The addition of anti-integrin β1 antibody impaired the hDPSC adhesion on the NF-MT microislands that a lower amount of single hDPSCs (56%) got attached (Fig. 32A). Its influence on hDPSC polarization was evident that less than 9.7% of single hDPSCs formed cellular process within the microchannels (Fig. 32B) and the average length of the processes decreased to 1.32 μm (Fig. 32C). Moreover, a obvious translocation of Golgi apparatus couldn't be observed as well (Fig. 32F).

4.4. Discussion

4.4.1. Intercellular communication

Intercellular communication is an inevitable signal source for both *in vivo* and *in vitro* cells and its importance has been known for a long time [261, 262]. It can be mainly divided into 2 parts, direct cell-cell contact via intercellular junctions and indirect cell-cell communication via paracrine signals. As to odontoblast polarization and differentiation, it's well documented that during primary odontogenesis, preodontoblasts received signal from surrounding preaemloblasts, withdrew from the mitotic cell cycle and started to differentiate in a sequential order [1]. However, if we focus on the change of one single preodontoblast, what signal it receives and responses to remains ambiguous. The signal may come from corresponding preameloblasts via paracrine,

from the adjacent odontoblasts via direct cell-cell contact, from the adjacent odontoblasts via paracrine, or from the combination of two or 3 of these factors.

The exploration of cell-cell contact in osteogenesis has started for more than 30 years [263-265]. In earlier time, researchers attempting to explore the effect of intercellular interaction used approaches like seeding cells at very low densities or adding intercellular junction inhibitors to prevent direct cell-cell contact [147]. Now with the advancement of micropatterning techniques, which made single cell entrapment possible, researchers are able to examine the intercellular communication in a more reliable way [147, 159, 266, 267]. For example, one research group designed micropatterns of particular shapes to manipulate the number of cell-cell contacts and examined its association with BMSC differentiation behaviors. They found that a fairly linear relationship existed between the cell-cell contact number and the osteogenesis or adipogenesis per cell [159], which indicated that intercellular communication was a favorable factor in inducing both adipogenic and osteogenic lineage commitments of BMSCs. Moreover, both the traditional low density culture approach [147] and the micropatterning approach [159] confirmed that among the 4 types of intercellular junctions, gap junction was the critical one in the cell-cell communication that by inhibiting the assembly of gap junction, the accelerated ALP activity or adipogenesis returned to normal level. Moreover, when Connexin 43 was overexpressed in MC3T3 cells, the activation of Runx2 in response to FGF2 was greatly enhanced and it's found this process was dependent on Connexin 43 activation of ERK and PKC-δ pathways [268, 269]. All these data indicated that direct cell-cell junction, especially gap junction

played a critical role in osteogenesis. On the contrary, unlike direct cell-cell contact which was easy to modulate, signals from paracrine could hardly be controlled using existing techniques, therefore, herein we mainly focused on the exploration of direct cell-cell contact to odontoblast polarization and differentiation using our ECM-like matrix-based micropatterning technique.

In our study, the ALP activity on 450-μm^2 NF-MTs occupied by single cells were compared to that on 900-μm^2 NF-M2Ts occupied by two cells to evaluate differentiation of hDPSCs. Results showed that the ALP-positive ratio on the 2-cell microislands was almost 3 times higher than the 1-cell microislands (Fig. 27B). Similarly, the anti-Collagen I staining intensity per cell on the 2-cell NF-M2T microislands was also much higher than 1-cell NF-MTs (Fig. 27C), implying that cell-cell contact greatly promoted hDPSC differentiation. The formation of gap junction between the 2 cells on a 2-cell NF-M2T was confirmed using an anti-Connexin 43 antibody (data not shown). To examine whether gap junctions were responsible for the increased ALP activity, a gap junction inhibitor AGA was added to the culture system. Results found that with the addition of AGA, the significant difference between the 1-cell group and 2-cell group disappeared (Fig. 27B). These results showed that intercellular communication, especially the direct cell-cell contact via gap junction, played vital roles in promoting odontoblast differentiation.

As to the hDPSC polarization study, we selected again the ratio of cell with process and the average process length to examine the effect of cell-cell contact. The detection of Golgi apparatus location was omitted because of our observation that the

cytosol of the 2 cells on a NF-M2T was usually mixed and it was difficult to identify which Golgi belonged to which cell, let alone to measure the distance from the Golgi to the nucleus. Results showed that the ratio of cell with process on 2-cell NF-M2Ts was similar to that on the 1-cell NF-MTs (Fig. 26F), and the average process length between these two groups were similar (Fig. 26G), indicating that cell-cell communication didn't promote hDPSC polarization on our 3D platform. This result, which showed that direct cell-cell contact may not contribute to the polarization of odontoblast, suggested that signals from pre-ameloblast via the paracrine way might be the major force in this process, although further detailed studies are needed to verify this hypothesis.

4.4.2. Growth factors

Various types of growth factors are believed to play a role in the odontoblast maturation process, for example, previous studies have showed that 21 matrix and eight TGF-β-related genes exhibited altered expression levels during the differentiation from DPSCs to dentin-secreting odontoblasts [225, 270]. Studies that discovered the critical roles of these growth factors generally include gene-modified animal models and *in vitro* 2D culture systems, neither of which could enable an interference-free exploration of the growth factors. Now with our biomimetic single-cell platform, it's possible to explore their effects on odontoblast polarization in a much simpler system.

TGF-β superfamily members [271], including BMP-2, BMP4, BMP7, TGF-β1, and TGF-β3 [272] have been well documented as key regulatory molecules in epithelial-mesenchymal interactions during odontogenesis and dentin regeneration [273, 274]. TGF-β1 is the most abundant member of the superfamily. Previous studies have found

that TGF-β1 could be synthesized by pulp tissues in its latent form and stored in dentin matrix. Once activated by matrix metalloproteinase or some artificial biophysical methods [275], functional TGF-β1 could enhance the mRNA expression of DSPP in dental pulp cells, thus accelerate odontogenesis [276]. Exogeneous TGF-β1 protein, usually applied in combination with bioactive materials, have been reported to promote the proliferation, migration, odontoblast-like lineage differentiation and matrix secretion of dental stem cells *in vitro* and dentin regeneration in the pulp capping model *in vivo* [275, 277, 278]. However, it's noteworthy that the effect of TGF-β superfamily members are usually complicated that they don't necessarily play a positive role in cell behaviors. For example, previous studies have reported both pro- and anti-migration effects of TGF-β on endothelial cells depending on the concentration and the cell types [279]. Also, TGF-β promoted chondroblast differentiation at early stages, but inhibited osteoblast maturation at late stages [280]. In our study, it's found 50 ng/ml and 100 ng/ml TGF-β slightly enhanced hDPSC process extension while 200 ng/ml showed a negative role in promoting cell process extension. Although no significant differences were found between control group and any of the TGF-β groups, the results might propose a dual role of TGF- on hDPSC polarization, which was dependent on the concentration used. One previous study demonstrated that rat dental papilla tissues in combination with a low concentration of TGF-β (6 ng/ml) was able to induce the pulp cells to polarize on a filter [138]. However, in that experimental design, apart from TGF-β, dental papilla tissue naturally contain many growth factors and the filter provided the biophysical cues (the microchannels) at the same time, therefore, the real effect of TGF-

β remained unclear. Our study proved that the biophysical factor (3D architecture) solely could induce hDPSC polarization successfully, while addition of TGF-β in various concentrations failed to further enhance this effect, implying that the biophysical factor was indispensable in inducing hDPSC polarization and TGF-β may not play a critical role in this process.

Similarly, BMP-2 also exhibited evident and widely-documented effects in dentinogenesis and dentin regeneration in numerous studies. Moreover, its effects in promoting dentinogenesis have been proved on multiple dental cell lines, including human or rat DPSCs [281], stem cells from human exfoliated deciduous teeth (SHED) [282], stem cells of apical papilla (SCAP) [283], and odontoblast-like KN-3 cells [284] with various approaches, but its role in inducing odontoblast polarization has not been identified. In our study, we found all 3 concentrations promoted the formation of hDPSC processes and the concentration of 100 ng/ml displayed a significant effect.

BMP-4 is also a potent signal factor between mesenchymal-epithelial induced odontogenesis [285]. In one study, the addition of BMP4 to intact second-arch explants resulted in the development of organized structures containing layers of cells that expressed odontoblasts marker genes, proving that BMP-4 was capable of stimulating organized differentiation of dental-specific cells from non-dental primordia [286]. Another study found the injection of anti-BMP-4 antibody in pregnant mice blocked normal odontoblast differentiation and dentin formation [287]. These studies together confirmed the critical role of BMP-4 in primary odontogenesis and dentinogenesis. Apart from that, BMP-4 possesses odontogenesis-promoting effects in a number of *in*

vitro studies [288-290], although its effect was less pronounced when compared to BMP-2. Our results found that, similar to BMP-2, all 3 concentrations of BMP-4 accelerated the hDPSC polarization and a concentration of 200 ng/ml displayed a significant effect. Together with our data of TGF-β and BMP-2, it indicated that TGF-β superfamily members generally possessed a favorable effect to odontoblast polarization, but their effects depended on the concentration they were used. Moreover, in regards to inducing odontoblast polarization, BMP-2 seemed more potent than BMP-4.

Molecules of the FGF family such as FGF-2, FGF-3, FGF-4, FGF-8 and FGF-10 are involved in cell proliferation and regulate expression of specific target genes in teeth [291-293]. Among those factors, FGF-2 stimulates proliferation in dental mesenchyme during the bud and cap stage of tooth germ development and therefore plays an important role in odontogenesis. It's believed that FGF-2 played a greater role in differentiation than in proliferation since it was observed in higher concentrations during the cap to bell stage and during dentin deposition in odontoblasts [294]. A variety of studies have demonstrated the effective role of FGF-2 in post-injury dentin repairment in combination with various types of biomaterials [288, 295-299]. Our results showed that FGF-2 exhibited strong promoting effects on hDPSC polarization process in all 3 concentration tested, which indicated that FGF-2 could be a potent regulator of odontoblast polarization *in vivo*.

EGF is a protein that is critically associated with rapid tissue regeneration after injuries. Previous reports demonstrated that EGF was beneficial for the regeneration of multiple tissue types, such as skin [300], liver [301], kidney [302] and bone regeneration

[303, 304]. Its potent capability in tissue regeneration is closely related to its effect in promoting DNA synthesis and cell proliferation, cell migration, colony forming [305] and most important of all, angiogenesis [306, 307], which remains a challenging part in the regeneration of most tissues. Although its effect in dentin regeneration hasn't be reported, EGF has been proposed to be involved in tooth initiation and morphogenesis using immunolocalization and/or in situ hybridizations approaches [1]. The effect of EGF, according to our data, was not evident even though slight enhancing effects were observed. This indicated that instead of directly inducing odontoblast polarization, EGF is more likely to participate in this process indirectly, maybe by promoting dental mesenchymal division or accelerating blood vessel generation underneath the odontoblast layer to ensure nutrient supply, which requires massive further studies.

HGF is a type of growth factor mainly derived from mesenchyme and it participates in the regulation of a broad range of physiological processes, including mineralized tissue formation under pathological conditions. Expression of HGF and its downstream factor c-Met have been localized in developing dental epithelia and mesenchyme, implicating its potential role in tooth development [308-310]. Previous reports have proved that HGF could be sequestrated in dentin matrix [311] and either released or exogeneous HGF protein could promote the chemoattraction, proliferation, differentiation and subsequently the mineralization of dental pulp cells *in vitro* [311, 312]. Our result indicated HGF was also a potent regulator of odontoblast polarization that all 3 concentrations tested greatly enhanced the formation of hDPSC processes.

Wnt-family proteins including Wnt3, Wnt5a, Wnt-7b, Wnt-10a and Wnt-10b have critical roles in regulating cell proliferation, migration and differentiation during tooth initiation and morphogenesis [313-315]. However, Among all the Wnt genes that are differentially expressed during tooth development, only Wnt5a is localized in the mesenchyme and dental papilla [316]. Previous studies found that Wnt5a regulated odontoblast growth, patterning, and differentiation during odontogenesis by modulating both non-canonical and canonical Wnt/β-catenin signaling [135, 317]. Exogenous Wnt5a promoted cell apoptosis in non-dental regions, while acted as a regulator of other genes that rescued tooth germs from cell death in the dental region, thus it played a critical role in controlling the tooth size during development [316]. Moreover, in ex vivo studies, Wnt5a overexpression was proved to inhibit the proliferation and migration of human dental papilla cells [318], but in the meantime, promoted their differentiation and mineralization activities [319]. In our study, all 3 concentrations of Wnt5a were found to greatly increase the formation of hDPSC cellular process, indicating Wnt5a was also a powerful factor that could induce hDPSC polarization *in vitro*.

Shh is a signaling protein mainly expressed in dental epithelium that also contributes to the initiation of odontogenesis and dental morphogenesis in primary tooth development [320]. Moreover, dental mesenchymal cells express Gli1, a downstream transcription factor of Shh signaling pathway, and Ptch1 and Smo, the surface receptors of Shh. Therefore, the Shh signaling network is delicately regulated between dental mesenchymal layer and dental epithelial layer. Apart from that, many other signaling pathways or critical transcription factors may also participate in the regulatory role of

Shh, like the BMP2/4 pathway [321], FGF pathway [322], Wnt/β-catenin pathway [323] and Runx2 [324], which indicates Shh could be a potent regulator in odontoblast differentiation. Shh also preserves the stem cell population in dental pulp [325, 326], especially the Gli1-positive cells that have been shown to possess multilineage differentiation potential, high colony-forming activity [327] and even tooth injury reparation ability [326]. Even though the regulatory role of Shh has been widely acknowledged, there are few researchers using it in regenerative studies. One study found that transfection of Shh via adenovirus in hDPCs displayed increased expression of odontogenic markers *in vitro*, and when the transfected cells were implanted *in vivo* in combination with a porous calcium phosphate cement scaffold, dentin-like mineralized tissues were generated [328]. Our results found that direct application of Shh protein could significantly promote hDPSC polarization *in vitro*, providing a hint that may encourage the future use of this protein in dentin regeneration studies.

Moreover, it's clearly shown that each growth factor had a concentration range and only within the range, the promoting effect on hDPSC polarization on the NF-MT microislands could be observed (Fig. 29). However, when a concentration higher than the threshold was applied, single hDPSCs managed to break the cell-limiting effect of the micropatterns (Fig. 30A). Based on this phenomenon, a non-patterned non-drilled nanofibrous matrix was used as culture substrate and Shh of various concentrations were added to the culture system to examine whether those high concentration of growth factors alone could promote hDPSC polarization. Results showed no significant difference between the control group and the 4 Shh groups, indicating that the growth

factors alone failed to induce hDPSC polarization *in vitro*. Therefore, the 3D micropatterning structure was essential for hDPSC polarization *in vitro*, and the addition of growth factors played a supplementary role in this process.

4.4.3. Cell type

As mentioned in the Introduction Chapter, one big challenge in regenerative dentistry is that the end product of various dentin regeneration strategies is always osteodentin. Lacking the polarized odontoblasts and the tubular structure, the functions of those regenerated tissues are usually far from satisfactory. Therefore, the regeneration of tubular dentin and the induced polarization of odontoblasts seems unachievable to researchers for many years until in the most recent decade, studies from several research groups including our group [138, 143, 144, 174, 329] successfully induced odontoblast to polarize and regenerated dentin-like tissues on dentin surface [143, 144], Millipore filters [138] or artificial tubular gelatin matrices [139] in both *in vitro* and *in vivo* studies. To be noted, in all these studies, only dental tissues including DPSCs, tooth germs or dental pulp tissues were used. However, a research group [259] managed to achieve similar results using non-dental cells including human BMSCs and connective tissue cell line C3H10T1/2 with the addition of a preameloblast-derived protein Cpne7, indicating that dental cells were not the only source for dentin regeneration and non-dental cells or tissues could also be induced to polarize into odontoblasts with specific inductions. This study provided us with new insights and made us wonder whether BMSCs could also be polarize into odontoblasts on our scaffold and function like dental cells.

We examined the morphology of single rBMSCs on the NF-MT microislands using confocal microscopy and SEM. Images from both approaches showed that identical to hDPSCs, single rBMSCs displayed a odontoblast-like polarized morphology (Fig. 31 A-H). Besides, the ratio of cell with processes (Fig. 31I) and the average cellular process length (Fig. 31J) of rBMSCs were similar to the hDPSCs at any timepoint. Moreover, the translocation of Golgi apparatus within the cytosol of rBMSCs also displayed a similar pattern to that of hDPSCs (Fig. 31 J&K). All these morphological data informed us that rBMSCs could be induced to polarize in the same pattern as hDPSCs on our 3D tubular platform.

In the meantime, the differentiation behaviors of rBMSCs and hDPSCs on the NF-MT scaffolds were examined and compared. Quantitative data of ALP staining indicated that rBMSCs possessed significantly higher osteo/odontogenic potential than hDPSCs (Fig. 31L). Similar results were also seen when both types of cells were seeded on NF-MPs (Fig. 31L). While ALP protein could be synthesized and expressed naturally by both rBMSCs and hDPSCs, we purposely selected another assay to further examine the odontogenic potential of rBMSCs, the anti-DSP immunofluorescent staining. Although traditionally DSPP and/or its cleaved products DSP and DPP were believed to be tooth specific, studies from recent two decades had demonstrated its expression in non-dental tissues like bone [330], cementum [331] and some non-mineralized tissues, although the expression intensity of these markers in non-dental tissues was reported to be lower than that in dentin. In our assay, we clearly observed the expression of DSP proteins within the polarized rBMSCs, although the intensity was not comparable to

hDPSCs (Fig. 31 D&H). Therefore, it's indicated that rBMSCs could be polarized into a odontoblast-like morphology on the 3D tubular scaffold, but their differentiation behaviors were distinct from the hDPSCs. Still, these results hinted us that BMSCs could be utilized as an alternative cell resource for dentin regeneration with the help of some external stimuli.

4.4.4. Inhibitors

Previous reports have confirmed that the differentiation of odontoblasts and its secretion of pre-dentin components require the integrity of the cytoskeleton system, which interact with cytosol and plasma membrane [332] proteins to function as the basic units forming the cellular processes [210, 333]. Moreover, cytoskeletal elements have been documented to concentrate on the apical pole (process pole) of odontoblasts and are likely to functionally participate in the secretory activity of a mature odontoblast. However, the role of this cytoskeletal network in odontoblast polarization remains unclear. Taking advantage of our novel 3D tubular micropatterning technique, this question could be discussed slightly.

Inhibitors targeting the assembly and reorganization of microfilaments and microtubules were added to the hDPSCs' culture environment, separately. Results indicated that the microfilament dynamics played an indispensable role in supporting cell adhesion and subsequent cell polarization, since the addition of its inhibitor dramatically destroyed cell attachment (Fig. 32A), and when further observation was made to the few cells that survived, no discernable cell processes could be found (Fig. 32 B&C). Microtubule played a less critical role in supporting cell attachment, but it's

indispensable for cellular process formation during hDPSC polarization. Results showed that the microtubule assembly inhibitor significantly impacted cell adhesion (Fig. 32A), cellular process formation (Fig. 32 B&C), and Golgi apparatus translocation (Fig. 32D), although its effects were less severe than the inhibitor of microfilaments. Intermediate filaments, unlike microfilaments or microtubules, are more stable in nature and their components are more complex, as a result, there is no well-documented inhibitor available to inhibit their assembly and their effect in inducing hDPSC polarization cannot be studied likewise.

RhoA/ROCK signaling pathway has been well demonstrated to regulate the organization and distribution of cytoskeletal elements and modulate intracellular tension. Moreover, it's the main regulator in various cytological activities that require cellular reshaping and movement, such as cell migration and cell polarity [334]. In previous chapter, we had proved the vital role of RhoA/ROCK signaling pathway in regulating hDPSC differentiation, thus here we examined its role in hDPSC polarization. The addition of Y-27632 didn't influence cell adhesion as shown by the cell attachment ratio (Fig. 32A), but it greatly hindered the hDPSC polarization process that a significantly smaller amount of cellular processes were formed (Fig. 32B) and their average length was decreased (Fig. 32C&E). The movement of Golgi apparatus could still be observed on a NF-MT microisland, but it stopped at a juxtanuclear position after 3 days' culture (Fig. 32E), indicating the cell was not fully polarized. These results showed that the RhoA/ROCK signaling pathway had minimal influence to hDPSC adhesion on the gelatin nanofibers but it played an important role in inducing hDPSC polarization.

Integrin families are a group of transmembrane proteins that mediate in cell-matrix interactions. They function not only as scaffolding protein that connect cytoskeleton elements to extracellular components, but also as sensors that sense external stimuli and regulators that modify cellular responses [335]. Integrin has two subunits, alpha and beta, and its normal function requires the specific binding of both subunits. In previous chapters, we had identified that integrin β1 proteins participated in the hDPSC-gelatin nanofiber interaction and its distribution differed on different surface topographies (data not shown), suggesting that integrin-mediated cell adhesion could influence hDPSC differentiation behaviors. To examine its role in hDPSC polarization, a high concentration of anti-integrin β1 antibody was added to the culture system to block integrin β1-mediated cell adhesion. Results showed that the anti-integrin β1 antibody exhibited a similar effect to nocodazole that cell adhesion (Fig. 32A), process formation (Fig. 32 B&C) and Golgi translocation (Fig. 32F) were all significantly impaired compared to the control group. This result indicated that integrin β1-mediated cell adhesion was also a prerequisite for hDPSC polarization *in vitro*. However, it's noteworthy that even though a high concentration of anti-integrin β1 antibody was used in our study, there were still quite a number of cells managed to attach on the nanofibers, indicating that integrin β1 proteins were not the only adhesion mediators of hDPSCs. This was consistent with a previous study which showed that apart from the β1 subtype, various integrin alpha-beta heterodimers were expressed on the odontoblast surface [226].

In summary, in this chapter, we further utilized the 3D tubular NF-MT scaffold as a platform to examine how various biochemical factors regulate single cell polarization *in vitro*, which include intercellular communication, growth factors, cell type and various inhibitors. Our results showed that intercellular communication promoted hDPSC differentiation but didn't influence hDPSC polarization. Various types of growth factors enhanced single hDPSC polarization, and their effects were concentration-dependent. Besides, rat BMSCs displayed a polarized morphology similar to hDPSCs on the NF-MTs, but the differentiation abilities of these 2 types of cells were distinct. Lastly, we confirmed that the cytoskeletal integrity and integrin-mediated cell adhesion were both prerequisites for hDPSC polarization *in vitro*.

5. CONCLUSIONS

To date, the regeneration of tubular dentin remains challenging in dental clinic and in dental regeneration studies. Displaying a bone-like structure, the regenerated dentin tissues are deprived of the neural sensation ability and appropriate mechanical strengths. In order to achieve functional tubular dentin regeneration, it's important to figure out the critical factors that could potently induce odontoblast polarization and differentiation and apply them in future scaffold designs. However, currently the knowledge regarding to odontoblast polarization and differentiation is scarce, which greatly impedes the development of regenerative dentistry.

Previous studies had demonstrated that both biochemical and biophysical factors participated in the odontoblast polarization and differentiation process, but what types of factors and how exactly do they regulate odontoblast behaviors remains unclear. Therefore, a platform that enables the exploration of both biochemical and biophysical factors seems advantageous for the odontoblast study.

Here we generated a biomimetic 3D scaffold for *in vitro* single cell observation by combining the electrospinning, photolithography and laser ablation techniques. This scaffold managed to recapitulate the hierarchical structures of natural dentin ECM and successfully induced single hDPSC to polarize into a odontoblast-like morphology. Moreover, this scaffold possessed controllable versality. Therefore, it could be utilized as a clean platform for us to identify various biochemical or biophysical factors that regulated odontoblast polarization and differentiation behaviors *in vitro*.

Micropatterns with different physical parameters were fabricated to explore the influence of various biophysical factors on hDPSC behaviors. Firstly, micropattern morphology was found to be a regulatory factor in hDPSC adhesion, morphology and differentiation. Then the comparison of micropatterns constructed on a nanofibrous substrate and a smooth substrate showed that the nanofibrous topography promoted a more *in vivo*-like cell morphology, less focal adhesion and stronger differentiation ability, which was regulated by the RhoA/ROCK/YAP1 signaling pathway. However, hDPSC polarization was not observed on any of the 2D substrates. Thus, a 3D tubular architecture was introduced into the micropatterning design. This spatial architecture induced single hDPSC polarization by promoting the formation of cellular process and translocation of the Golgi apparatus. It also accelerated the differentiation of single hDPSCs. Lastly, the influence of gravity was examined using the NF-MT platform and it turned out to be a contributory factor of odontoblast polarization and differentiation.

Afterwards, the NF-MT microislands were utilized to examine the role of several biochemical factors on hDPSC polarization and differentiation behaviors. Intercellular communication was found an advantageous factor to hDPSC differentiation, but it displayed minimal effects on single hDPSC polarization. Eight types of growth factors were tested on the NF-MT platform and most of them exhibited a promoting effect on hDPSC polarization, and these effects were concentration-dependent. Moreover, it's found that growth factors alone failed to induce hDPSC polarization *in vitro* and the tubular micropatterning structure was indispensable in this process. Then rat BMSCs were seeded on the NF-MT platform in the same way to hDPSCs to examine the

influence of cell type. Results showed that rBMSCs displayed similar polarization behaviors to hDPSCs, but their differentiation abilities were distinct to those of hDPSCs. Lastly, several cellular inhibitors were added to the NF-MT platform and it's found that both cytoskeletal integrity and integrin β1-mediated cell adhesion were prerequisites for hDPSC polarization.

Therefore, using the nanofibrous micropattern as a platform, we have identified multiple biophysical and biochemical factors that could promote *in vitro* hDPSC polarization and differentiation. Those factors will provide a hint for the design of next-generation scaffolds and benefit future tubular dentin regeneration studies.

REFERENCES

1. Ruch, J., H. Lesot, and C. Begue-Kirn, *Odontoblast differentiation.* The International journal of developmental biology, 1995. 39(1): p. 51-68.
2. Li, C., et al., *Dentinal mineralization is not limited in the mineralization front but occurs along with the entire odontoblast process.* International journal of biological sciences, 2018. 14(7): p. 693.
3. Linde, A. and M. Goldberg, *Dentinogenesis.* Critical Reviews in Oral Biology & Medicine, 1993. 4(5): p. 679-728.
4. Diekwisch, T., *Localization of microfilaments and microtubules during dental development in the rat.* Acta histochemica. Supplementband, 1989. 37: p. 209-212.
5. Magloire, H., et al., *Odontoblast: a mechano‐sensory cell.* Journal of Experimental Zoology Part B: Molecular and Developmental Evolution, 2009. 312(5): p. 416-424.
6. LESOT, H., et al., *Immunofluorescent localization of vimentin, prekeratin and actin during odontoblast and ameloblast differentiation.* Differentiation, 1982. 21(1-3): p. 133-137.
7. McGuire, J.D., et al., *Enamel organic matrix: potential structural role in enamel and relationship to residual basement membrane constituents at the dentin enamel junction.* Connective tissue research, 2014. 55(sup1): p. 33-37.
8. Román‐Fernández, A. and D.M. Bryant, *Complex polarity: building multicellular tissues through apical membrane traffic.* Traffic, 2016. 17(12): p.

1244-1261.

9. Tjäderhane, L., et al., *Polarity of mature human odontoblasts.* Journal of dental research, 2013. 92(11): p. 1011-1016.

10. Miyoshi, J. and Y. Takai, *Structural and functional associations of apical junctions with cytoskeleton.* Biochimica et Biophysica Acta (BBA)-Biomembranes, 2008. 1778(3): p. 670-691.

11. Moritz, M. and D.A. Agard, *γ-Tubulin complexes and microtubule nucleation.* Current opinion in structural biology, 2001. 11(2): p. 174-181.

12. Wiese, C. and Y. Zheng, *A new function for the γ-tubulin ring complex as a microtubule minus-end cap.* Nature Cell Biology, 2000. 2(6): p. 358-364.

13. Li, R. and G.G. Gundersen, *Beyond polymer polarity: how the cytoskeleton builds a polarized cell.* Nature reviews Molecular cell biology, 2008. 9(11): p. 860.

14. Feldman, J.L. and J.R. Priess, *A role for the centrosome and PAR-3 in the hand-off of MTOC function during epithelial polarization.* Current Biology, 2012. 22(7): p. 575-582.

15. Sugioka, K. and H. Sawa, *Formation and functions of asymmetric microtubule organization in polarized cells.* Current opinion in cell biology, 2012. 24(4): p. 517-525.

16. Oriolo, A.S., et al., *Intermediate filaments: a role in epithelial polarity.* Experimental cell research, 2007. 313(10): p. 2255-2264.

17. Franke, W., et al., *The organization of cytokeratin filaments in the intestinal epithelium.* European journal of cell biology, 1979. 19(3): p. 255.

18. Fontao, L., et al., *Polarized expression of HD1: relationship with the cytoskeleton in cultured human colonic carcinoma cells.* Experimental cell research, 1997. 231(2): p. 319-327.

19. Windoffer, R., et al., *Focal adhesions are hotspots for keratin filament precursor formation.* The Journal of cell biology, 2006. 173(3): p. 341-348.

20. Deacon, S.W., et al., *Dynactin is required for bidirectional organelle transport.* J Cell Biol, 2003. 160(3): p. 297-301.

21. Müsch, A., *Microtubule organization and function in epithelial cells.* Traffic, 2004. 5(1): p. 1-9.

22. Apodaca, G., *Endocytic traffic in polarized epithelial cells: role of the actin and microtubule cytoskeleton.* Traffic, 2001. 2(3): p. 149-159.

23. Spiliotis, E.T., et al., *Epithelial polarity requires septin coupling of vesicle transport to polyglutamylated microtubules.* The Journal of cell biology, 2008. 180(2): p. 295-303.

24. Kodama, A., et al., *ACF7: an essential integrator of microtubule dynamics.* Cell, 2003. 115(3): p. 343-354.

25. Wu, X.S., G.L. Tsan, and J.A. Hammer, *Melanophilin and myosin Va track the microtubule plus end on EB1.* J Cell Biol, 2005. 171(2): p. 201-207.

26. Martin, S.G., et al., *Tea4p links microtubule plus ends with the formin for3p in the establishment of cell polarity.* Developmental cell, 2005. 8(4): p. 479-491.

27. Kaverina, I., K. Rottner, and J.V. Small, *Targeting, capture, and stabilization of microtubules at early focal adhesions.* The Journal of cell biology, 1998. 142(1):

p. 181-190.

28. Krendel, M., F.T. Zenke, and G.M. Bokoch, *Nucleotide exchange factor GEF-H1 mediates cross-talk between microtubules and the actin cytoskeleton.* Nature cell biology, 2002. 4(4): p. 294-301.

29. Chang, L. and R.D. Goldman, *Intermediate filaments mediate cytoskeletal crosstalk.* Nature reviews Molecular cell biology, 2004. 5(8): p. 601-613.

30. Elric, J. and S. Etienne-Manneville, *Centrosome positioning in polarized cells: common themes and variations.* Experimental cell research, 2014. 328(2): p. 240-248.

31. Roux, K.J., et al., *Nesprin 4 is an outer nuclear membrane protein that can induce kinesin-mediated cell polarization.* Proceedings of the National Academy of Sciences, 2009. 106(7): p. 2194-2199.

32. Razafsky, D. and D. Hodzic, *Bringing KASH under the SUN: the many faces of nucleo-cytoskeletal connections.* The Journal of cell biology, 2009. 186(4): p. 461-472.

33. Starr, D.A. and M. Han, *ANChors away: an actin based mechanism of nuclear positioning.* Journal of cell science, 2003. 116(2): p. 211-216.

34. Huelsmann, S. and N.H. Brown, *Nuclear positioning by actin cables and perinuclear actin: Special and general?* Nucleus, 2014. 5(3): p. 219-223.

35. Gomes, E.R., S. Jani, and G.G. Gundersen, *Nuclear movement regulated by Cdc42, MRCK, myosin, and actin flow establishes MTOC polarization in migrating cells.* Cell, 2005. 121(3): p. 451-463.

36. Dupin, I., E. Camand, and S. Etienne-Manneville, *Classical cadherins control nucleus and centrosome position and cell polarity.* The Journal of cell biology, 2009. 185(5): p. 779-786.

37. Dupin, I., Y. Sakamoto, and S. Etienne-Manneville, *Cytoplasmic intermediate filaments mediate actin-driven positioning of the nucleus.* J Cell Sci, 2011. 124(6): p. 865-872.

38. Dupin, I. and S. Etienne-Manneville, *Nuclear positioning: mechanisms and functions.* The international journal of biochemistry & cell biology, 2011. 43(12): p. 1698-1707.

39. Piel, M., et al., *The respective contributions of the mother and daughter centrioles to centrosome activity and behavior in vertebrate cells.* The Journal of cell biology, 2000. 149(2): p. 317-330.

40. Gonçalves, J., et al., *TBCCD1, a new centrosomal protein, is required for centrosome and Golgi apparatus positioning.* EMBO reports, 2010. 11(3): p. 194-200.

41. Matsumoto, T., et al., *Ninein is expressed in the cytoplasm of angiogenic tip-cells and regulates tubular morphogenesis of endothelial cells.* Arteriosclerosis, thrombosis, and vascular biology, 2008. 28(12): p. 2123-2130.

42. Sütterlin, C. and A. Colanzi, *The Golgi and the centrosome: building a functional partnership.* The Journal of cell biology, 2010. 188(5): p. 621-628.

43. Zhu, X. and I. Kaverina, *Golgi as an MTOC: making microtubules for its own good.* Histochemistry and cell biology, 2013. 140(3): p. 361-367.

44. Sanders, A.A. and I. Kaverina, *Nucleation and dynamics of Golgi-derived microtubules.* Frontiers in neuroscience, 2015. 9.

45. Efimov, A., et al., *Asymmetric CLASP-dependent nucleation of noncentrosomal microtubules at the trans-Golgi network.* Developmental cell, 2007. 12(6): p. 917-930.

46. Ori-McKenney, K.M., L.Y. Jan, and Y.-N. Jan, *Golgi outposts shape dendrite morphology by functioning as sites of acentrosomal microtubule nucleation in neurons.* Neuron, 2012. 76(5): p. 921-930.

47. Rivero, S., et al., *Microtubule nucleation at the cis‐side of the Golgi apparatus requires AKAP450 and GM130.* The EMBO journal, 2009. 28(8): p. 1016-1028.

48. Vicente-Manzanares, M., et al., *Regulation of protrusion, adhesion dynamics, and polarity by myosins IIA and IIB in migrating cells.* The Journal of cell biology, 2007. 176(5): p. 573-580.

49. Gurel, P.S., A.L. Hatch, and H.N. Higgs, *Connecting the cytoskeleton to the endoplasmic reticulum and Golgi.* Current biology, 2014. 24(14): p. R660-R672.

50. Giepmans, B.N. and S.C. van IJzendoorn, *Epithelial cell–cell junctions and plasma membrane domains.* Biochimica et Biophysica Acta (BBA)-Biomembranes, 2009. 1788(4): p. 820-831.

51. Zihni, C., et al., *Tight junctions: from simple barriers to multifunctional molecular gates.* Nature Reviews Molecular Cell Biology, 2016.

52. Günzel, D. and S. Alan, *Claudins and the modulation of tight junction permeability.* Physiological reviews, 2013. 93(2): p. 525-569.

53. Balda, M.S. and K. Matter, *Tight junctions as regulators of tissue remodelling.* Current opinion in cell biology, 2016. 42: p. 94-101.

54. Caplan, M.J., P. Seo-Mayer, and L. Zhang, *Molecular cell biology and physiology of solute transport: Epithelial junctions and polarity: complexes and kinases.* Current opinion in nephrology and hypertension, 2008. 17(5): p. 506.

55. Shin, K., V.C. Fogg, and B. Margolis, *Tight junctions and cell polarity.* Annu. Rev. Cell Dev. Biol., 2006. 22: p. 207-235.

56. Fanning, A.S. and J.M. Anderson, *Zonula occludens‐1 and‐2 are cytosolic scaffolds that regulate the assembly of cellular junctions.* Annals of the New York Academy of Sciences, 2009. 1165(1): p. 113-120.

57. Heymann, R., et al., *E-and N-cadherin distribution in developing and functional human teeth under normal and pathological conditions.* The American journal of pathology, 2002. 160(6): p. 2123-2133.

58. Sasaki, T. and P.R. Garant, *Structure and organization of odontoblasts.* The Anatomical Record, 1996. 245(2): p. 235-249.

59. Arana-Chavez, V. and E. Katchburian, *Development of tight junctions between odontoblasts in early dentinogenesis as revealed by freeze-fracture.* The Anatomical Record, 1997. 248(3): p. 332-338.

60. Callé, A., *Intercellular junctions between human odontoblasts.* Cells Tissues Organs, 1985. 122(3): p. 138-144.

61. Iguchi, Y., et al., *Intercellular junctions in odontoblasts of the rat incisor studied with freeze-fracture.* Archives of oral biology, 1984. 29(7): p. 487-497.

62. Bishop, M., *Evidence for tight junctions between odontoblasts in the rat incisor.* Cell and tissue research, 1985. 239(1): p. 137-140.

63. Arana‐Chavez, V.E. and E. Katchburian, *Freeze‐fracture studies of the distal plasma membrane of rat odontoblasts during their differentiation and polarisation.* European journal of oral sciences, 1998. 106(S1): p. 132-136.

64. João, S. and V.E. Arana‐Chavez, *Tight junctions in differentiating ameloblasts and odontoblasts differentially express ZO‐1, occludin, and claudin‐1 in early odontogenesis of rat molars.* The Anatomical Record Part A: Discoveries in Molecular, Cellular, and Evolutionary Biology, 2004. 277(2): p. 338-343.

65. Hoshino, M., et al., *Claudin rather than occludin is essential for differentiation in rat incisor odontoblasts.* Oral diseases, 2008. 14(7): p. 606-612.

66. Xu, J., et al., *Novel role of zonula occludens‐1: A tight junction protein closely associated with the odontoblast differentiation of human dental pulp cells.* Cell biology international, 2016. 40(7): p. 787-795.

67. Heymann, R., *Cell adhesion molecules during odontogenesis and tooth-related diseases*. 2002: Institutionen för cell-och molekylärbiologi (CMB)/Department of Cell and Molecular Biology.

68. Lee, H.-K., et al., *Nuclear factor IC (NFIC) regulates dentin sialophosphoprotein (DSPP) and E-cadherin via control of Kruppel-like factor 4 (KLF4) during dentinogenesis.* Journal of Biological Chemistry, 2014: p. jbc. M114. 568691.

69. Assémat, E., et al., *Polarity complex proteins.* Biochimica et Biophysica Acta (BBA)-Biomembranes, 2008. 1778(3): p. 614-630.

70. Ebnet, K., *Cell Polarity 1: Biological Role and Basic Mechanisms*. 2015: Springer.

71. Cereijido, M., et al., *Tight junction and polarity interaction in the transporting epithelial phenotype.* Biochimica et Biophysica Acta (BBA)-Biomembranes, 2008. 1778(3): p. 770-793.

72. Chen, J. and M. Zhang, *The Par3/Par6/aPKC complex and epithelial cell polarity.* Experimental cell research, 2013. 319(10): p. 1357-1364.

73. Suzuki, A. and S. Ohno, *The PAR-aPKC system: lessons in polarity.* Journal of cell science, 2006. 119(6): p. 979-987.

74. Kishikawa, M., A. Suzuki, and S. Ohno, *aPKC enables development of zonula adherens by antagonizing centripetal contraction of the circumferential actomyosin cables.* Journal of cell science, 2008. 121(15): p. 2481-2492.

75. Hong, Y., *aPKC: the Kinase that Phosphorylates Cell Polarity.* F1000Research, 2018. 7.

76. Michel, D., et al., *PATJ connects and stabilizes apical and lateral components of tight junctions in human intestinal cells.* Journal of cell science, 2005. 118(17): p. 4049-4057.

77. Bulgakova, N.A. and E. Knust, *The Crumbs complex: from epithelial-cell polarity to retinal degeneration.* Journal of cell science, 2009. 122(15): p. 2587-2596.

78. Fogg, V.C., C.-J. Liu, and B. Margolis, *Multiple regions of Crumbs3 are required for tight junction formation in MCF10A cells.* Journal of cell science, 2005. 118(13): p. 2859-2869.

79. Qin, Y., et al., *The mammalian Scribble polarity protein regulates epithelial cell*

adhesion and migration through E-cadherin. The Journal of cell biology, 2005. 171(6): p. 1061-1071.

80. Iizuka-Kogo, A., et al., *Abnormal development of urogenital organs in Dlgh1-deficient mice.* Development, 2007. 134(9): p. 1799-1807.

81. Inai, T., et al., *Differential expression of the tight junction proteins, claudin‐1, claudin‐4, occludin, ZO‐1, and PAR3, in the ameloblasts of rat upper incisors.* The Anatomical Record: Advances in Integrative Anatomy and Evolutionary Biology, 2008. 291(5): p. 577-585.

82. Wu, C.-F. and D.J. Lew, *Beyond symmetry-breaking: competition and negative feedback in GTPase regulation.* Trends in cell biology, 2013. 23(10): p. 476-483.

83. Iden, S. and J.G. Collard, *Crosstalk between small GTPases and polarity proteins in cell polarization.* Nature reviews Molecular cell biology, 2008. 9(11): p. 846-859.

84. Ngok, S.P., W.-H. Lin, and P.Z. Anastasiadis, *Establishment of epithelial polarity–GEF who's minding the GAP?* J Cell Sci, 2014. 127(15): p. 3205-3215.

85. Mack, N.A. and M. Georgiou, *The interdependence of the Rho GTPases and apicobasal cell polarity.* Small GTPases, 2014. 5(2): p. e973768.

86. Spiering, D. and L. Hodgson, *Dynamics of the Rho-family small GTPases in actin regulation and motility.* Cell adhesion & migration, 2011. 5(2): p. 170-180.

87. Sit, S.-T. and E. Manser, *Rho GTPases and their role in organizing the actin cytoskeleton.* J Cell Sci, 2011. 124(5): p. 679-683.

88. Hall, A., *Rho GTPases and the actin cytoskeleton.* Science, 1998. 279(5350): p.

509-514.

89. Watanabe, T., J. Noritake, and K. Kaibuchi, *Regulation of microtubules in cell migration.* Trends in cell biology, 2005. 15(2): p. 76-83.

90. Wojnacki, J., et al., *Rho GTPases at the crossroad of signaling networks in mammals: impact of Rho-GTPases on microtubule organization and dynamics.* Small GTPases, 2014. 5(1): p. e28430.

91. Quinones, G.B., et al., *The posttranslational modification of tubulin undergoes a switch from detyrosination to acetylation as epithelial cells become polarized.* Molecular Biology of the Cell, 2011. 22(7): p. 1045-1057.

92. Kaverina, I., O. Krylyshkina, and J.V. Small, *Regulation of substrate adhesion dynamics during cell motility.* The international journal of biochemistry & cell biology, 2002. 34(7): p. 746-761.

93. Birkenfeld, J., et al., *Cellular functions of GEF-H1, a microtubule-regulated Rho-GEF: is altered GEF-H1 activity a crucial determinant of disease pathogenesis?* Trends in cell biology, 2008. 18(5): p. 210-219.

94. Farhan, H. and V.W. Hsu, *Cdc42 and cellular polarity: emerging roles at the Golgi.* Trends in cell biology, 2016. 26(4): p. 241-248.

95. Long, M. and J.C. Simpson, *Rho GTPases operating at the Golgi complex: Implications for membrane traffic and cancer biology.* Tissue and Cell, 2017. 49(2): p. 163-169.

96. Zilberman, Y., et al., *Involvement of the Rho–mDia1 pathway in the regulation of Golgi complex architecture and dynamics.* Molecular biology of the cell, 2011.

22(16): p. 2900-2911.

97. Braun, A.C., et al., *The Rho-specific GAP protein DLC3 coordinates endocytic membrane trafficking.* J Cell Sci, 2015. 128(7): p. 1386-1399.

98. Chen, X. and I.G. Macara, *Par-3 controls tight junction assembly through the Rac exchange factor Tiam1.* Nature cell biology, 2005. 7(3): p. 262-269.

99. Yagi, S., M. Matsuda, and E. Kiyokawa, *Chimaerin suppresses Rac1 activation at the apical membrane to maintain the cyst structure.* PLoS one, 2012. 7(12): p. e52258.

100. Bryant, D.M., et al., *A molecular network for de novo generation of the apical surface and lumen.* Nature cell biology, 2010. 12(11): p. 1035-1045.

101. Schlüter, M.A., et al., *Trafficking of Crumbs3 during cytokinesis is crucial for lumen formation.* Molecular biology of the cell, 2009. 20(22): p. 4652-4663.

102. Zihni, C., M.S. Balda, and K. Matter, *Signalling at tight junctions during epithelial differentiation and microbial pathogenesis.* J Cell Sci, 2014. 127(16): p. 3401-3413.

103. Ehrlich, J.S., M.D. Hansen, and W.J. Nelson, *Spatio-temporal regulation of Rac1 localization and lamellipodia dynamics during epithelial cell-cell adhesion.* Developmental cell, 2002. 3(2): p. 259-270.

104. Yamada, S. and W.J. Nelson, *Localized zones of Rho and Rac activities drive initiation and expansion of epithelial cell–cell adhesion.* The Journal of cell biology, 2007. 178(3): p. 517-527.

105. Quiros, M. and A. Nusrat. *RhoGTPases, actomyosin signaling and regulation of*

the epithelial Apical Junctional Complex. in *Seminars in cell & developmental biology*. 2014. Elsevier.

106. Terry, S.J., et al., *Spatially restricted activation of RhoA signalling at epithelial junctions by p114RhoGEF drives junction formation and morphogenesis.* Nature cell biology, 2011. 13(2): p. 159-166.

107. Itoh, M., et al., *Rho GTP exchange factor ARHGEF11 regulates the integrity of epithelial junctions by connecting ZO-1 and RhoA-myosin II signaling.* Proceedings of the National Academy of Sciences, 2012. 109(25): p. 9905-9910.

108. Nakajima, H. and T. Tanoue, *Lulu2 regulates the circumferential actomyosin tensile system in epithelial cells through p114RhoGEF.* J Cell Biol, 2011. 195(2): p. 245-261.

109. Samarin, S.N., et al., *Rho/Rho-associated kinase-II signaling mediates disassembly of epithelial apical junctions.* Molecular biology of the cell, 2007. 18(9): p. 3429-3439.

110. Aijaz, S., et al., *Binding of GEF-H1 to the tight junction-associated adaptor cingulin results in inhibition of Rho signaling and G1/S phase transition.* Developmental cell, 2005. 8(5): p. 777-786.

111. Zihni, C., et al., *Dbl3 drives Cdc42 signaling at the apical margin to regulate junction position and apical differentiation.* J Cell Biol, 2014. 204(1): p. 111-127.

112. Liu, X.F., S. Ohno, and T. Miki, *Nucleotide exchange factor ECT2 regulates epithelial cell polarity.* Cellular signalling, 2006. 18(10): p. 1604-1615.

113. Ratheesh, A., et al., *Centralspindlin and [alpha]-catenin regulate Rho signalling*

at the epithelial zonula adherens. Nature cell biology, 2012. 14(8): p. 818-828.

114. Otani, T., et al., *Cdc42 GEF Tuba regulates the junctional configuration of simple epithelial cells.* The Journal of cell biology, 2006. 175(1): p. 135-146.

115. Wells, C.D., et al., *A Rich1/Amot complex regulates the Cdc42 GTPase and apical-polarity proteins in epithelial cells.* Cell, 2006. 125(3): p. 535-548.

116. Biz, M.T., et al., *GTPases RhoA and Rac1 are important for amelogenin and DSPP expression during differentiation of ameloblasts and odontoblasts.* Cell and tissue research, 2010. 340(3): p. 459-470.

117. Rodriguez-Boulan, E. and I.G. Macara, *Organization and execution of the epithelial polarity programme.* Nature reviews Molecular cell biology, 2014. 15(4): p. 225-242.

118. Goehring, N.W., *PAR polarity: from complexity to design principles.* Experimental cell research, 2014. 328(2): p. 258-266.

119. Etienne-Manneville, S., *Cdc42-the centre of polarity.* Journal of cell science, 2004. 117(8): p. 1291-1300.

120. Martin-Belmonte, F. and M. Perez-Moreno, *Epithelial cell polarity, stem cells and cancer.* Nature Reviews Cancer, 2012. 12(1): p. 23-38.

121. Karcher-Djuricic, V., et al., *Basement membrane reconstitution and cytodifferentiation of odontoblasts in isochronal and heterochronal reassociations of enamel organs and pulps.* Journal de biologie buccale, 1978. 6(4): p. 257-265.

122. Kjoelby, M., et al., *Degradation of the dental basement membrane during mouse tooth development in vitro.* International Journal of Developmental Biology, 2002.

38(3): p. 455-462.

123. Heikinheimo, K., et al., *Transforming growth factor beta 2 in epithelial differentiation of developing teeth and odontogenic tumors.* The Journal of clinical investigation, 1993. 91(3): p. 1019-1027.

124. Heikinheimo, K., et al., *EGF receptor and its ligands, EGF and TGF-alpha, in developing and neoplastic human odontogenic tissues.* International Journal of Developmental Biology, 2002. 37(3): p. 387-396.

125. Byers, M., G. Schatteman, and M. Bothwell, *Multiple functions for NGF receptor in developing, aging and injured rat teeth are suggested by epithelial, mesenchymal and neural immunoreactivity.* Development, 1990. 109(2): p. 461-471.

126. Joseph, B., et al., *Expression and regulation of insulin-like growth factor-I in the rat incisor.* Growth Factors, 1993. 8(4): p. 267-275.

127. Miyazaki, T., et al., *Inhibition of the terminal differentiation of odontoblasts and their transdifferentiation into osteoblasts in Runx2 transgenic mice.* Archives of histology and cytology, 2008. 71(2): p. 131-146.

128. Li, S., et al., *The role of runt-related transcription factor 2 (Runx2) in the late stage of odontoblast differentiation and dentin formation.* Biochemical and biophysical research communications, 2011. 410(3): p. 698-704.

129. Li, Y., et al., *TWIST1 promotes the odontoblast-like differentiation of dental stem cells.* Advances in dental research, 2011. 23(3): p. 280-284.

130. Aubin, J., *New immunological approaches to studying the odontoblast.* Journal of

dental research, 1985. 64(4): p. 515-522.

131. Lu, Y., et al., *Rescue of odontogenesis in Dmp1-deficient mice by targeted re-expression of DMP1 reveals roles for DMP1 in early odontogenesis and dentin apposition in vivo.* Developmental biology, 2007. 303(1): p. 191-201.

132. Ye, L., et al., *Deletion of dentin matrix protein-1 leads to a partial failure of maturation of predentin into dentin, hypomineralization and expanded cavities of pulp and root canal during postnatal tooth development.* Journal of Biological Chemistry, 2004.

133. Gluhak-Heinrich, J., et al., *New roles and mechanism of action of BMP4 in postnatal tooth cytodifferentiation.* Bone, 2010. 46(6): p. 1533-1545.

134. Li, J., et al., *SMAD4-mediated WNT signaling controls the fate of cranial neural crest cells during tooth morphogenesis.* Development, 2011: p. dev. 061341.

135. Lin, M., et al., *Wnt5a regulates growth, patterning, and odontoblast differentiation of developing mouse tooth.* Developmental Dynamics, 2011. 240(2): p. 432-440.

136. Vogel, P., et al., *Dentin Dysplasia in Notum Knockout Mice.* Veterinary pathology, 2016. 53(4): p. 853-862.

137. Choi, S., et al., *Mutant DLX 3 disrupts odontoblast polarization and dentin formation.* Developmental biology, 2010. 344(2): p. 682-692.

138. Li, Y., et al., *Odontoblast-like cell differentiation and dentin formation induced with TGF-β1.* Archives of oral biology, 2011. 56(11): p. 1221-1229.

139. Ma, C., et al., *3D Maskless Micropatterning for Regeneration of Highly Organized Tubular Tissues.* Advanced Healthcare Materials, 2017.

140. Li, X., et al., *Pulp regeneration in a full-length human tooth root using a hierarchical nanofibrous microsphere system.* Acta biomaterialia, 2016. 35: p. 57-67.

141. Mammoto, T., et al., *Mechanochemical control of mesenchymal condensation and embryonic tooth organ formation.* Developmental cell, 2011. 21(4): p. 758-769.

142. Hashmi, B., et al., *Mechanical induction of dentin-like differentiation by adult mouse bone marrow stromal cells using compressive scaffolds.* Stem cell research, 2017. 24: p. 55-60.

143. Huang, G.T.-J., K. Shagramanova, and S.W. Chan, *Formation of odontoblast-like cells from cultured human dental pulp cells on dentin in vitro.* Journal of endodontics, 2006. 32(11): p. 1066-1073.

144. Huang, G.T.-J., et al., *In vitro characterization of human dental pulp cells: various isolation methods and culturing environments.* Cell and tissue research, 2006. 324(2): p. 225.

145. Cuffaro, H.M., V. Paakkonen, and L. Tjaderhane, *Enzymatic isolation of viable human odontoblasts.* International Endodontic Journal, 2016. 49(5): p. 454-461.

146. Guo, L., et al., *A novel method to isolate odontoblasts from rat incisor.* Calcified Tissue International, 2000. 66(3): p. 212-216.

147. McBeath, R., et al., *Cell shape, cytoskeletal tension, and RhoA regulate stem cell lineage commitment.* Developmental Cell, 2004. 6(4): p. 483-495.

148. Kumar, G., et al., *The determination of stem cell fate by 3D scaffold structures through the control of cell shape.* Biomaterials, 2011. 32(35): p. 9188-9196.

149. Ma, C., et al., *3D Maskless Micropatterning for Regeneration of Highly Organized Tubular Tissues.* Adv Healthc Mater, 2018. 7(3).

150. Bonewald, L.F., *The Amazing Osteocyte.* Journal of Bone and Mineral Research, 2011. 26(2): p. 229-238.

151. Lee, K.Y. and D.J. Mooney, *Hydrogels for tissue engineering.* Chem. Rev., 2001. 101(7): p. 1869-1879.

152. Wallace, D.G. and J. Rosenblatt, *Collagen gel systems for sustained delivery and tissue engineering.* Advanced Drug Delivery Reviews, 2003. 55(12): p. 1631-1649.

153. Sun, Y., et al., *Biomimetic engineering of nanofibrous gelatin scaffolds with noncollagenous proteins for enhanced bone regeneration.* Tissue Eng Part A, 2013. 19(15-16): p. 1754-1763.

154. Kim, Y.H., et al., *Controlled deposition of a high-performance small-molecule organic single-crystal transistor array by direct ink-jet printing.* Adv Mater, 2012. 24(4): p. 497-502.

155. Cavallini, M., et al., *Micro- and nanopatterning by lithographically controlled wetting.* Nat Protoc, 2012. 7(9): p. 1668-76.

156. Whitesides, G.M., et al., *Soft lithography in biology and biochemistry.* Annual Review of Biomedical Engineering, 2001. 3: p. 335-373.

157. Qin, D., Y. Xia, and G.M. Whitesides, *Soft lithography for micro- and nanoscale patterning.* Nat Protoc, 2010. 5(3): p. 491-502.

158. Kilian, K.A., et al., *Geometric cues for directing the differentiation of mesenchymal stem cells.* Proc Natl Acad Sci U S A, 2010. 107(11): p. 4872-7.

159. Tang, J., R. Peng, and J. Ding, *The regulation of stem cell differentiation by cell-cell contact on micropatterned material surfaces.* Biomaterials, 2010. 31(9): p. 2470-2476.

160. Thery, M., *Micropatterning as a tool to decipher cell morphogenesis and functions.* Journal of Cell Science, 2010. 123(24): p. 4201-4213.

161. DeFife, K.M., et al., *Spatial regulation and surface chemistry control of monocyte/macrophage adhesion and foreign body giant cell formation by photochemically micropatterned surfaces.* Journal of Biomedical Materials Research, 1999. 45(2): p. 148-154.

162. Qu, T., et al., *Complete pulpodentin complex regeneration by modulating the stiffness of biomimetic matrix.* Acta Biomater, 2015. 16: p. 60-70.

163. Peng, R., X. Yao, and J. Ding, *Effect of cell anisotropy on differentiation of stem cells on micropatterned surfaces through the controlled single cell adhesion.* Biomaterials, 2011. 32(32): p. 8048-8057.

164. Liu, X., et al., *Biomimetic nanofibrous gelatin/apatite composite scaffolds for bone tissue engineering.* Biomaterials, 2009. 30(12): p. 2252-2258.

165. Liu, X.H. and P.X. Ma, *Phase separation, pore structure, and properties of nanofibrous gelatin scaffolds.* Biomaterials, 2009. 30(25): p. 4094-4103.

166. Sachar, A., et al., *Cell-matrix and cell-cell interactions of human gingival fibroblasts on three-dimensional nanofibrous gelatin scaffolds.* J Tissue Eng Regen Med, 2012.

167. Sachar, A., et al., *Osteoblasts responses to three-dimensional nanofibrous gelatin*

scaffolds. J Biomed Mater Res Part A, 2012. 100A(11): p. 3029-3041.

168. Sun, M., et al., *Synthesis and properties of gelatin methacryloyl (GelMA) hydrogels and their recent applications in load-bearing tissue.* Polymers, 2018. 10(11): p. 1290.

169. Li, Y., et al., *Improved performance of collagen scaffolds crosslinked by Traut's reagent and Sulfo-SMCC.* Journal of Biomaterials science, Polymer edition, 2017. 28(7): p. 629-647.

170. Hrubi, E., et al., *Diverse effect of BMP-2 homodimer on mesenchymal progenitors of different origin.* Human cell, 2018. 31(2): p. 139-148.

171. Atalayin, C., et al., *Medium modification with bone morphogenetic protein 2 addition for odontogenic differentiation.* Brazilian Oral Research, 2016. 30(1).

172. Chen, H., et al., *Fabrication of nanofibrous scaffolds for tissue engineering applications*, in *Nanomaterials in Tissue Engineering*. 2013, Elsevier. p. 158-183.

173. Harunaga, J.S. and K.M. Yamada, *Cell-matrix adhesions in 3D.* Matrix Biology, 2011. 30(7-8): p. 363-368.

174. Ma, C., et al., *3D maskless micropatterning for regeneration of highly organized tubular tissues.* Advanced healthcare materials, 2018. 7(3): p. 1700738.

175. Moroni, L., et al., *Fiber diameter and texture of electrospun PEOT/PBT scaffolds influence human mesenchymal stem cell proliferation and morphology, and the release of incorporated compounds.* Biomaterials, 2006. 27(28): p. 4911-4922.

176. Nathan, A.S., et al., *Mechano-topographic modulation of stem cell nuclear shape on nanofibrous scaffolds.* Acta biomaterialia, 2011. 7(1): p. 57-66.

177. Kawano, T., et al., *Honeycomb-shaped surface topography induces differentiation of human mesenchymal stem cells (hMSCs): uniform porous polymer scaffolds prepared by the breath figure technique.* Biomaterials science, 2014. 2(1): p. 52-56.

178. Breuls, R.G., T.U. Jiya, and T.H. Smit, *Scaffold stiffness influences cell behavior: opportunities for skeletal tissue engineering.* The open orthopaedics journal, 2008. 2: p. 103.

179. Levy-Mishali, M., J. Zoldan, and S. Levenberg, *Effect of scaffold stiffness on myoblast differentiation.* Tissue Engineering Part A, 2009. 15(4): p. 935-944.

180. Prabhakaran, M.P., L. Ghasemi-Mobarakeh, and S. Ramakrishna, *Electrospun composite nanofibers for tissue regeneration.* Journal of nanoscience and nanotechnology, 2011. 11(4): p. 3039-3057.

181. Kanani, A.G. and S.H. Bahrami, *Review on electrospun nanofibers scaffold and biomedical applications.* Trends Biomater Artif Organs, 2010. 24(2): p. 93-115.

182. Kumar, G., et al., *The determination of stem cell fate by 3D scaffold structures through the control of cell shape.* Biomaterials, 2011. 32(35): p. 9188-9196.

183. von Erlach, T.C., et al., *Cell-geometry-dependent changes in plasma membrane order direct stem cell signalling and fate.* Nature materials, 2018. 17(3): p. 237-242.

184. Kilian, K.A., et al., *Geometric cues for directing the differentiation of mesenchymal stem cells.* Proceedings of the National Academy of Sciences, 2010. 107(11): p. 4872-4877.

185. Li, S., et al., *Effects of nanoscale spatial arrangement of arginine–glycine–aspartate peptides on dedifferentiation of chondrocytes.* Nano letters, 2015. 15(11): p. 7755-7765.

186. Wang, X., et al., *Fabrication of RGD micro/nanopattern and corresponding study of stem cell differentiation.* Nano letters, 2015. 15(3): p. 1457-1467.

187. Hynes, R.O., *The Extracellular Matrix: Not Just Pretty Fibrils.* Science, 2009. 326(5957): p. 1216-1219.

188. Trappmann, B., et al., *Extracellular-matrix tethering regulates stem-cell fate.* Nature Materials, 2012. 11(7): p. 642-649.

189. Silva, G.A., et al., *Selective differentiation of neural progenitor cells by high-epitope density nanofibers.* Science, 2004. 303(5662): p. 1352-1355.

190. Ma, Z., et al., *Potential of nanofiber matrix as tissue-engineering scaffolds.* Tissue engineering, 2005. 11(1-2): p. 101-109.

191. Barnes, C.P., et al., *Nanofiber technology: designing the next generation of tissue engineering scaffolds.* Advanced drug delivery reviews, 2007. 59(14): p. 1413-1433.

192. Liu, W., et al., *Dose-dependent enhancement of bone marrow stromal cells adhesion, spreading and osteogenic differentiation on atmospheric plasma-treated poly (L-lactic acid) nanofibers.* Journal of bioactive and compatible polymers, 2013. 28(5): p. 453-467.

193. Mahboudi, H., et al., *Enhanced chondrogenesis of human bone marrow mesenchymal stem cell (BMSC) on nanofiber-based polyethersulfone (PES)*

scaffold. Gene, 2018. 643: p. 98-106.

194. Magloire, H., et al., *Molecular regulation of odontoblast activity under dentin injury.* Advances in dental research, 2001. 15(1): p. 46-50.

195. Imura, T., et al., *"Microgravity" as a unique and useful stem cell culture environment for cell-based therapy.* Regenerative Therapy, 2019.

196. Otsuka, T., et al., *Simulated microgravity culture enhances the neuroprotective effects of human cranial bone-derived mesenchymal stem cells in traumatic brain injury.* Stem cells and development, 2018. 27(18): p. 1287-1297.

197. Yuge, L., et al., *Simulated microgravity maintains the undifferentiated state and enhances the neural repair potential of bone marrow stromal cells.* Stem cells and development, 2011. 20(5): p. 893-900.

198. Mattei, C., et al., *Generation of neural organoids from human embryonic stem cells using the rotary cell culture system: effects of microgravity on neural progenitor cell fate.* Stem cells and development, 2018. 27(12): p. 848-857.

199. Yuge, L., et al., *Cell differentiation and p38 MARK cascade are inhibited in human osteoblasts cultured in a three-dimensional clinostat.* In Vitro Cellular & Developmental Biology-Animal, 2003. 39(1-2): p. 89-97.

200. Yuge, L., et al., *Microgravity potentiates stem cell proliferation while sustaining the capability of differentiation.* Stem cells and development, 2006. 15(6): p. 921-929.

201. Kawahara, Y., et al., *LIF-free embryonic stem cell culture in simulated microgravity.* PLoS One, 2009. 4(7).

202. Huang, Y., et al., *Gravity, a regulation factor in the differentiation of rat bone marrow mesenchymal stem cells.* Journal of biomedical science, 2009. 16(1): p. 87.

203. He, L., et al., *Increased proliferation and adhesion properties of human dental pulp stem cells in PLGA scaffolds via simulated microgravity.* International endodontic journal, 2016. 49(2): p. 161-173.

204. Li, Y., et al., *Three-dimensional simulated microgravity culture improves the proliferation and odontogenic differentiation of dental pulp stem cell in PLGA scaffolds implanted in mice.* Molecular medicine reports, 2017. 15(2): p. 873-878.

205. Dupont, S., *Role of YAP/TAZ in cell-matrix adhesion-mediated signalling and mechanotransduction.* Experimental cell research, 2016. 343(1): p. 42-53.

206. Dupont, S., et al., *Role of YAP/TAZ in mechanotransduction.* Nature, 2011. 474(7350): p. 179-183.

207. Yang, C., et al., *Mechanical memory and dosing influence stem cell fate.* Nature materials, 2014. 13(6): p. 645-652.

208. Peng, R., et al., *The effect of culture conditions on the adipogenic and osteogenic inductions of mesenchymal stem cells on micropatterned surfaces.* Biomaterials, 2012. 33(26): p. 6008-6019.

209. Jimenez-Vergara, A.C., et al., *Refined assessment of the impact of cell shape on human mesenchymal stem cell differentiation in 3D contexts.* Acta biomaterialia, 2019. 87: p. 166-176.

210. Ruch, J., *Session I: Development, Form, and Function of Odontoblasts—CD. Torneck, Chairman: Odontoblast Differentiation and the Formation of the*

Odontoblast Layer. Journal of dental research, 1985. 64(4): p. 489-498.

211. Chan, E.W. and M.N. Yousaf, *A photo-electroactive surface strategy for immobilizing ligands in patterns and gradients for studies of cell polarization.* Molecular BioSystems, 2008. 4(7): p. 746-753.

212. Wang, X., et al., *Regulating the stemness of mesenchymal stem cells by tuning micropattern features.* Journal of Materials Chemistry B, 2016. 4(1): p. 37-45.

213. Cabahug‐Zuckerman, P., et al., *Potential role for a specialized β3 integrin‐based structure on osteocyte processes in bone mechanosensation.* Journal of Orthopaedic Research®, 2018. 36(2): p. 642-652.

214. Cukierman, E., R. Pankov, and K.M. Yamada, *Cell interactions with three-dimensional matrices.* Current opinion in cell biology, 2002. 14(5): p. 633-640.

215. Sen, B., et al., *Intranuclear actin regulates osteogenesis.* Stem Cells, 2015. 33(10): p. 3065-3076.

216. Seo, E., et al., *SOX2 regulates YAP1 to maintain stemness and determine cell fate in the osteo-adipo lineage.* Cell reports, 2013. 3(6): p. 2075-2087.

217. Zaidi, S.K., et al., *Tyrosine phosphorylation controls Runx2‐mediated subnuclear targeting of YAP to repress transcription.* The EMBO journal, 2004. 23(4): p. 790-799.

218. Zhang, H., et al., *Titanium nanotubes induce osteogenic differentiation through the FAK/RhoA/YAP cascade.* RSC Advances, 2016. 6(50): p. 44062-44069.

219. Kim, S., et al., *Stat1 functions as a cytoplasmic attenuator of Runx2 in the transcriptional program of osteoblast differentiation.* Genes & development, 2003.

17(16): p. 1979-1991.

220. Uemura, M., A. Nagasawa, and K. Terai, *Yap/Taz transcriptional activity in endothelial cells promotes intramembranous ossification via the BMP pathway.* Scientific reports, 2016. 6: p. 27473.

221. Schofield, A.V., R. Steel, and O. Bernard, *Rho-associated coiled-coil kinase (ROCK) protein controls microtubule dynamics in a novel signaling pathway that regulates cell migration.* Journal of Biological Chemistry, 2012. 287(52): p. 43620-43629.

222. Westermann, S. and K. Weber, *Post-translational modifications regulate microtubule function.* Nature Reviews Molecular Cell Biology, 2003. 4(12): p. 938.

223. Khatiwala, C.B., et al., *ECM compliance regulates osteogenesis by influencing MAPK signaling downstream of RhoA and ROCK.* Journal of bone and mineral research, 2009. 24(5): p. 886-898.

224. Xu, Y., et al., *Connective tissue growth factor in regulation of RhoA mediated cytoskeletal tension associated osteogenesis of mouse adipose-derived stromal cells.* PloS one, 2010. 5(6): p. e11279.

225. Miyashita, S., et al., *Mechanical forces induce odontoblastic differentiation of mesenchymal stem cells on three‐dimensional biomimetic scaffolds.* Journal of tissue engineering and regenerative medicine, 2017. 11(2): p. 434-446.

226. Staquet, M.-J., et al., *Expression and localisation of αv integrins in human odontoblasts.* Cell and tissue research, 2006. 323(3): p. 457-463.

227. Saito, K., et al., *Interaction between fibronectin and β1 integrin is essential for*

tooth development. PLoS One, 2015. 10(4).

228. Herold, R.C. and H. Kaye, *Mitochondria in odontoblastic processes.* Nature, 1966. 210(5031): p. 108-109.

229. Couve, E., R. Osorio, and O. Schmachtenberg, *Mitochondrial autophagy and lipofuscin accumulation in aging odontoblasts.* Journal of dental research, 2012. 91(7): p. 696-701.

230. Couve, E., R. Osorio, and O. Schmachtenberg, *The amazing odontoblast: activity, autophagy, and aging.* Journal of dental research, 2013. 92(9): p. 765-772.

231. Blaber, E., K. Sato, and E.A. Almeida, *Stem cell health and tissue regeneration in microgravity.* Stem cells and development, 2014. 23(S1): p. 73-78.

232. Blaber, E.A., et al., *Microgravity reduces the differentiation and regenerative potential of embryonic stem cells.* Stem cells and development, 2015. 24(22): p. 2605-2621.

233. Zayzafoon, M., W.E. Gathings, and J.M. McDonald, *Modeled microgravity inhibits osteogenic differentiation of human mesenchymal stem cells and increases adipogenesis.* Endocrinology, 2004. 145(5): p. 2421-2432.

234. Crawford-Young, S.J., *Effects of microgravity on cell cytoskeleton and embryogenesis.* International journal of developmental biology, 2003. 50(2-3): p. 183-191.

235. Buravkova, L. and Y.A. Romanov, *The role of cytoskeleton in cell changes under condition of simulated microgravity.* Acta astronautica, 2001. 48(5-12): p. 647-650.

236. Pisanu, M.E., et al., *Lung cancer stem cell lose their stemness default state after*

exposure to microgravity. BioMed research international, 2014. 2014.

237. Gershovich, P., et al., *Cytoskeletal proteins and stem cell markers gene expression in human bone marrow mesenchymal stromal cells after different periods of simulated microgravity.* Acta astronautica, 2012. 70: p. 36-42.

238. Nabavi, N., et al., *Effects of microgravity on osteoclast bone resorption and osteoblast cytoskeletal organization and adhesion.* Bone, 2011. 49(5): p. 965-974.

239. Casey, T., O.V. Patel, and K. Plaut, *Transcriptomes reveal alterations in gravity impact circadian clocks and activate mechanotransduction pathways with adaptation through epigenetic change.* Physiological genomics, 2015. 47(4): p. 113-128.

240. Furukawa, T., et al., *Simulated microgravity attenuates myogenic differentiation via epigenetic regulations.* NPJ microgravity, 2018. 4(1): p. 1-8.

241. Ishikawa, M. and Y. Yamada, *The role of pannexin 3 in bone biology.* Journal of dental research, 2017. 96(4): p. 372-379.

242. About, I., et al., *In vivo and in vitro expression of connexin 43 in human teeth.* Connective tissue research, 2002. 43(2-3): p. 232-237.

243. Iwamoto, T., et al., *Pannexin 3 regulates proliferation and differentiation of odontoblasts via its hemichannel activities.* PloS one, 2017. 12(5): p. e0177557.

244. Zhang, C., W. Young, and M. Waters, *Immunocytochemical localization of growth hormone receptor in rat maxillary teeth.* Archives of oral biology, 1992. 37(2): p. 77-84.

245. Thesleff, I. and M. Mikkola, *The role of growth factors in tooth development.*

International review of cytology, 2002. 217: p. 93-135.

246. Zhang, Y.D., et al., *Making a tooth: growth factors, transcription factors, and stem cells.* Cell research, 2005. 15(5): p. 301.

247. Yang, W., et al., *Bmp2 is required for odontoblast differentiation and pulp vasculogenesis.* Journal of dental research, 2012. 91(1): p. 58-64.

248. Yamashiro, T., et al., *Wnt10a regulates dentin sialophosphoprotein mRNA expression and possibly links odontoblast differentiation and tooth morphogenesis.* Differentiation, 2007. 75(5): p. 452-462.

249. Sreenath, T., et al., *Dentin sialophosphoprotein knockout mouse teeth display widened predentin zone and develop defective dentin mineralization similar to human dentinogenesis imperfecta type III.* Journal of Biological Chemistry, 2003. 278(27): p. 24874-24880.

250. Ye, L., et al., *Deletion of dentin matrix protein-1 leads to a partial failure of maturation of predentin into dentin, hypomineralization, and expanded cavities of pulp and root canal during postnatal tooth development.* Journal of Biological Chemistry, 2004. 279(18): p. 19141-19148.

251. Liu, H., S. Gronthos, and S. Shi, *Dental pulp stem cells*, in *Methods in enzymology*. 2006, Elsevier. p. 99-113.

252. Ferro, F., R. Spelat, and C.S. Baheney, *Dental pulp stem cell (DPSC) isolation, characterization, and differentiation*, in *Stem Cells and Tissue Repair*. 2014, Springer. p. 91-115.

253. Gronthos, S., et al., *Postnatal human dental pulp stem cells (DPSCs) in vitro and*

in vivo. Proceedings of the National Academy of Sciences, 2000. 97(25): p. 13625-13630.

254. Mori, G., et al., *Dental pulp stem cells: osteogenic differentiation and gene expression.* Annals of the new York Academy of Sciences, 2011. 1237(1): p. 47-52.

255. Menicanin, D., *Functional and molecular characterisation of mesenchymal stem cells derived from bone marrow and dental tissues*. 2010.

256. Xie, J., et al., *Comparative study of differentiation potential of mesenchymal stem cells derived from orofacial system into vascular endothelial cells.* Beijing da xue xue bao. Yi xue ban= Journal of Peking University. Health sciences, 2019. 51(5): p. 900.

257. Mead, B., et al., *Dental pulp, bone marrow and adipose-derived mesenchymal stem cell therapies for optic neuropathies.* Investigative Ophthalmology & Visual Science, 2014. 55(13): p. 2161-2161.

258. Lee, Y.-C., et al., *Comparing the Osteogenic Potentials and Bone Regeneration Capacities of Bone Marrow and Dental Pulp Mesenchymal Stem Cells in a Rabbit Calvarial Bone Defect Model.* International journal of molecular sciences, 2019. 20(20): p. 5015.

259. Oh, H.-J., et al., *CPNE7, a preameloblast-derived factor, regulates odontoblastic differentiation of mesenchymal stem cells.* Biomaterials, 2015. 37: p. 208-217.

260. Zhang, L. and C. Chan, *Isolation and enrichment of rat mesenchymal stem cells (MSCs) and separation of single-colony derived MSCs.* J Vis Exp, 2010(37).

261. Borek, C., S. Higashino, and W. Loewenstein, *Intercellular communication and tissue growth.* The Journal of membrane biology, 1969. 1(1): p. 274-293.

262. Loewenstein, W.R., *Junctional intercellular communication and the control of growth.* Biochimica et Biophysica Acta (BBA)-Reviews on Cancer, 1979. 560(1): p. 1-65.

263. Civitelli, R., *Cell-cell communication in bone.* 1998.

264. Van der Plas, A. and P. Nijweide, *Cell-cell interactions in the osteogenic compartment of bone.* Bone, 1988. 9(2): p. 107-111.

265. Stains, J.P. and R. Civitelli, *Cell‐cell interactions in regulating osteogenesis and osteoblast function.* Birth Defects Research Part C: Embryo Today: Reviews, 2005. 75(1): p. 72-80.

266. Hassanzadeh-Barforoushi, A., et al., *A rapid co-culture stamping device for studying intercellular communication.* Scientific reports, 2016. 6(1): p. 1-11.

267. Efremov, A.N., et al., *Micropatterned superhydrophobic structures for the simultaneous culture of multiple cell types and the study of cell–cell communication.* Biomaterials, 2013. 34(7): p. 1757-1763.

268. Hebert, C. and J.P. Stains, *An intact connexin43 is required to enhance signaling and gene expression in osteoblast‐like cells.* Journal of cellular biochemistry, 2013. 114(11): p. 2542-2550.

269. Stains, J.P., et al., *Molecular mechanisms of osteoblast/osteocyte regulation by connexin43.* Calcified tissue international, 2014. 94(1): p. 55-67.

270. Nadiri, A., et al., *Immunolocalization of BMP-2/-4, FGF-4, and WNT10b in the*

developing mouse first lower molar. Journal of Histochemistry & Cytochemistry, 2004. 52(1): p. 103-112.

271. Huang, X.F. and Y. Chai, *TGF-β signalling and tooth development.* Chin J Dent Res, 2010. 13(1): p. 7-13.

272. Huojia, M., et al., *TGF‐β3 induces ectopic mineralization in fetal mouse dental pulp during tooth germ development.* Development, growth & differentiation, 2005. 47(3): p. 141-152.

273. Kratochwil, K., et al., *Lef1 expression is activated by BMP-4 and regulates inductive tissue interactions in tooth and hair development.* Genes & development, 1996. 10(11): p. 1382-1394.

274. Nakashima, M., *Bone morphogenetic proteins in dentin regeneration for potential use in endodontic therapy.* Cytokine & growth factor reviews, 2005. 16(3): p. 369-376.

275. Arany, P.R., et al., *Photoactivation of endogenous latent transforming growth factor–β1 directs dental stem cell differentiation for regeneration.* Science translational medicine, 2014. 6(238): p. 238ra69-238ra69.

276. Niwa, T., et al., *The dynamics of TGF-β in dental pulp, odontoblasts and dentin.* Scientific reports, 2018. 8(1): p. 1-14.

277. Dobie, K., et al., *Effects of alginate hydrogels and TGF-β1 on human dental pulp repair in vitro.* Connective tissue research, 2002. 43(2-3): p. 387-390.

278. Howard, C., P.E. Murray, and K.N. Namerow, *Dental pulp stem cell migration.* Journal of endodontics, 2010. 36(12): p. 1963-1966.

279. Jonker, L., *TGF - β & BMP Receptors Endoglin and ALK 1: Overview of their Functional Role and Status as Antiangiogenic Targets.* Microcirculation, 2014. 21(2): p. 93-103.

280. Watabe, T. and K. Miyazono, *Roles of TGF-β family signaling in stem cell renewal and differentiation.* Cell research, 2009. 19(1): p. 103-115.

281. Iohara, K., et al., *Dentin regeneration by dental pulp stem cell therapy with recombinant human bone morphogenetic protein 2.* Journal of dental research, 2004. 83(8): p. 590-595.

282. Casagrande, L., et al., *Dentin-derived BMP-2 and odontoblast differentiation.* Journal of dental research, 2010. 89(6): p. 603-608.

283. Wang, W., et al., *Dentin regeneration by stem cells of apical papilla on injectable nanofibrous microspheres and stimulated by controlled BMP-2 release.* Acta biomaterialia, 2016. 36: p. 63-72.

284. Washio, A., et al., *Possible involvement of Smad signaling pathways in induction of odontoblastic properties in KN-3 cells by bone morphogenetic protein-2: a growth factor to induce dentin regeneration.* International journal of dentistry, 2012. 2012.

285. Vainio, S., et al., *Identification of BMP-4 as a signal mediating secondary induction between epithelial and mesenchymal tissues during early tooth development.* Cell, 1993. 75(1): p. 45-58.

286. Ohazama, A., A. Tucker, and P. Sharpe, *Organized tooth-specific cellular differentiation stimulated by BMP4.* Journal of dental research, 2005. 84(7): p.

603-606.

287. Koussoulakou, D.S., L.H. Margaritis, and S.L. Koussoulakos, *Anti-BMP4 monoclonal antibody delays mandibular osteogenesis and affects odontoblast differentiation.* Hellenic Orthodontic Review, 2006. 9(1).

288. Kawazoe, Y., et al., *Activation of the FGF signaling pathway and subsequent induction of mesenchymal stem cell differentiation by inorganic polyphosphate.* International journal of biological sciences, 2008. 4(1): p. 37.

289. Nakashima, M., *Induction of dentine in amputated pulp of dogs by recombinant human bone morphogenetic proteins-2 and-4 with collagen matrix.* Archives of oral biology, 1994. 39(12): p. 1085-1089.

290. Nakashima, M., K. Iohara, and L. Zheng, *Gene therapy for dentin regeneration with bone morphogenetic proteins.* Current gene therapy, 2006. 6(5): p. 551-560.

291. Bei, M. and R. Maas, *FGFs and BMP4 induce both Msx1-independent and Msx1-dependent signaling pathways in early tooth development.* Development, 1998. 125(21): p. 4325-4333.

292. Kettunen, P., I. Karavanova, and I. Thesleff, *Responsiveness of developing dental tissues to fibroblast growth factors: expression of splicing alternatives of FGFR1, ‐2, ‐3, and of FGFR4; and stimulation of cell proliferation by FGF ‐2, ‐4, ‐8, and ‐9.* Developmental genetics, 1998. 22(4): p. 374-385.

293. Kettunen, P., et al., *Associations of FGF ‐3 and FGF ‐10 with signaling networks regulating tooth morphogenesis.* Developmental dynamics: an official publication of the American Association of Anatomists, 2000. 219(3): p. 322-332.

294. Tsuboi, T., et al., *Fgf-2 regulates enamel and dentine formation in mouse tooth germ.* Calcified tissue international, 2003. 73(5): p. 496-501.

295. Sonmez, A.B. and J. Castelnuovo, *Applications of basic fibroblastic growth factor (FGF‐2, bFGF) in dentistry.* Dental Traumatology, 2014. 30(2): p. 107-111.

296. Kitamura, C., et al., *Local regeneration of dentin-pulp complex using controlled release of fgf-2 and naturally derived sponge-like scaffolds.* International journal of dentistry, 2012. 2012.

297. Ishimatsu, H., et al., *Formation of dentinal bridge on surface of regenerated dental pulp in dentin defects by controlled release of fibroblast growth factor–2 from gelatin hydrogels.* Journal of endodontics, 2009. 35(6): p. 858-865.

298. Terranova, V.P., et al., *Repopulation of dentin surfaces by periodontal ligament cells and endothelial cells: effect of basic fibroblast growth factor.* Journal of periodontology, 1989. 60(6): p. 293-301.

299. Rossa Jr, C., et al., *Regeneration of Class III furcation defects with basic fibroblast growth factor (b‐FGF) associated with GTR. A descriptive and histometric study in dogs.* Journal of periodontology, 2000. 71(5): p. 775-784.

300. Norouzi, M., et al., *PLGA/gelatin hybrid nanofibrous scaffolds encapsulating EGF for skin regeneration.* Journal of Biomedical Materials Research Part A, 2015. 103(7): p. 2225-2235.

301. Raper, S.E., et al., *Translocation of epidermal growth factor to the hepatocyte nucleus during rat liver regeneration.* Gastroenterology, 1987. 92(5): p. 1243-1250.

302. Humes, H.D., et al., *Epidermal growth factor enhances renal tubule cell regeneration and repair and accelerates the recovery of renal function in postischemic acute renal failure.* The Journal of clinical investigation, 1989. 84(6): p. 1757-1761.

303. Marquez, L., et al., *Enhanced bone healing of rat tooth sockets after administration of epidermal growth factor (EGF) carried by liposome.* Injury, 2013. 44(4): p. 558-564.

304. Wallmichrath, J., et al., *Epidermal growth factor (EGF) transfection of human bone marrow stromal cells in bone tissue engineering.* Journal of cellular and molecular medicine, 2009. 13(8b): p. 2593-2601.

305. Tamama, K., H. Kawasaki, and A. Wells, *Epidermal growth factor (EGF) treatment on multipotential stromal cells (MSCs). Possible enhancement of therapeutic potential of MSC.* BioMed Research International, 2010. 2010.

306. Mehta, V.B., et al., *HB-EGF promotes angiogenesis in endothelial cells via PI3-kinase and MAPK signaling pathways.* Growth factors, 2007. 25(4): p. 253-263.

307. McVicar, C., et al., *Angiogenesis Induced by EGF Is Mediated by Autocrine VEGF.* Investigative Ophthalmology & Visual Science, 2007. 48(13): p. 1379-1379.

308. Kajihara, T., et al., *Expression of hepatocyte growth factor/scatter factor and c-Met in human dental papilla and fibroblasts from dental papilla.* Archives of oral biology, 1999. 44(2): p. 135-147.

309. Sonnenberg, E., et al., *Scatter factor/hepatocyte growth factor and its receptor, the c-met tyrosine kinase, can mediate a signal exchange between mesenchyme and*

epithelia during mouse development. The Journal of cell biology, 1993. 123(1): p. 223-235.

310. Tabata, M.J., et al., *Hepatocyte growth factor is involved in the morphogenesis of tooth germ in murine molars.* Development, 1996. 122(4): p. 1243-1251.

311. Tomson, P.L., et al., *Hepatocyte growth factor is sequestered in dentine matrix and promotes regeneration-associated events in dental pulp cells.* Cytokine, 2013. 61(2): p. 622-629.

312. Ye, L., et al., *HGF enhanced proliferation and differentiation of dental pulp cells.* Journal of endodontics, 2006. 32(8): p. 736-741.

313. Tamura, M. and E. Nemoto, *Role of the Wnt signaling molecules in the tooth.* Japanese Dental Science Review, 2016. 52(4): p. 75-83.

314. Dassule, H.R. and A.P. McMahon, *Analysis of epithelial–mesenchymal interactions in the initial morphogenesis of the mammalian tooth.* Developmental biology, 1998. 202(2): p. 215-227.

315. Tamura, M., et al., *Role of the Wnt signaling pathway in bone and tooth.* Front Biosci (Elite Ed), 2010. 2: p. 1405-1413.

316. Cai, J., et al., *Wnt5a plays a crucial role in determining tooth size during murine tooth development.* Cell and tissue research, 2011. 345(3): p. 367.

317. Peng, L., et al., *Expression of Wnt5a in tooth germs and the related signal transduction analysis.* Archives of oral biology, 2010. 55(2): p. 108-114.

318. Peng, L., et al., *WNT5A inhibits human dental papilla cell proliferation and migration.* Biochemical and biophysical research communications, 2009. 390(3):

p. 1072-1078.

319. Peng, L., et al., *Wnt5a promotes differentiation of human dental papilla cells.* International endodontic journal, 2010. 43(5): p. 404-412.

320. Hosoya, A., et al., *Sonic Hedgehog Signaling and Tooth Development.* International Journal of Molecular Sciences, 2020. 21(5): p. 1587.

321. Shimo, T., et al., *Sonic hedgehog positively regulates odontoblast differentiation by a BMP2/4-dependent mechanism.* Journal of Oral Tissue Engineering, 2009. 7(1): p. 26-37.

322. Ota, M.S., *The role of Sonic hedgehog signaling and fibroblast growth factors in tooth development in mice.* Journal of Oral Biosciences, 2008. 50(3): p. 167-174.

323. Sarkar, L., et al., *Wnt/Shh interactions regulate ectodermal boundary formation during mammalian tooth development.* Proceedings of the National Academy of Sciences, 2000. 97(9): p. 4520-4524.

324. Wang, X.-P., et al., *Runx2 (Cbfa1) inhibits Shh signaling in the lower but not upper molars of mouse embryos and prevents the budding of putative successional teeth.* Journal of dental research, 2005. 84(2): p. 138-143.

325. Ishikawa, Y., et al., *Quiescent adult stem cells in murine teeth are regulated by Shh signaling.* Cell and tissue research, 2017. 369(3): p. 497-512.

326. Zhao, H., et al., *Secretion of shh by a neurovascular bundle niche supports mesenchymal stem cell homeostasis in the adult mouse incisor.* Cell stem cell, 2014. 14(2): p. 160-173.

327. Feng, J., et al., *BMP signaling orchestrates a transcriptional network to control*

the fate of mesenchymal stem cells in mice. Development, 2017. 144(14): p. 2560-2569.

328. Xia, L., et al., *Enhanced dentin-like mineralized tissue formation by AdShh-transfected human dental pulp cells and porous calcium phosphate cement.* PloS one, 2013. 8(5).

329. Ma, C., et al., *Bio‐Inspired Micropatterned Platforms Recapitulate 3D Physiological Morphologies of Bone and Dentinal Cells.* Advanced Science, 2018: p. 1801037.

330. Qin, C., et al., *Dentin sialoprotein in bone and dentin sialophosphoprotein gene expressed by osteoblasts.* Connective tissue research, 2003. 44(1): p. 179-183.

331. Baba, O., et al., *Detection of dentin sialoprotein in rat periodontium.* European journal of oral sciences, 2004. 112(2): p. 163-170.

332. Lesot, H., et al., *Membrane-cytoskeleton interactions: inhibition of odontoblast differentiation by a monoclonal antibody directed against a membrane protein.* Differentiation, 1988. 37(1): p. 62-72.

333. LESOT, H., et al., *Immunofluorescent localization of vimentin, prekeratin and actin during odontoblast and ameloblast differentiation.* Differentiation, 1982. 21(1‐3): p. 133-137.

334. Vicente-Manzanares, M., et al., *Non-muscle myosin II takes centre stage in cell adhesion and migration.* Nature reviews Molecular cell biology, 2009. 10(11): p. 778.

335. Anderson, L.R., T.W. Owens, and M.J. Naylor, *Structural and mechanical*

functions of integrins. Biophysical reviews, 2014. 6(2): p. 203-213.

336. Chang, B., C. Ma, and X. Liu, *Nanofibers Regulate Single Bone Marrow Stem Cell Osteogenesis via FAK/RhoA/YAP1 Pathway.* ACS applied materials & interfaces, 2018. 10(39): p. 33022-33031.

APPENDIX A

FIGURES

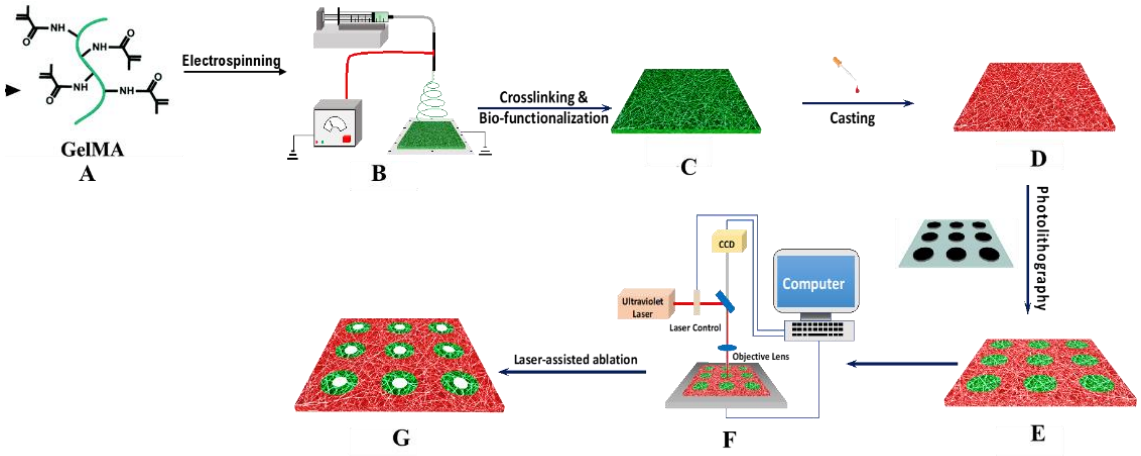

Figure 1. Illustration of the fabrication process of a nanofibrous micropatterned tubular 3D platform.
A. GelMA syntheses from gelatin and methacrylic anhydride. **B.** GelMA was used as the raw material for electrospinning. **C.** A membrane-like GelMA matrix was generated after chemical crosslinking and/or conjugation with bioactive factors. **D.** A mixture of PEGDA and photoinitiator was casted onto the GelMA matrix. **E.** The matrix-PEGDA-photoinitiator complex was placed under a photomask for photolithographpy. **F.** A laser ablation technique was applied on the patterned matrix to generate dentinal tubule-like microchannels. **G.** The resultant 3D tubular microislands. Modified with permission from [329].

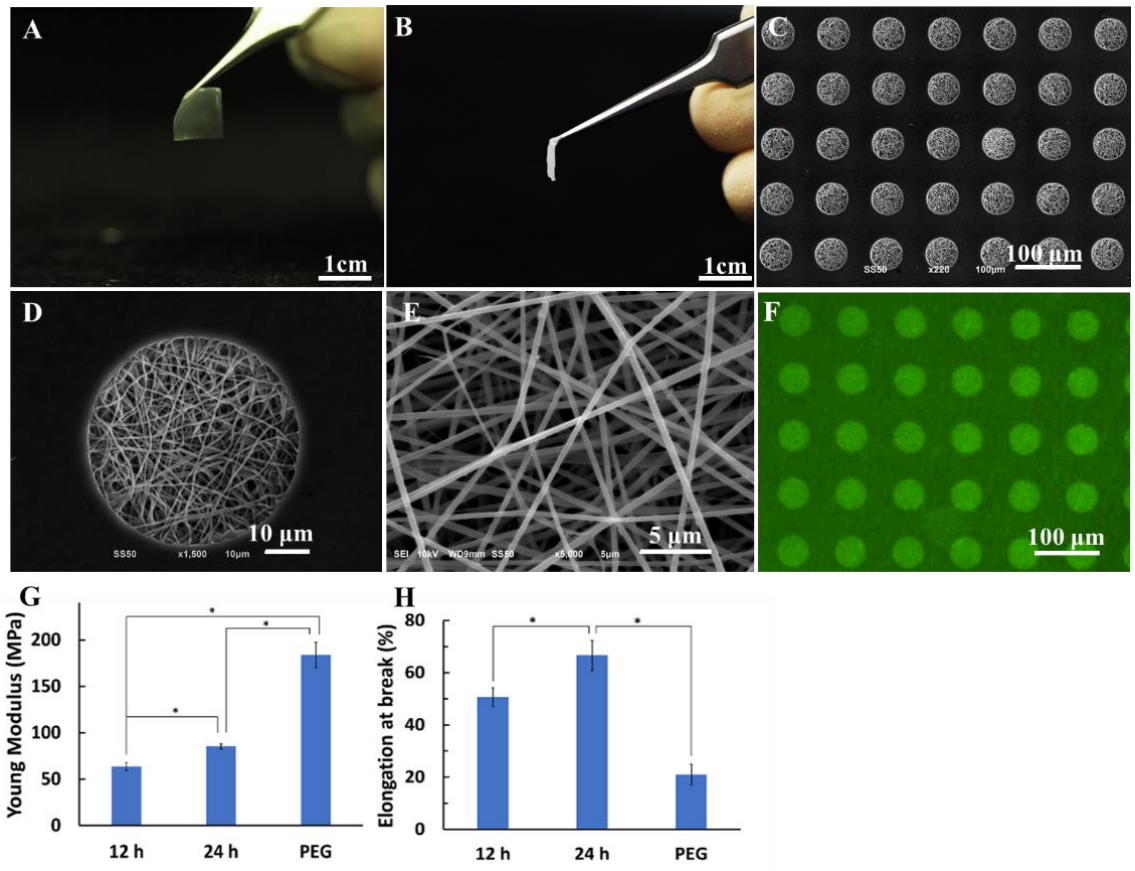

Figure 2. Morphology and mechanical strength of the micropatterned gelatin matrix.

(**A**) and (**B**) are photographical images of a NF-MP scaffold, showing the matrix is transparent and easy to handle. **C.** SEM image of circular NF-MP microislands of 60 µm in diameter. **D**. The magnified image of (**C**), exhibiting the distinct surface topography within and surrounding a microisland. **E.** SEM image showing the GelMA nanofibers within a NF-MP microisland. **F.** Confocal image showing the morphology of FITC-conjugated NF-MPs under a fluorescent microscope. **G**. The Young's modulus of the gelatin nanofibrous matrix with crosslinking time of 12 hours and 24 hours, and the micropatterned matrix with PEGDA. **H**. The elongation at break of the gelatin nanofibrous matrix with crosslinking time of 12 hours and 24 hours, and the micropatterned matrix with PEGDA. Modified with permission from [329].

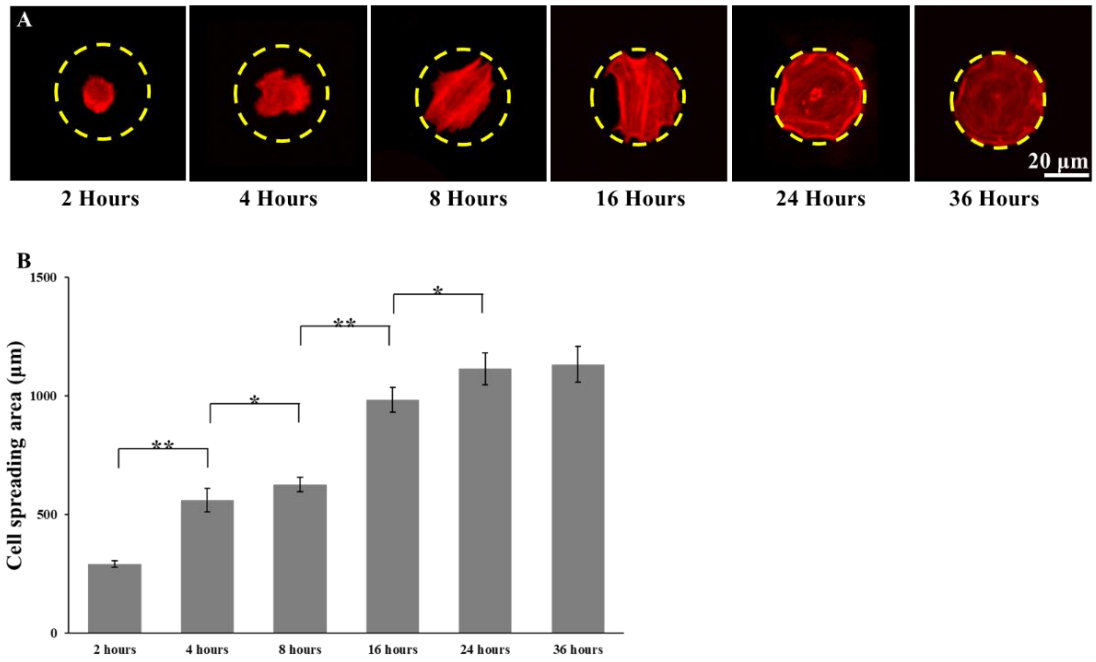

Figure 3. Cell tracking of single hDPSCs on NF-MPs.
(**A**) shows the cellular morphologies at different timepoints, 2, 4, 8, 16, 24, 36 hours after cell seeding, respectively. (**B**) shows the change in cell spreading area at different timepoints.

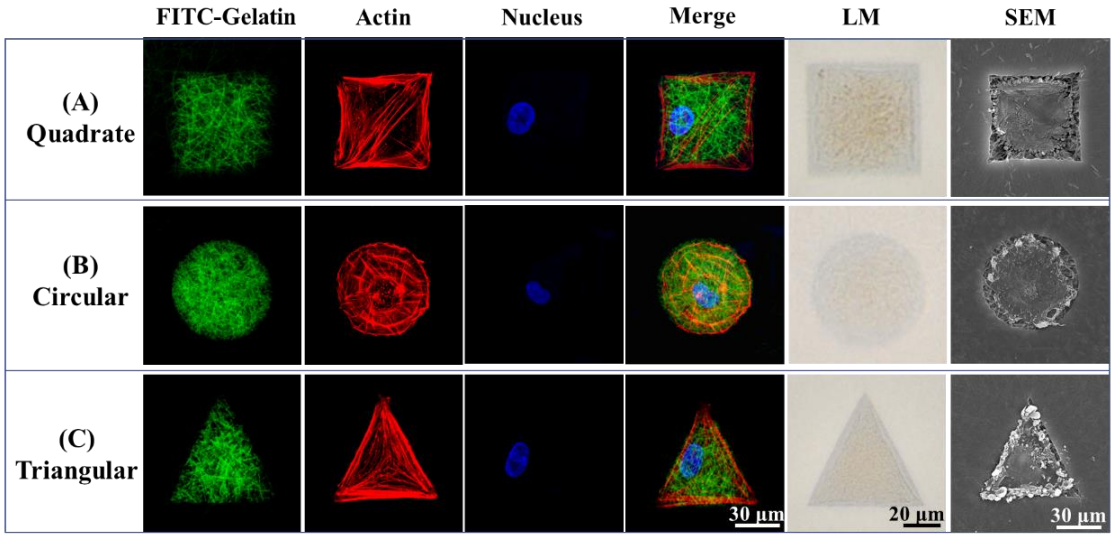

Figure 4. Morphology of single hDPSCs on NF-MP microislands of different shapes.

Images are shown by confocal microscope, light microscope and SEM, respectively. (**A**) shows the quadrate NF-MP microislands with a side length of 60μm, (**B**) shows the circular NF-MP microislands with a diameter of 60μm and (**C**) shows the triangular NF-MP microislands with a side length of 60μm. Red indicates phalloidin-stained actin filaments, green indicates FITC-conjugated GelMA nanofibers and blue indicates the nuclei.

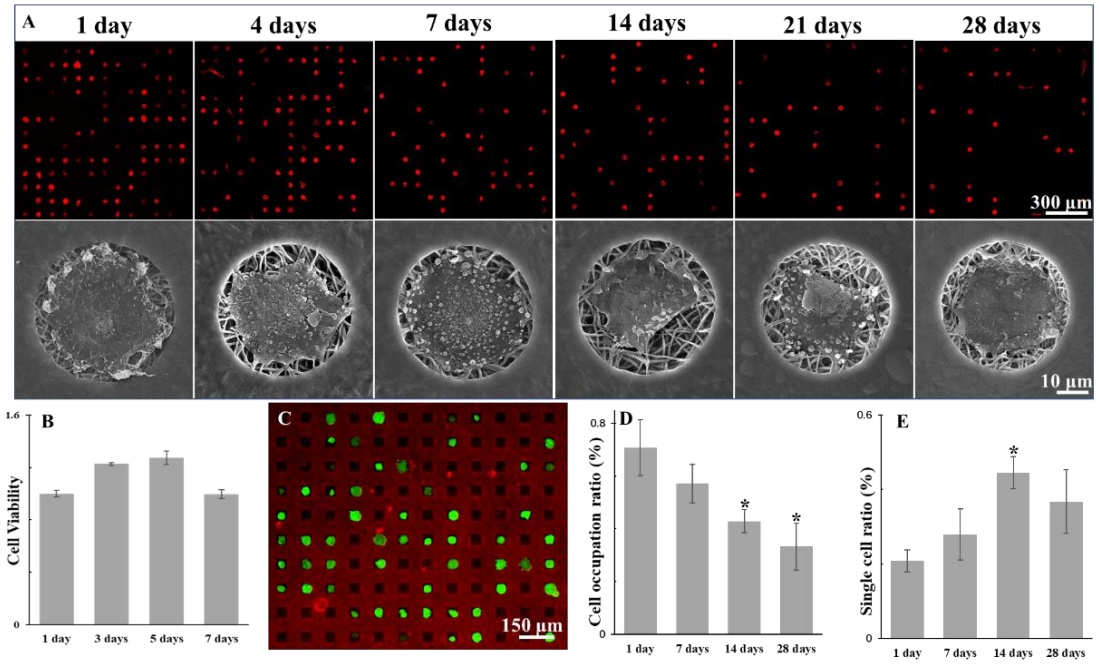

Figure 5. Stability of the NF-MP.
A. HDPSC adhesion status on NF-MP microislands are shown by confocal images and SEM images after the cells are seeded for 1, 4, 7, 14, 21 and 28 days, respectively. It's seen that microisland boundaries remain clear and the cell-limiting effect of PEGDA remains good at each timepoint. **B.** MTT assay shows the vitality of hDPSCs on a NF-MP scaffold at 1, 3, 5 and 7 days after cell seeding. **C.** Live-dead staining implies the vitality of cells attached on the GelMA surface and PEGDA surface. Red dots indicate dead cells, green dots indicate live cells and quadrate frames indicate NF-MP microislands. **D.** Cell occupation ratio shows the changes in cell number on the NF-MP microislands with time. **E**. Single cell ratio shows the changes in cell distribution pattern on the NF-MP microislands with time.

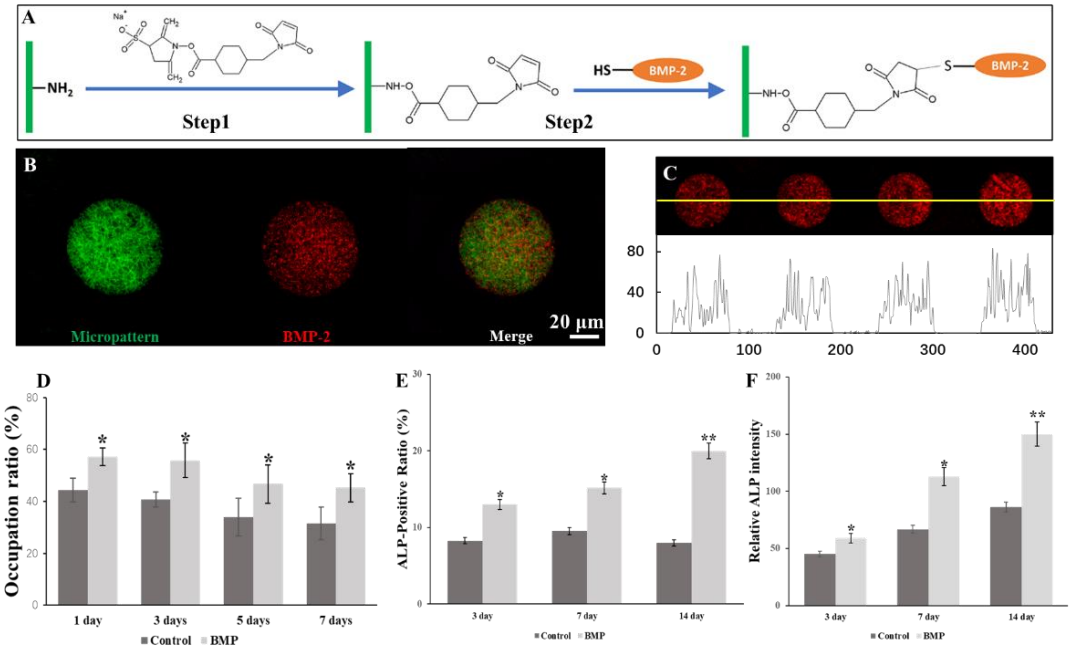

Figure 6. Conjugation of BMP-2 proteins onto the nanofibers of the NF-MP microislands.

A. Shown are the steps of the conjugation process. In step 1, the NHS-ester groups reacted with the amino group (-NH2) on the GelMA nanofibers. In step 2, the maleimide groups reacted with the –SH group on the BMP-2. **B.** Shown is the successful conjugation of BMP-2 proteins on a NF-MP microisland with a diameter of 60 μm. Green indicates FITC-labeled nanofibers and red indicates BMP-2 proteins. **C.** The distribution of BMP-2 proteins on the NF-MP microislands. The values of the relative intensity indicate that the BMP-2 can only be detected inside the microislands. Red indicates BMP-2 signals. (**D**) shows cell occupation ratios of the NF-MP scaffolds with/without BMP-2 conjugation at 1, 3, 5 and 7 days after cell seeding. **E.** The ALP-positive ratio and (**F**) relative ALP intensity of hDPSCs cultured on the NF-MP microislands with/without BMP-2 conjugation at 3,7 and 14 days after cell seeding. Modified with permission from [329].

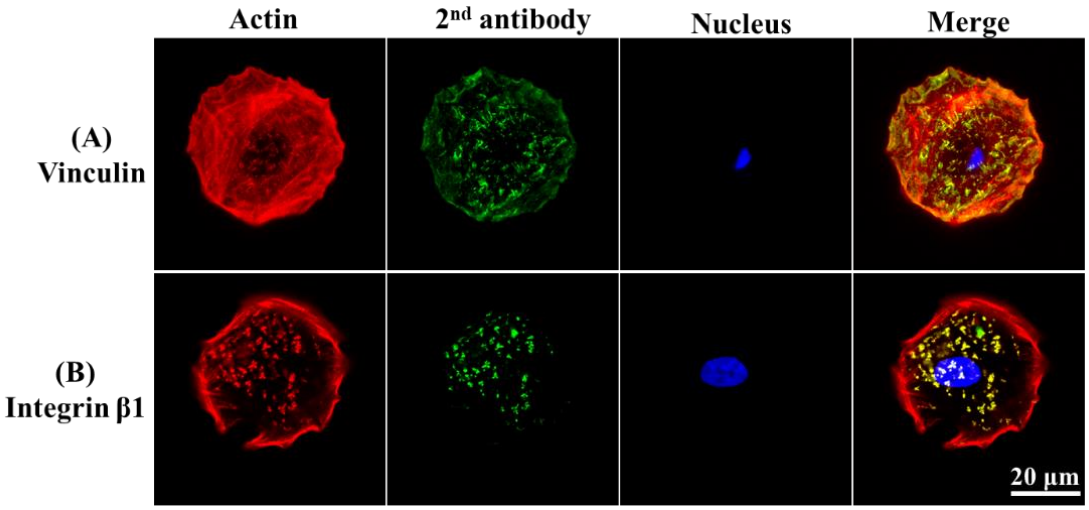

Figure 7. Formation of focal adhesion within single hDPSCs on the NF-MP microislands.
A. Shown is the distribution of vinculin within a hDPSC. **B.** Shown is the distribution of integrin β1 proteins within a hDPSC. Red indicates phalloidin-stained actin filaments, green indicates the focal adhesion proteins (vinculin and integrin β1) and blue indicates the nuclei. Modified with permission from [329].

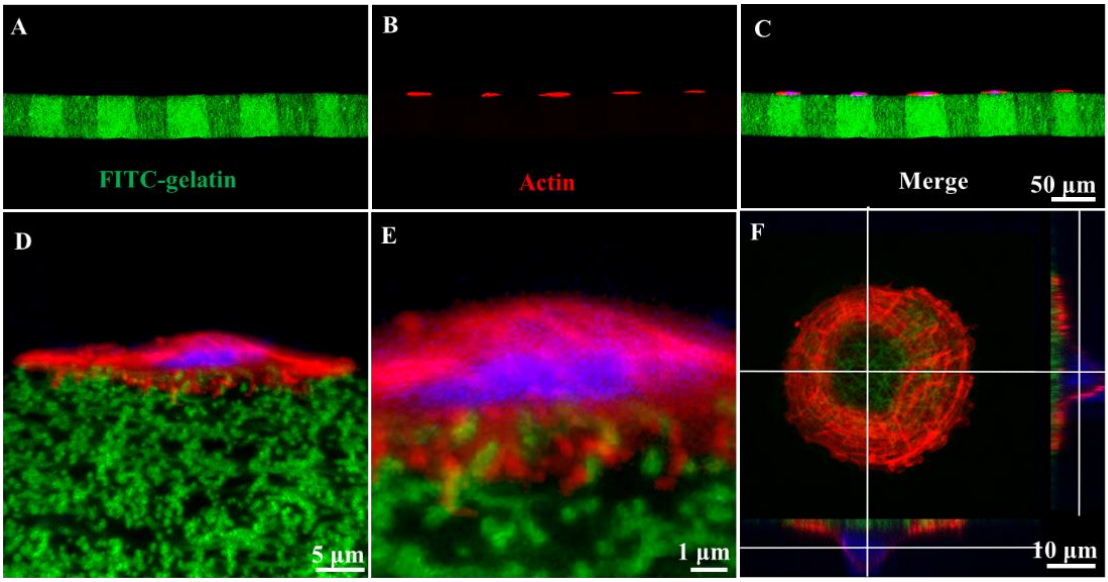

Figure 8. Lateral views of hDPSCs on the NF-MP microislands.
A. The cross-section of the micropatterned matrix. The cubic areas with stronger green signals indicate GelMA microislands and the areas of lower signals indicate PEGDA. **B.** The cross-section views of hDPSCs. **C.** The merged image of (**A**) and (**B**), showing that hDPSCs only attach on the GelMA surface. (**D**) and (**E**) are enlarged confocal images of (**C**), showing the short pseudopodia of the hDPSCs inserted into the nanofibrous matrix. **F.** Confocal z-stacked series in 3D cross section shows the lateral view of a hDPSC on a NF-MP microisland. Red indicates phalloidin-stained actin filaments, green indicates FITC-conjugated GelMA nanofibers and blue indicates the nuclei. Modified with permission from [329].

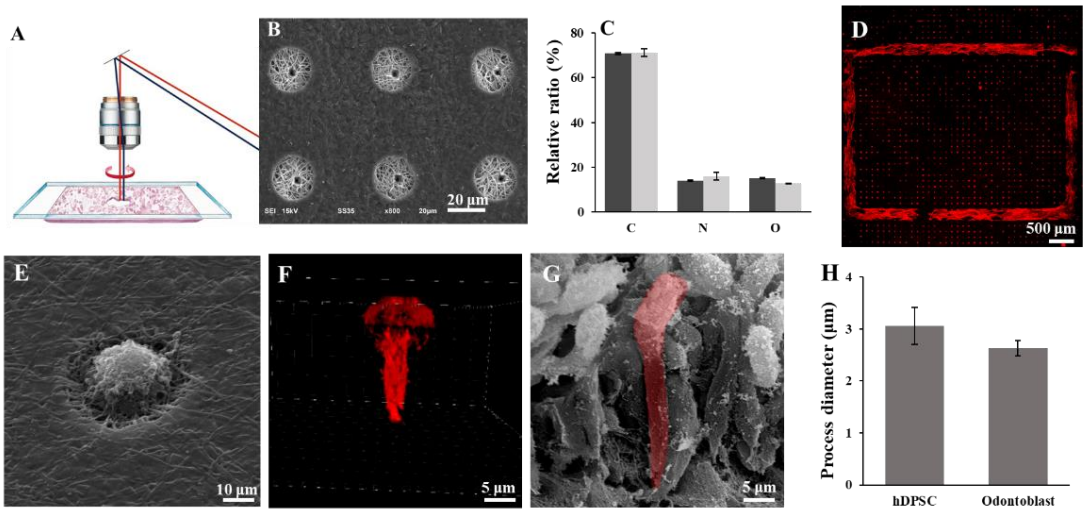

Figure 9. Generation of the 3D tubular architecture within the NF-MP microislands.

(**A**) shows the laser ablation technique. (**B**) shows morphology of resultant tubular NF-MP microislands (NF-MTs) and the diameter of the laser-drilled microchannels. **C**. Quantitative SEM-EDS analysis of the element compositions (carbon, nitrogen and oxygen) outside and inside the laser areas. **D**. Cell occupation statuses of hDPSCs on the NF-MT microislands (within the red rectangular frame) and the NF-MP microislands (outside the red rectangular frame). Red indicates phalloidin-stained cells. **E**. SEM image shows the top-view morphology of a single hDPSC on a NF-MP microisland. **F**. Reconstructed confocal image of a single hDPSC on a NF-MP microisland. **G**. SEM image shows natural odontoblasts. Red color is used to outline a typical odontoblast. (**H**) compares the diameters of the cellular process within a hDPSC on the NF-MT microisland and that of the natural odontoblasts.

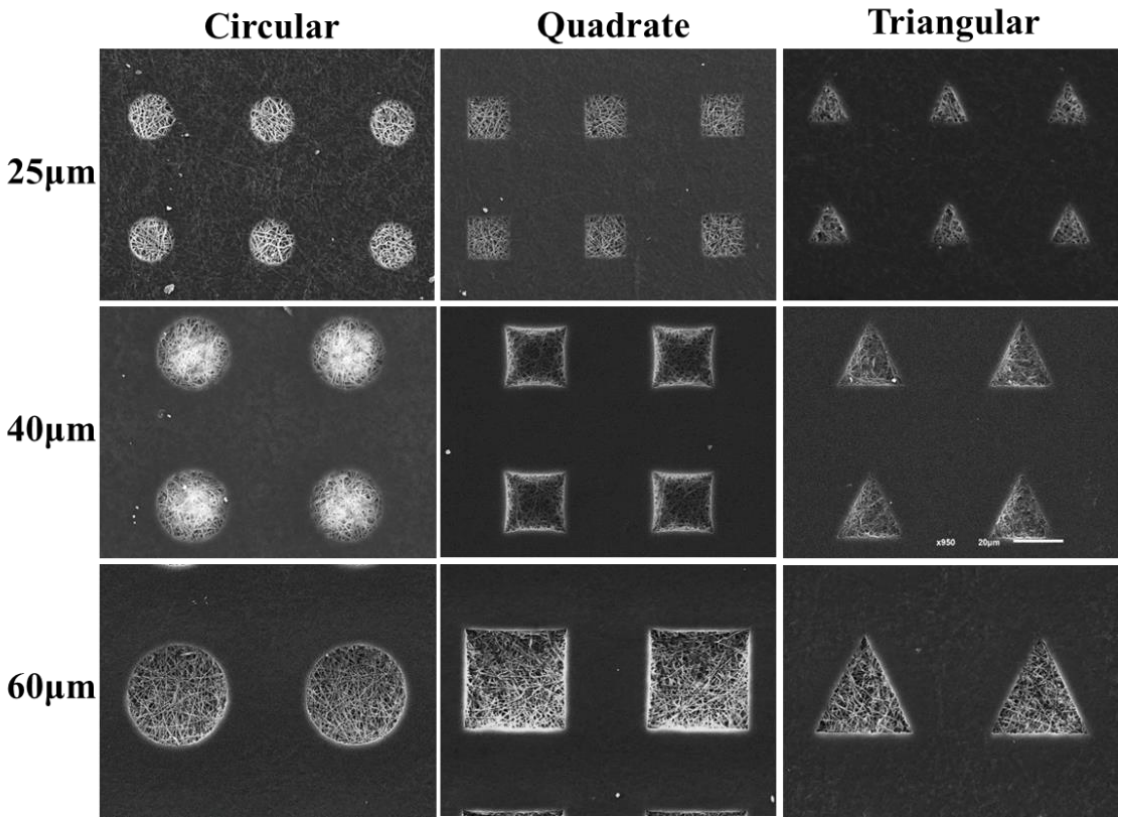

Figure 10. SEM images of NF-MP microislands with various sizes and shapes. The first column shows circular NF-MPs with diameters of 25, 40 and 60μm, respectively. The second column shows quadrate NF-MPs with side lengths of 25, 40 and 60μm. The third column shows triangular NF-MP with side lengths of 25, 40 and 60μm.

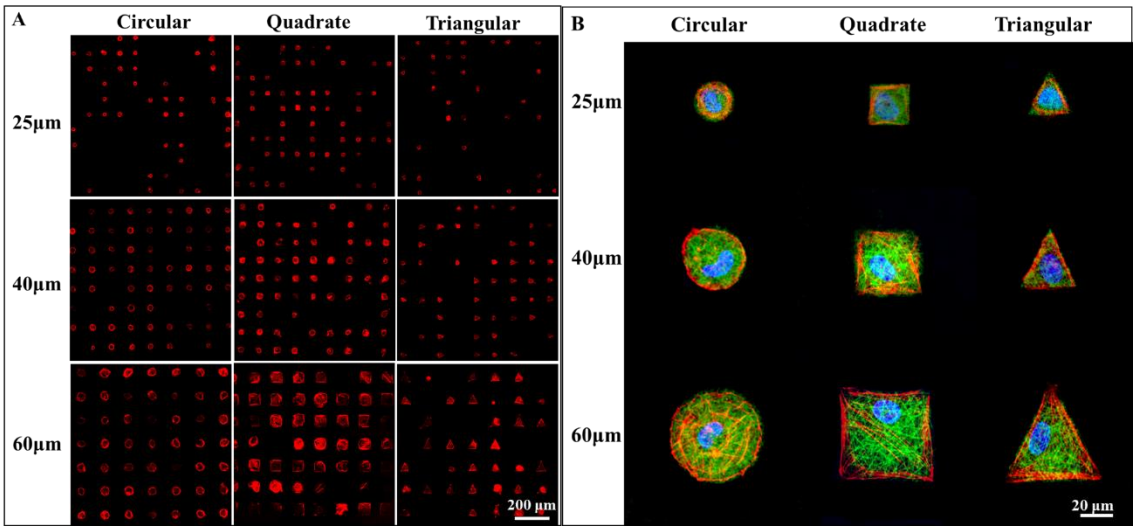

Figure 11. Confocal images of hDPSCs on NF-MP microislands of various sizes and shapes.

Sizes include diameters of 25, 40 and 60µm and shapes include circular, quadrate and triangular. (**A**) shows the hDPSC adhesion statuses on NF-MP scaffolds with different designs. All NF-MP scaffolds display high occupation ratios, regardless of the sizes or shapes. (**B**) shows the morphologies of single hDPSCs accommodated within each NF-MP microisland. Each single hDPSC recapitulates the morphology of its underlying microisland, regardless of its size or shape. Red indicates phalloidin-stained actin filaments, green indicates FITC-conjugated GelMA nanofibers and blue indicates the nuclei.

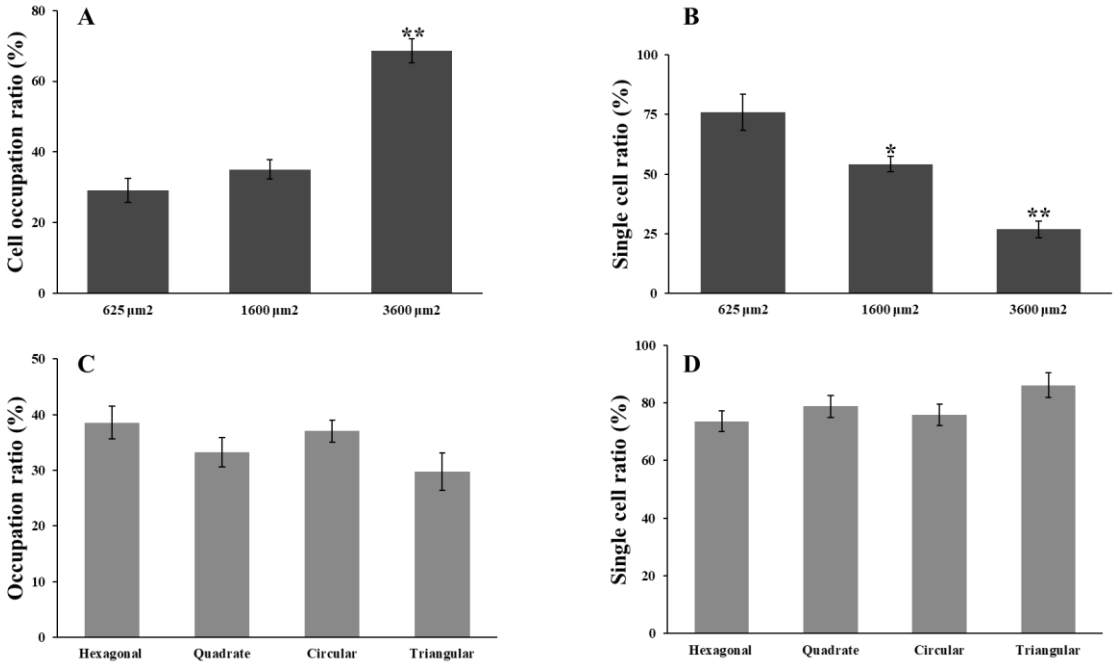

Figure 12. Quantitative data of hDPSC adhesion on NF-MP microislands of various sizes and shapes.

(**A**) and (**B**) show cell occupation ratio and single cell ratio of hDPSCs on quadrate NF-MP microislands with different surface areas (625, 1600 and 3600 μm^2), respectively. (**C**) and (**D**) show cell occupation ratio and single cell ratio of hDPSCs on NF-MP microislands with same area (1600 μm^2) but different shapes (hexagonal, quadrate, circular, and triangular), respectively.

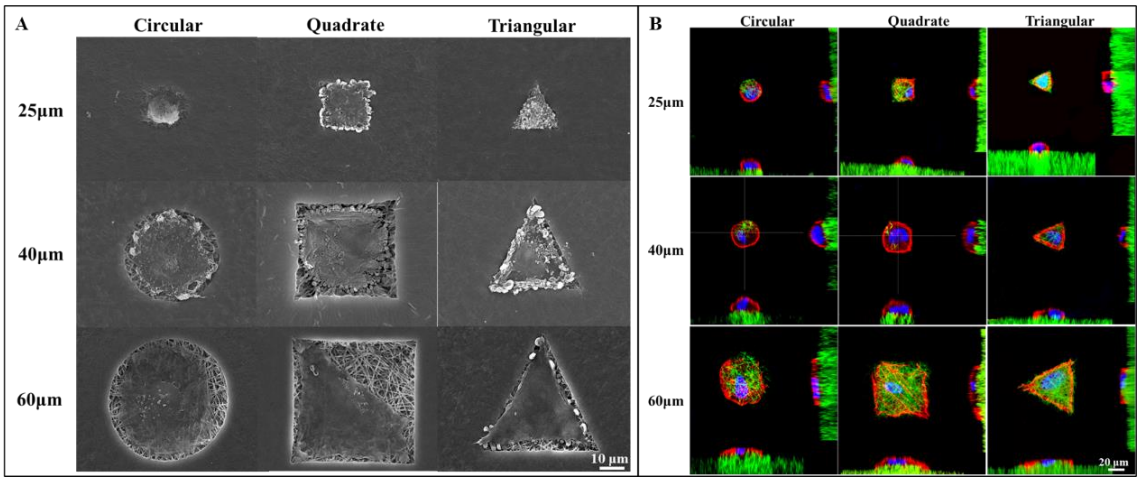

Figure 13. Single cell morphology of hDPSC on NF-MP microislands with different sizes and shapes.
A. SEM images of the apical surface of single hDPSCs on each microisland shows that with the increase in micropattern diameter, the cells displayed more spreading. **B.** Confocal z-stacked images displayed in 3D show the lateral views of single hDPSCs on each microisland. It demonstrated that with increased surface area in the micropattern, the cell height decreased. Red indicates phalloidin-stained actin filaments, green indicates FITC-conjugated GelMA nanofibers and blue indicates the nuclei.

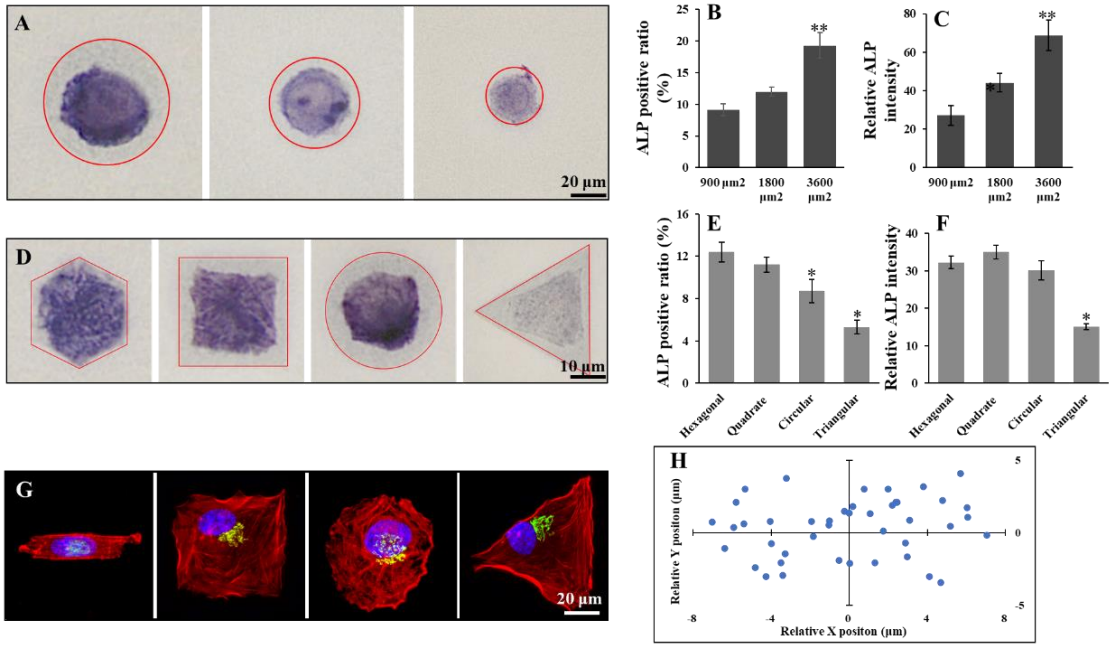

Figure 14. Differentiation and polarization behaviors of single hDPSCs on NF-MPs with various micropattern morphologies.
(**A**) shows typical ALP-positive single cells on circular NF-MP microislands with surface area of 3600, 1800 and 900 μm^2, respectively. (**B**) and (**C**) are the quantitative data of (**A**), which show the ALP-positive ratio and relative ALP intensity of single hDPSCs on NF-MPs with different surface areas, respectively. (**D**) shows typical ALP-positive single cells on 900 μm^2 NF-MP microislands with different shapes (hexagonal, quadrate, circular, and triangular). (**E**) and (**F**) are the quantitative data of (**E**), which show the ALP-positive ratio and relative ALP intensity of single hDPSCs on NF-MPs with different shapes, respectively. (**G**) shows typical Golgi apparatus-stained single cells on NF-MP microislands with different shapes (rectangular, quadrate, circular, and triangular). Red indicates phalloidin-stained actin filaments, green indicates Golgi apparatus and blue indicates the nuclei. (**H**) is the scatter plot showing the distribution pattern of Golgi apparatus within the single hDPSCs on rectangular NF-MP microislands. X axis defines the longitudinal axis of the microislands and Y axis indicates the imaginary line perpendicular to the X axis.

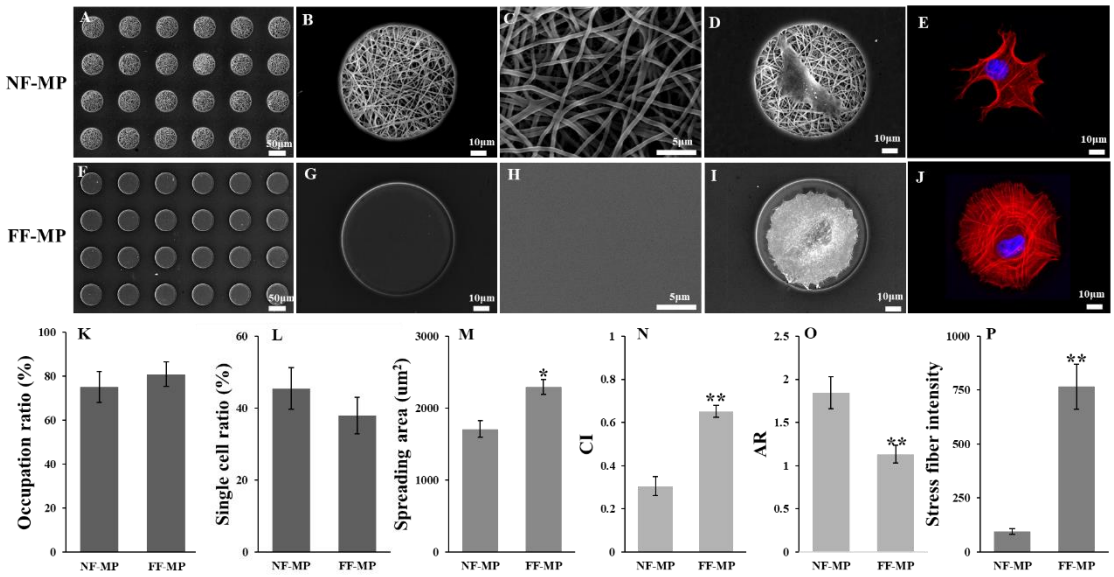

Figure 15. Morphologies and cell adhesion behaviors on the NF-MPs and FF-MPs. (**A**) and (**B**) are SEM images of the NF-MP microislands. In comparison, (**F**) and (**G**) are SEM images of the FF-MP microislands. (**C**) and (**H**) show the surface topographies of the NF-MP and FF-MP microislands, respectively. (**D**) and (**I**) are SEM images displaying typical morphologies of single hDPSCs when cultured on a NF-MP and FF-MP surface, respectively. (**E**) and (**J**) are confocal images showing the distribution of actin filaments within single hDPSCs on NF-MP and FF-MP microislands, respectively. Red indicates phalloidin-stained actin filaments and blue indicates the nuclei. (**K**) and (**I**) show the cell occupation ratio and single cell ratio of the NF-MP and FF-MP scaffolds, respectively. (**M**) shows the cell spreading area of single hDPSCs on NF-MPs and FF-MPs after 24 hours' culture. (**N**) shows the circularity index and (**O**) shows the aspect ratio, both are descriptive indexes to show the morphological features of single hDPSCs on NF-MPs and FF-MPs. (**P**) is the quantitative data of (**E**) and (**J**), showing the difference in actin distribution on the NF-MPs and FF-MPs. Modified with permission from [336].

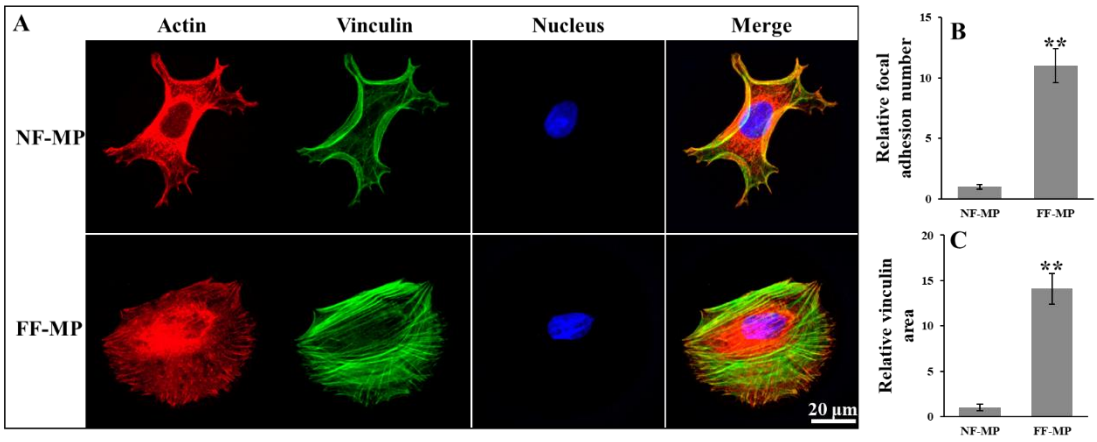

Figure 16. Formation of focal adhesions within single hDPSCs on NF-MPs and FF-MPs.

A. Typical images illustrating the formation of focal adhesion, indicated by the vinculin signals (green), are shown on NF-MPs and FF-MPs, respectively. Red indicates phalloidin-stained actin filaments, green indicates vinculin and blue indicates the nuclei. (**B**) and **C**) are semi-quantitative data of (**A**). (**B**) shows the relative focal adhesion number and (**C**) shows the relative focal adhesion area of a single hDPSC on NF-MPs and FF-MPs, respectively. The number and area of focal adhesion on NF-MPs were calibrated as 1, respectively. Modified with permission from [336].

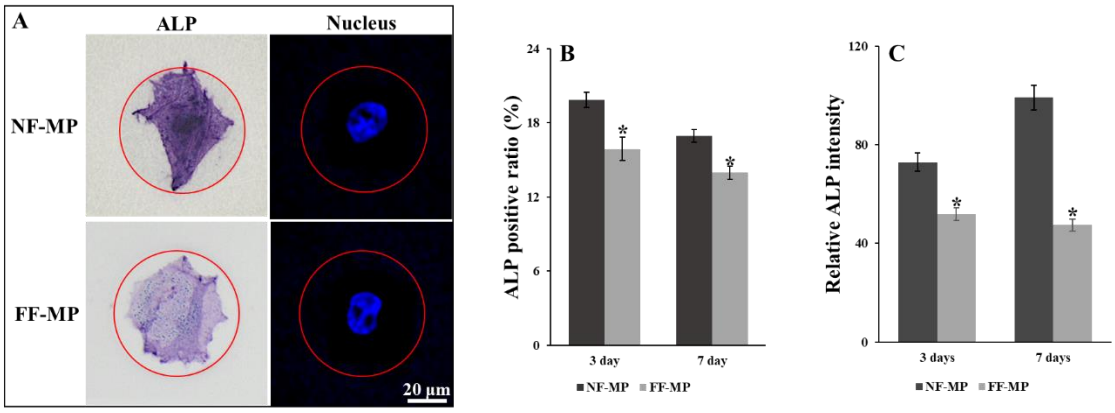

Figure 17. Differentiation of single hDPSCs on NF-MPs and FF-MPs.
(**A**) Typical images of ALP-positive single hDPSCs cultured on NF-MPs and FF-MPs, respectively. (**B**) shows the ALP-positive ratios of single hDPSCs on NF-MPs and FF-MPs at 3 days and 7 days after cell seeding. (**C**) shows the relative ALP activity of single hDPSCs on NF-MPs and FF-MPs at 3 days and 7 days after cell seeding. Modified with permission from [336].

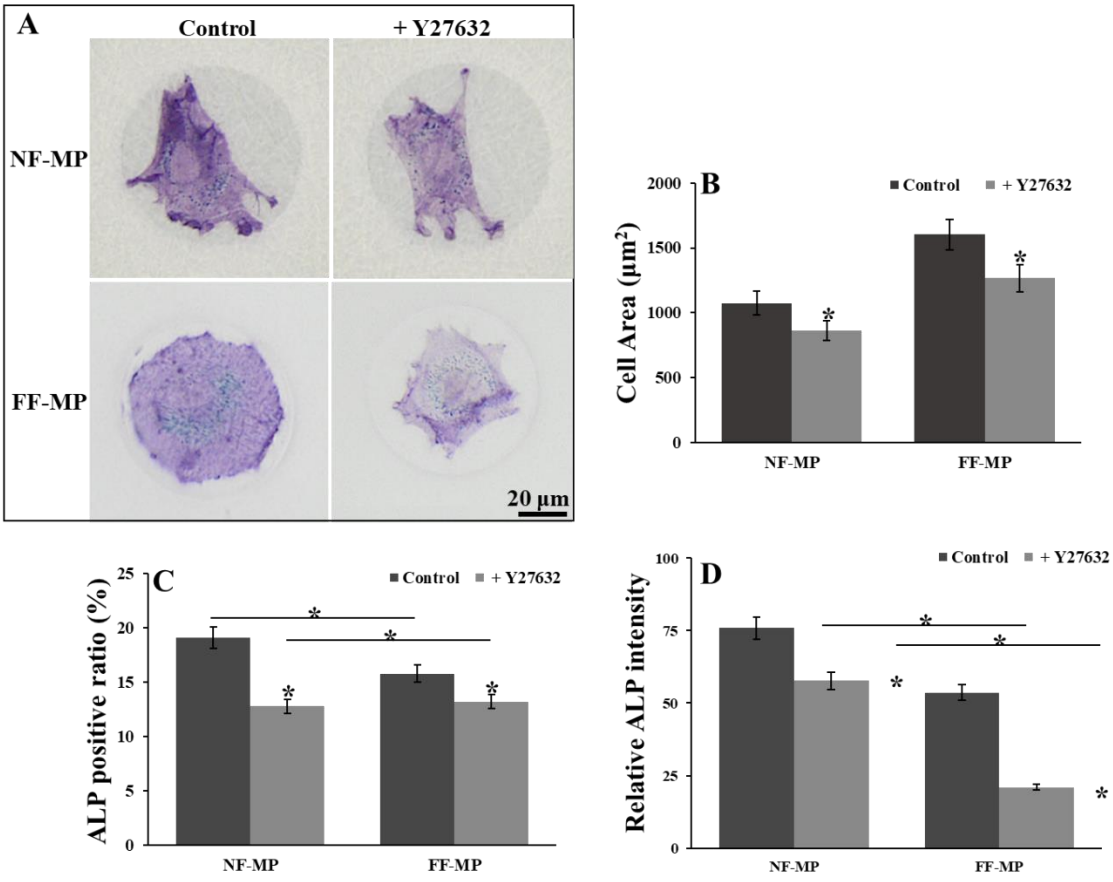

Figure 18. Morphology and differentiation changes of single hDPSCs on NF-MPs and FF-MPs with the inhibition of RhoA/ROCK pathway.
(**A**) shows typical ALP staining images of single hDPSCs with the addition of ROCK inhibitor Y-27632 on NF-MPs and FF-MPs. **B**. Quantitative data of the single cell spreading area with the addition of Y-27632 on NF-MPs and FF-MPs. (**C**) and (**D**) show the changes in ALP positive ratio and relative ALP activity of single hDPSCs on NF-MPs and FF-MPs with the addition of Y-27632, respectively. Modified with permission from [336].

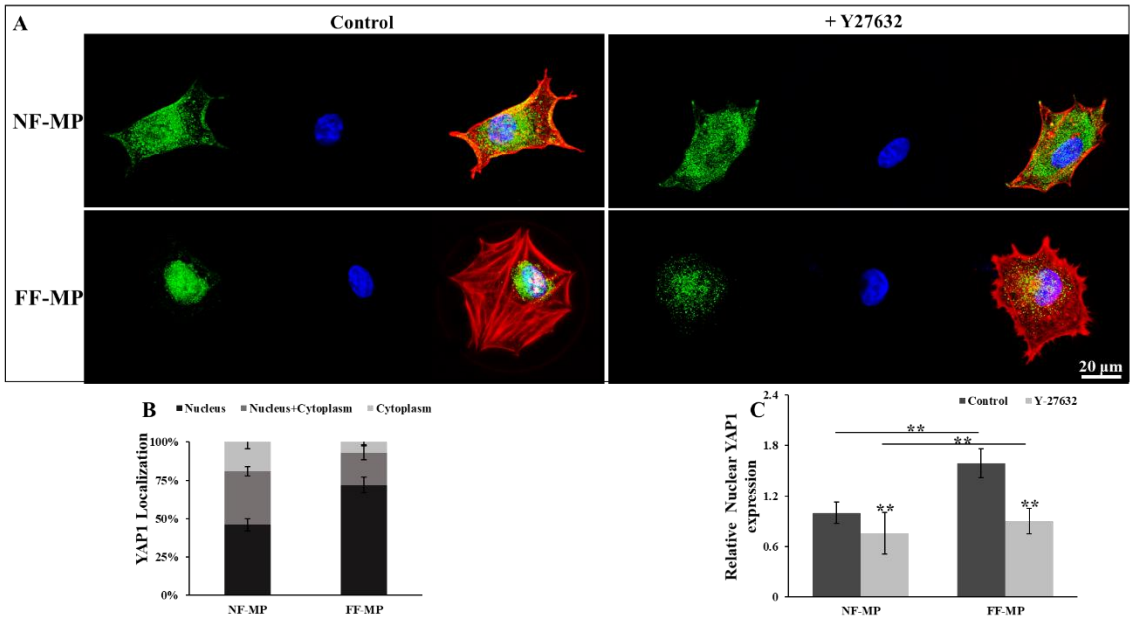

Figure 19. Distribution pattern of YAP1 within single hDPSCs on NF-MPs and FF-MPs with/without the addition of Y-26732.

A. The immunofluorescence staining of YAP1 of single hDPSC on a NF-MP and FF-MP microisland with the addition of Y-27632, respectively. Red indicates phalloidin-stained actin filaments, green indicates YAP1 proteins and blue indicates the nuclei. **B.** The cytoplasmic distribution of YAP1 proteins within a single hDPSC on NF-MPs and FF-MPs. **C**. The influence of Y-27632 on the expression of nuclear YAP1 on NF-MP and FF-MP microislands. Modified with permission from [336].

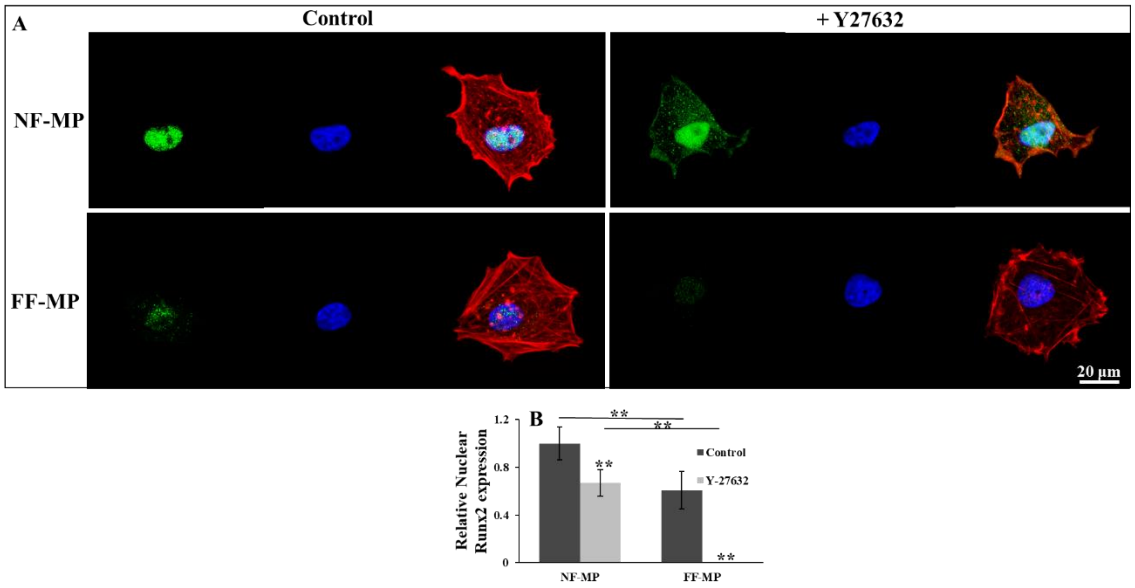

Figure 20. Expression of Runx2 within single hDPSCs on NF-MPs and FF-MPs with/without the addition of Y-26732.

(**A**) shows typical images of Runx2 distribution within single hDPSCs on NF-MPs and FF-MPs with/without the addition of Y-26732. Red indicates phalloidin-stained actin filaments, green indicates Runx2 proteins and blue indicates the nuclei. (**B**) shows the relative expression level of Runx2 within the nucleus of single hDPSCs on NF-MPs and FF-MPs with/without the addition of Y-26732. Modified with permission from [336].

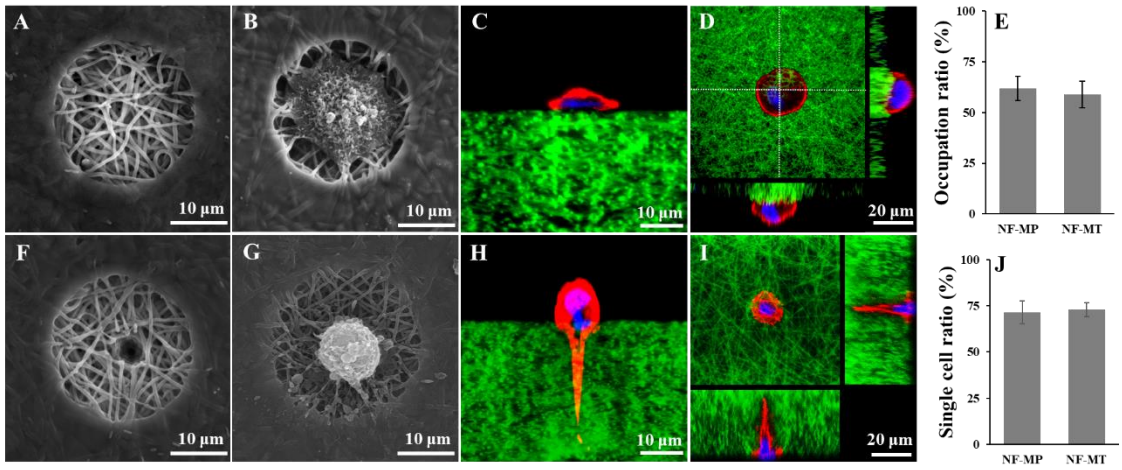

Figure 21. Morphological change of single hDPSCs on the tubular NF-MP microislands.

A. SEM image shows the morphology of a NF-MP microisland without the tubular structure. (**B**) SEM of the apical cell surface of a single hDPSC cultured on a NF-MP microisland. (**C**) and (**D**) confocal images of the lateral and 3D views of a single hDPSC on a NF-MP via sectioning (C) and confocal z-stack 3D projection scan (D), respectively. (**F**) shows the morphology of a NF-MP microisland with the tubular structure (NF-MT). (**G**) SEM of the apical cell surface of a single hDPSC on a NF-MT with drilled hole. (**H**) and (**I**) confocal images of the lateral views of a single hDPSC on a NF-MT via sectioning (H) and confocal z-stack 3D projection scan (I), (**E**) and (**J**) illustrate the cell occupation ratios and single cell ratios on the NF-MPs and NF-MTs, respectively. In (**C**), (**D**), (**H**) and (**J**), red indicates phalloidin-stained actin filaments, green indicates FITC-conjugated GelMA nanofibers and blue indicates the nuclei.

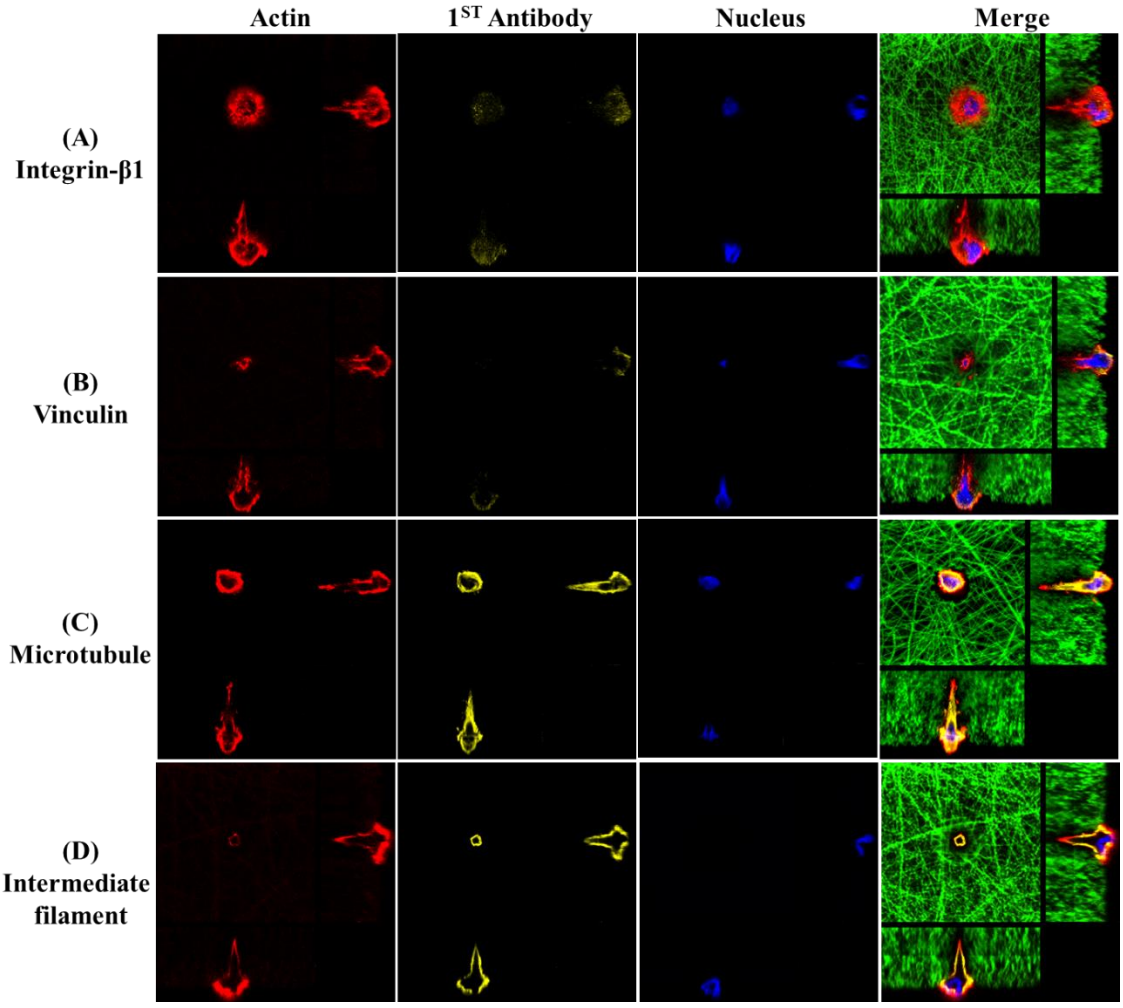

Figure 22. Characterization of the hDPSC cellular process on NF-MT microislands
Red indicates phalloidin-stained actin filaments, green indicates FITC-conjugated GelMA nanofibers, blue indicates the nuclei and yellow indicates integrin-β1 in (**A**), vinculin in (**B**), tubulin (microtubules) in (**C**) and intermediate filament in (**D**).

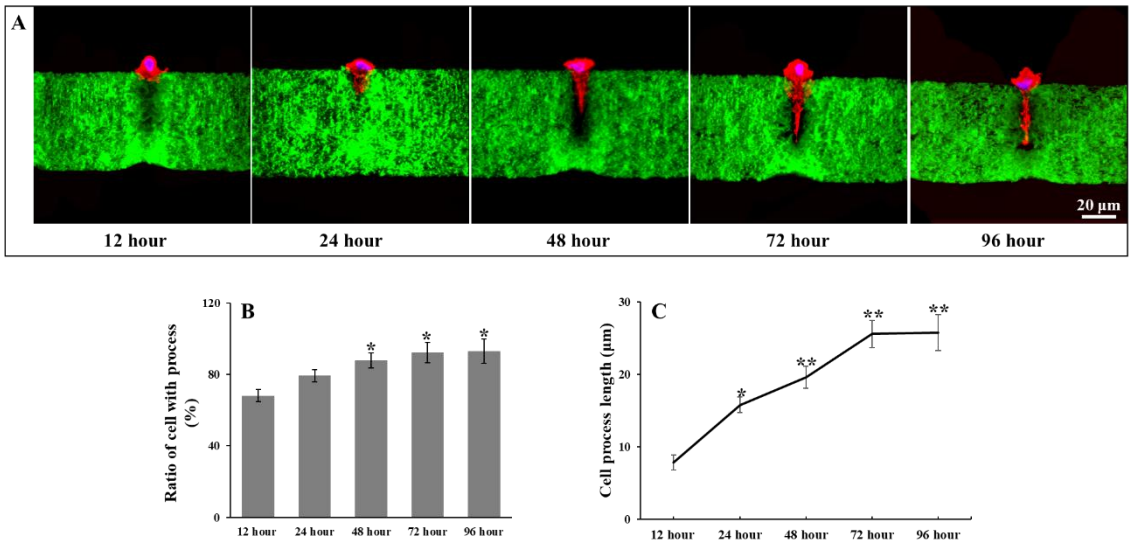

Figure 23. Tracing of the cellular process formation within single hDPSCs on the NF-MTs.

(**A**) shows typical lateral view images of hDPSC processes on the NF-MTs at 12, 24, 48, 72 and 96 hours after cell seeding. Red indicates phalloidin-stained actin filaments, green indicates FITC-conjugated GelMA nanofibers, and blue indicates the nuclei. (**B**) shows the change in the ratio of cell with process with time. (**C**) is the quantitative analysis of (**A**).

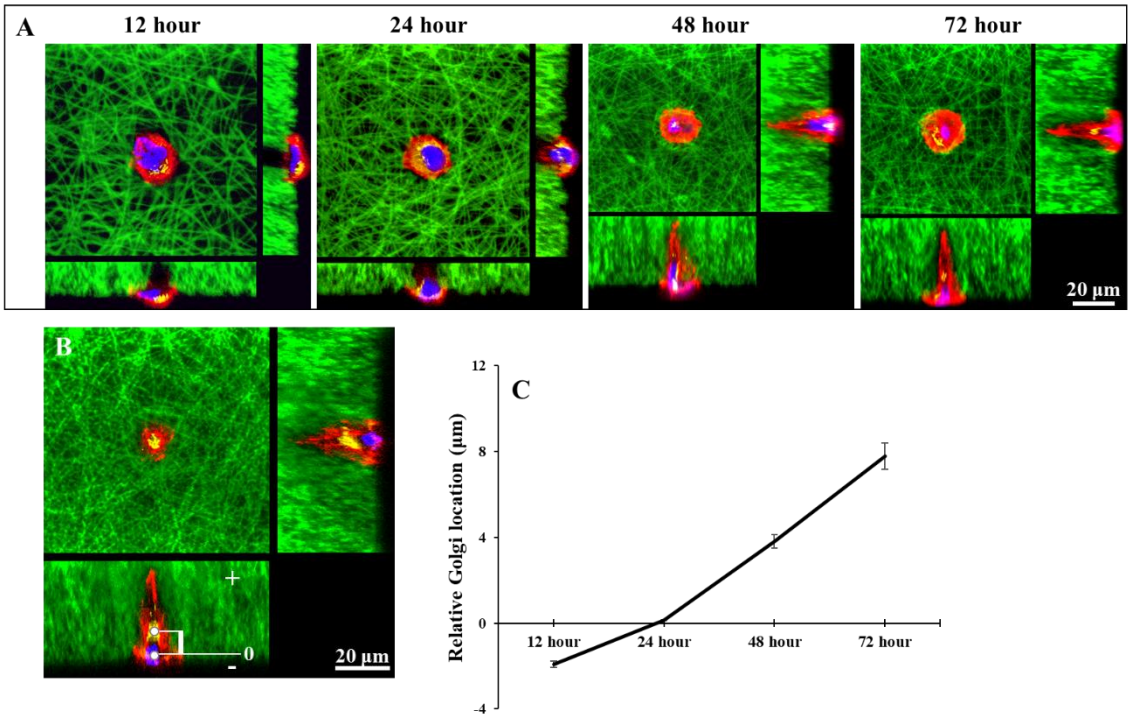

Figure 24. Tracing of the Golgi apparatus movement within single hDPSCs on the NF-MTs.

(**A**) shows typical Golgi apparatus locations within single hDPSCs on the NF-MTs at 12, 24, 48 and 72 hours after cell seeding using confocal stacking scan. Red indicates phalloidin-stained actin filaments, green indicates FITC-conjugated GelMA nanofibers, blue indicates the nuclei and yellow indicates the Golgi apparatus. (**B**) illustrates the construction of a coordinate system to locate Golgi apparatus and measure its distance to the nucleus. (**C**) is the quantitative data of (**A**).

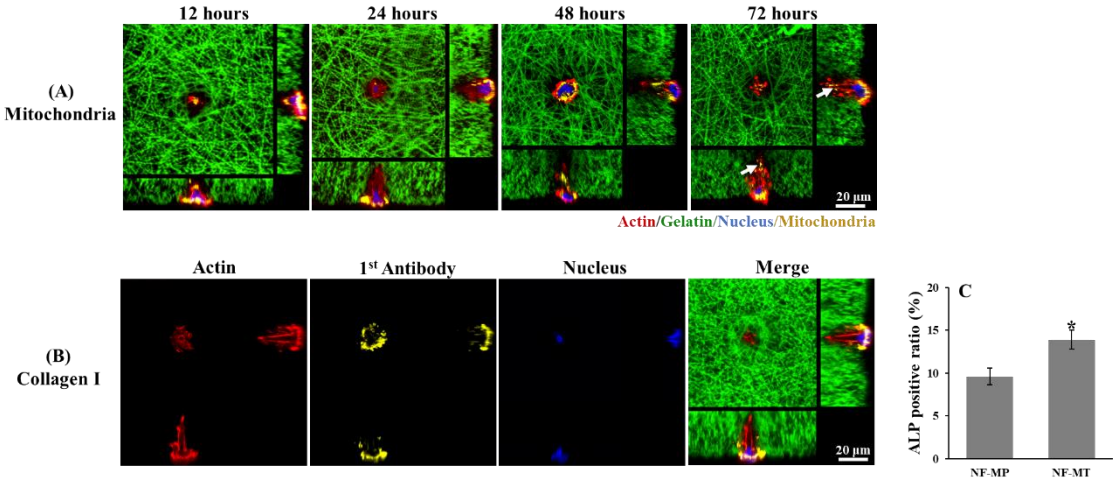

Figure 25. Physiological function of the polarized hDPSCs on NF-MTs.
(**A**) shows the distribution of mitochondria within a hDPSC at 12, 24, 48 and 72 hours after cell seeding using confocal stacking scan. White arrow indicates mitochondria at the cell process tip. (**B**) shows the expression of Collagen I within a polarized hDPSC. (**C**) shows the ALP-positive ratios of single hDPSCs on a NF-MP and NF-MT scaffold, respectively. In (**A**) and (**B**), red indicates phalloidin-stained actin filaments, green indicates FITC-conjugated GelMA nanofibers and blue indicates the nuclei. Yellow indicates mitochondria in (**A**), and Collagen I in (**B**).

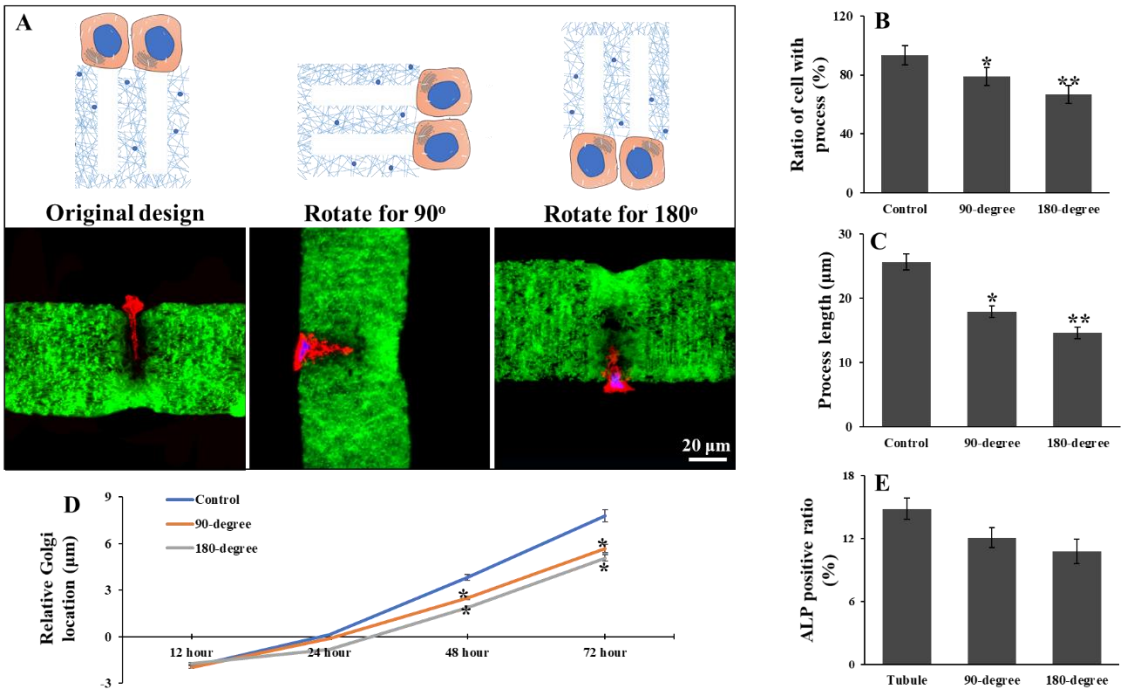

Figure 26. The influence of gravity on hDPSC polarization and differentiation. (**A**) illustrates how the 3 microenvironments were designed to explore the role of gravity on hDPSC behaviors. Three groups are included, the control group, the 90-degree rotation group and the 180-degree rotation group. Red indicates phalloidin-stained actin filaments, green indicates FITC-conjugated GelMA nanofibers and blue indicates the nuclei. (**B**) and (**C**) show the changes in ratio of cell with processes and average process length of the 3 groups, respectively. (**D**) shows the changes in Golgi apparatus locations with time of the 3 groups. (**E**) shows the changes in ALP positive ratio of single hDPSCs of the 3 groups.

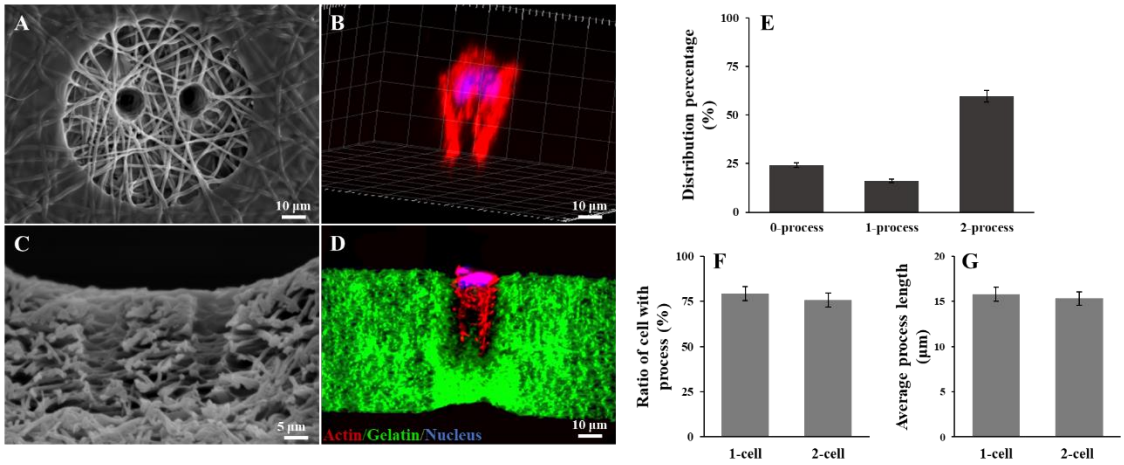

Figure 27. Polarization behaviors of hDPSCs on the 2-cell NF-M2T microislands. (**A**) and (**C**) are SEM images showing the top view and lateral view of a NF-M2T microisland, respectively. (**B**) is a 3D reconstructed image of 2 cells that accommodate within a NF-M2T microisland and there are 2 cellular processes formed on the microisland. This image was achieved by reconstructing a confocal stack series. (**D**) also displays the lateral views of a 2-cell NF-M2T, which was achieved by cryosectioning. (**E**) illustrates the distribution pattern of cellular process formation among all 2-cell NF-M2T microislands. (**F**) and (**G**) show the ratio of NF-M2T with processes and average process length on the NF-M2T microislands, respectively. In (**B**) and (**D**), red indicates phalloidin-stained actin filaments, green indicates FITC-conjugated GelMA nanofibers and blue indicates the nuclei.

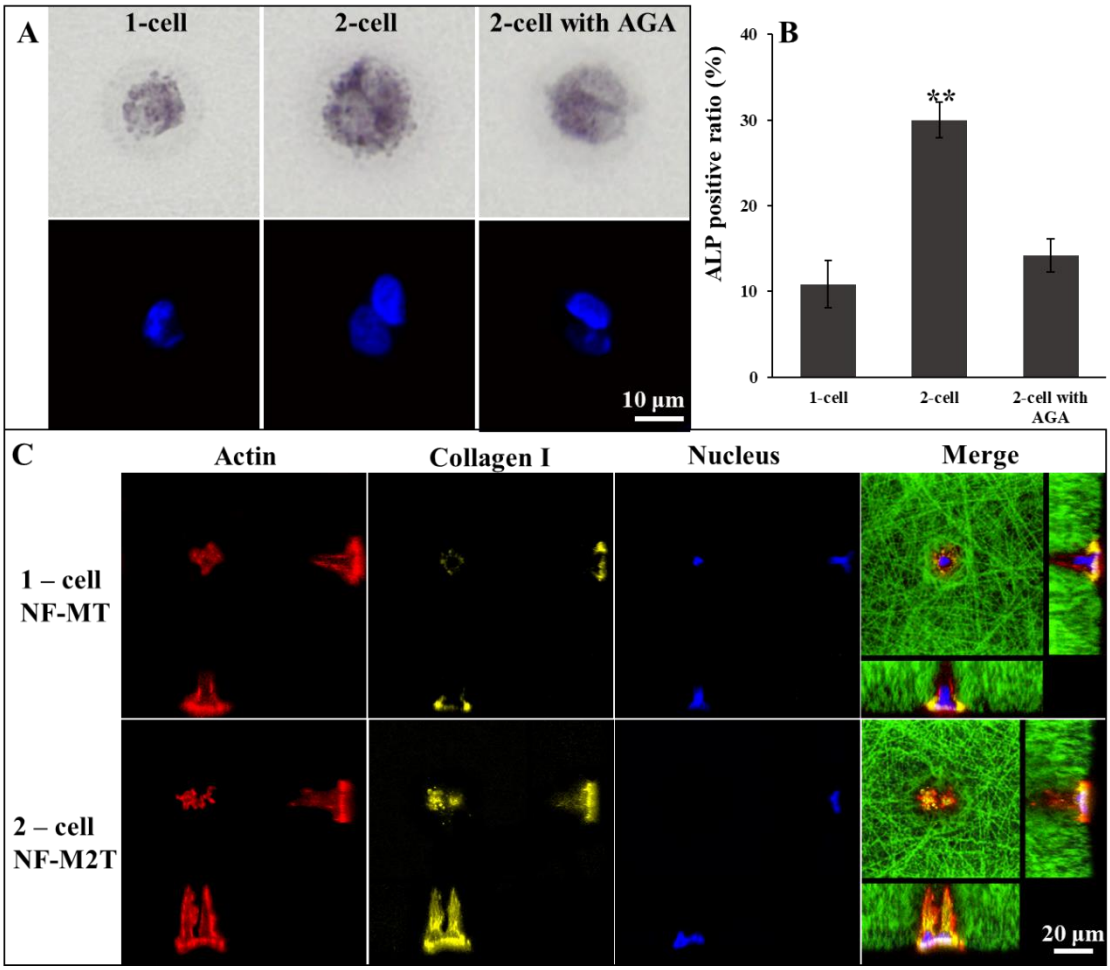

Figure 28. The differentiation of hDPSCs on the 2-cell NF-M2T microislands. (**A**) illustrates typical images of ALP-positive 1-cell NF-MT microislands, ALP-positive 2-cell NF-M2T microislands, and ALP-positive 2-cell NF-M2T microislands with the addition of gap junction inhibitor, AGA, respectively. (**B**) is the quantitative analysis of ALP positive ratios of the 3 groups illustrated in (**A**). (**C**) shows the comparison in collagen content between the 1-cell NF-MT microislands and 2-cell NF-M2T microislands. Red indicates phalloidin-stained actin filaments, green indicates FITC-conjugated GelMA nanofibers, blue indicates the nuclei and yellow indicates Collagen I.

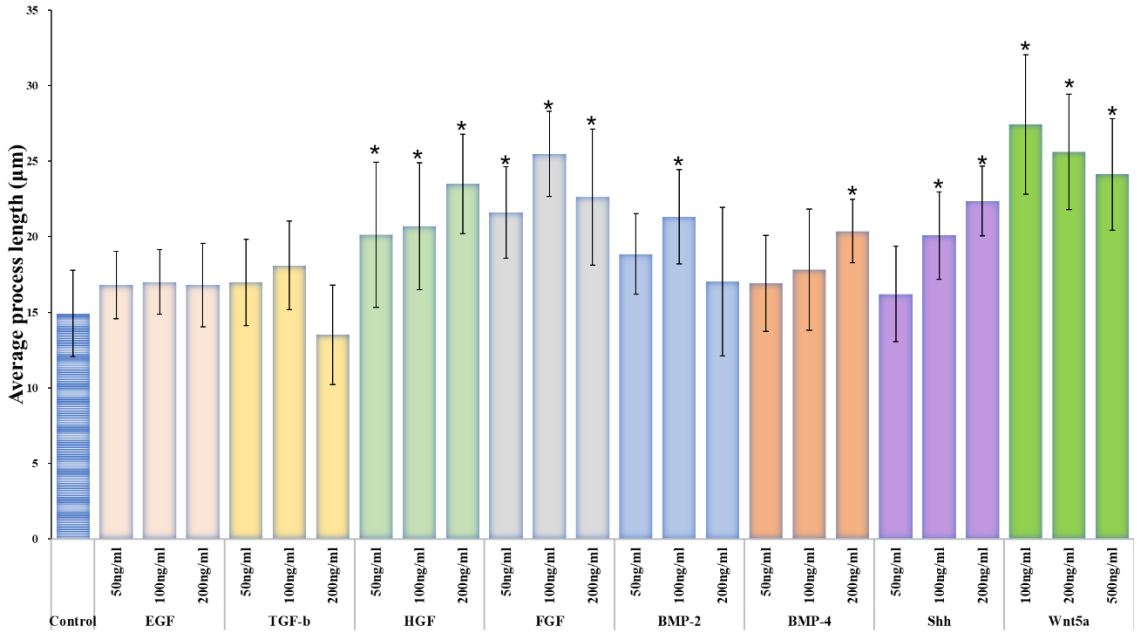

Figure 29. Effects of various growth factors on the process lengths of single hDPSCs on the NF-MT microislands.
Eight types of growth factors are shown, including EGF, TGF-β1, HGF, FGF, BMP-2, BMP-4, Shh and Wnt 5a and three concentrations for each growth factor are shown.

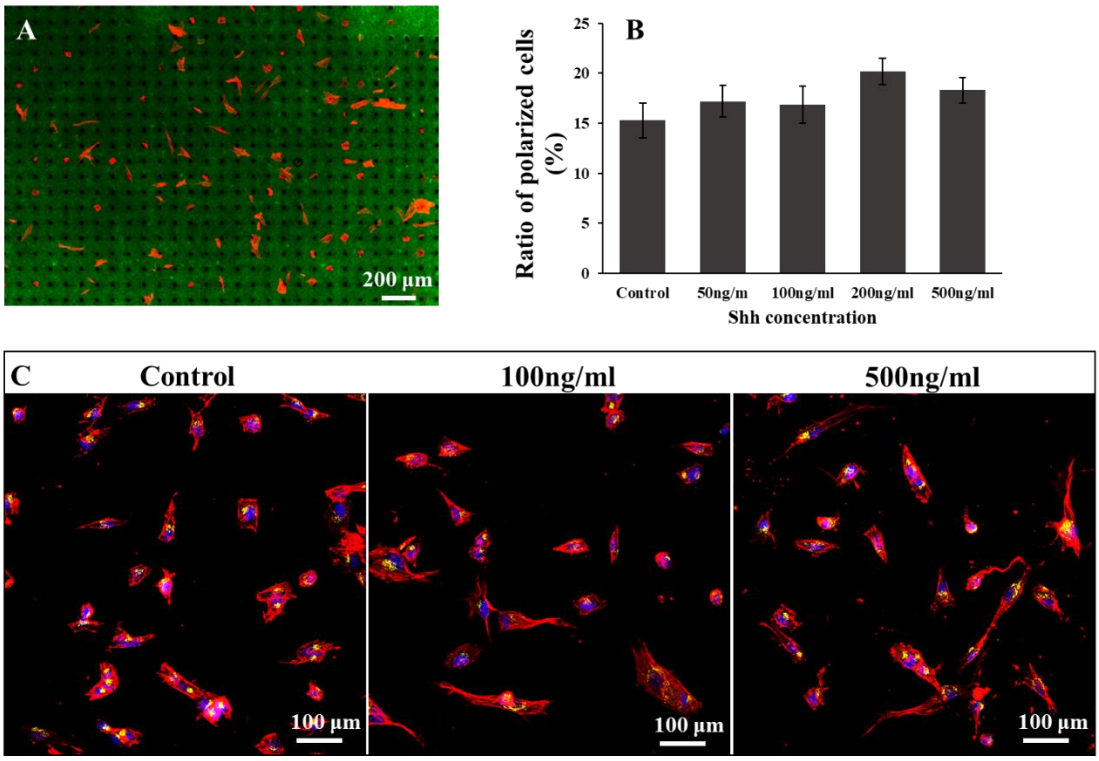

Figure 30. Effects of Shh of various concentrations on hDPSCs cultured on the patterned and non-patterned nanofibrous matrix.

A. Shown is the cell adhesion status on circular NF-MTs with the addition of 500 ng/ml Shh. **B.** The ratio of polarized hDPSCs cultured on the nanofibrous matrix with the addition of 0, 50, 100, 200 and 500 ng/ml Shh. **C.** Shown are the typical images of hDPSCs cultured on the nanofibrous matrix with the addition of 0, 100 and 500 ng/ml Shh, respectively. Red indicates actin filaments, blue indicates nuclei and yellow indicates Golgi apparatus.

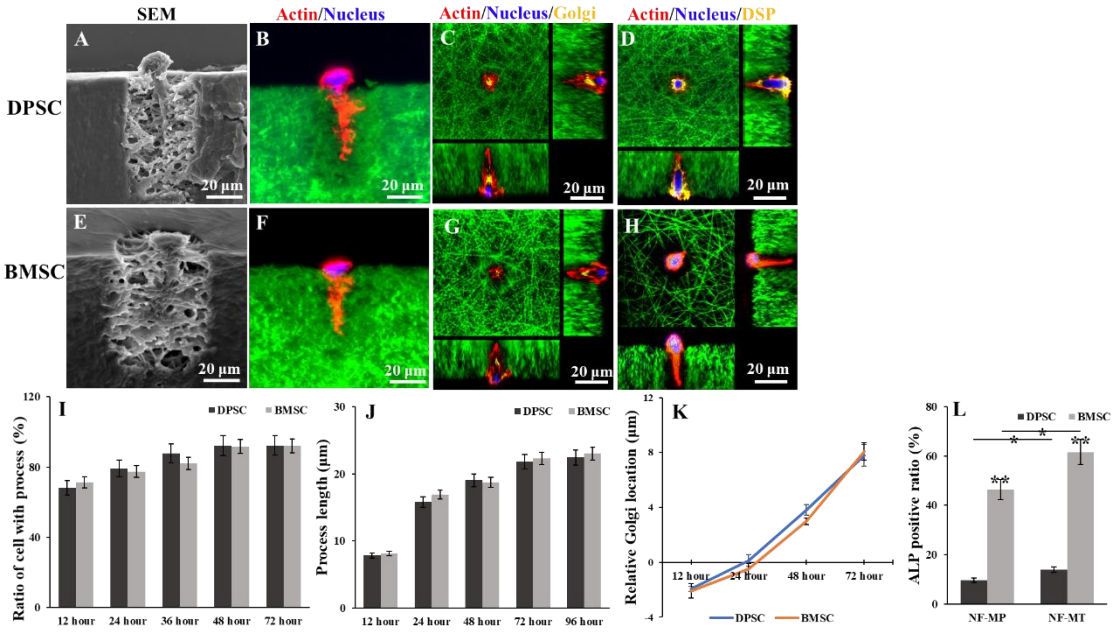

Figure 31. Polarization and differentiation behaviors of single rBMSCs on the NF-MT microislands.

(**A**) and (**E**) are SEM images illustrating the later views images of cellular process formed on NF-MT microislands of a single hDPSC and a single rBMSC, respectively. (**B**) and (**F**) are confocal images showing the same morphologies of (**A**) and (**E**), respectively. (**C**) and (**G**) display the location of Golgi apparatus within a single hDPSC and a single rBMSC on a NF-MT microisland, respectively. (**D**) and (**H**) show the anti-DSP staining of a single hDPSC and a single rBMSC on a NF-MT microisland, respectively. (**I**) and (**J**) show the ratio of cell with process and average length of the cellular process of single hDPSCs and rBMSCs, respectively. (**K**) is the quantitative analysis of Golgi apparatus movement within single hDPSCs and rBMSCs on NF-MT microislands. (**L**) shows the difference in ALP positive ratio of single hDPSCs and rBMSCs on NF-MP and NF-MT microislands. In (**C**), (**D**), (**G**) and (**H**), red indicates phalloidin-stained actin filaments, green indicates FITC-conjugated GelMA nanofibers and blue indicates the nuclei. In (**C**) and (**G**), yellow indicates Golgi apparatus, while in (**D**) and (**H**), yellow indicates the DSP proteins.

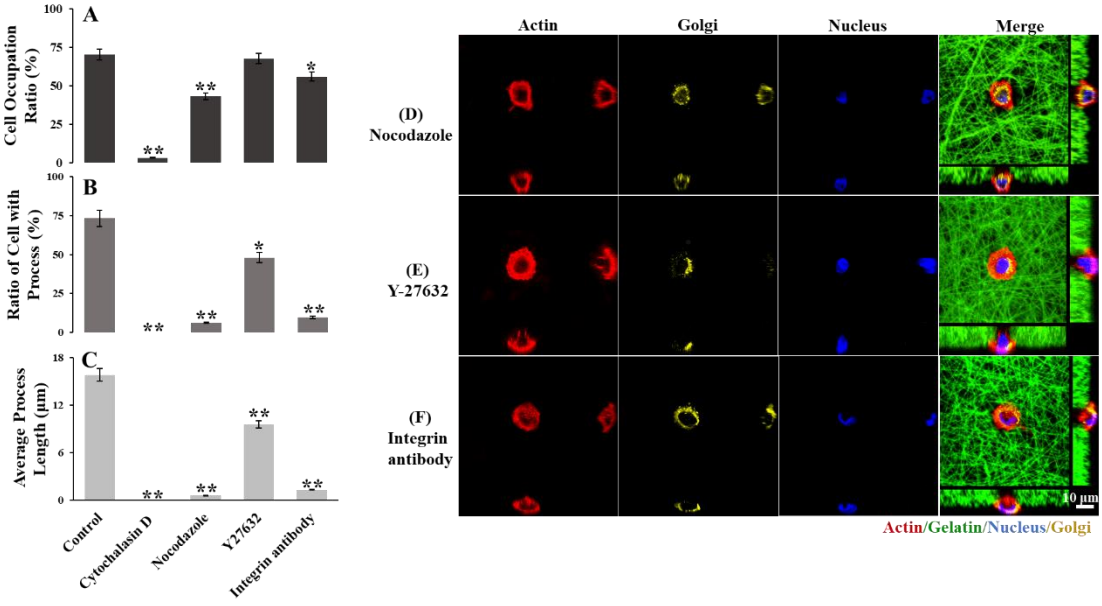

Figure 32. Influence of inhibitors on single hDPSC polarization on NF-MT microislands.

The cellular inhibitors include microfilament assembly inhibitor cytochalasin D, microtubule assembly inhibitor nocodazole, ROCK pathway inhibitor Y-27632 and the antibody against β1 integrins. (**A**) shows the changes in cell occupation ratio on a NF-MT scaffold with the addition of various inhibitors. (**B**) and (**C**) show the changes in the ratio of cell with process and average process length of single hDPSCs on NF-MT microislands with the addition of various inhibitors, respectively. (**D**), (**E**) and (**F**) show the morphology of single hDPSCs and the location of Golgi apparatus with the addition of nocodazole, Y-27632 and integrin antibody, respectively. Red indicates phalloidin-stained actin filaments, green indicates FITC-conjugated GelMA nanofibers, yellow indicates Golgi apparatus and blue indicates the nuclei.